PAUL SCHERRER INSTITUT

PSI

Annual Report 2021

Laboratory of Radiochemistry

Cover

Is the half-life of silicon-32 correct? Researchers from the group “Isotope and Target Chemistry” investigate this question together with other partners in the frame of the SNF-funded project “SINCHRON”.

PAUL SCHERRER INSTITUT

Annual Report 2021

Laboratory of Radiochemistry

Editors
R. Eichler, A. Blattmann

Paul Scherrer Institut
Laboratory of Radiochemistry
5232 Villigen PSI
Switzerland
Secretariat +41 56 310 24 01
Fax +41 56 310 44 35

Reports are available from
Angela Blattmann
angela.blattmann@psi.ch
Paul Scherrer Institut
5232 Villigen PSI
Switzerland

See also our web-page
https://www.psi.ch/lrc/

TABLE OF CONTENTS

EDITORIAL

Dear reader,

Sad news reached us by the end of this year. Hans Rudolf von Gunten, one of the founders of the Swiss Radiochemistry died at age 93 in Nussbaumen. The calm and thoughtful and always friendly "Hansruedi" will stay in the hearts of those who had the privilege and pleasure to meet him or even to collaborate with him. Thank you Hansruedi for your all-time great support of Radiochemistry!

My sincere thanks go to all my colleagues from our laboratory, department and institute for their patience and their professional attitude in these difficult times of pandemic. These were the pillars of our scientific success also this year that we intend to present here in this traditional form of the Annual report of LRC for the year 2021. We all have the privilege to live in very interesting and exciting times, where great solutions must be found to fundamental things in people's daily lives, such as energy, food, health, climate, and sustainability. Our research work is part of this, if not directly then indirectly, through education and gain of fundamental knowledge.

Despite the increasing number of cancelled conferences our research work was very well presented at several occasions over remote channels or rarely also in person. I would like to thank all contributors for representing our laboratory and our research so well.

My special congratulations go to Cristina Müller and Nick van der Meulen for the "Triumph of Terbium" awarded with the EJNMMI Best Paper 2020 and to Nick van der Meulen's joint success with the colleagues in Bern (S. Braccini et al.) on ^{44}Sc yielding the IBA Best Paper Award 2020.

The public outreach is of increasing importance in science. Our laboratory was able to present topics of Swiss radiochemistry at the SCIENTIFICA 2021 organized by ETH Zurich. Please accept my big applause to all presenters and particularly to Patrick Steinegger and Dominik Herrmann for the excellent preparation of the radiochemistry booth and materials. I think it was great to observe the stunned glances of people from all generations observing radioactivity from a different point of view, but scary. Well done! The 3Sat Nano TV show reporting on our success in applying BluAct Technologies' milk-protein based filter material for radioactive waste concentration was well received and we got very positive responses for presenting "radiochemistry at work".

Luckily, during a short relief from COVID restrictions, we were able to have a joint social activity that, as I feel, gave everybody a great motivation boost. Based on an initiative of Patrick Steinegger we were able to visit the Institute of Forensic Medicine where Michael Thali and Dominic Gascho gave us a great deep inside into their forensics work and introduced to us the modern possibilities. After this great experience we were able to do a short hike from Adliswil, Felsenegg to Uetliberg Kulm in perfect weather conditions. At the restaurant of Hotel UTO KULM we had a very nice reception celebrating Alexander Vögele's 50th birthday (Thank you Alex!), followed by a nice dinner. Let me share a photo here, expressing our will to overcome the situation to go back to a normal life:

Last but not least, let me express my wish and hope for a further civilized handling of the pandemic situation, where societal and personal aspects of the problems and their solutions are reasonably balanced. Yes, we can influence this in a way with patience, successful work and by trying to be educated references.

Have a good year 2022 and enjoy reading,

OBITUARY

Hans Rudolf (Hansruedi) von Gunten (12.12.1928 – 7.12.2021)

Foto: Willy Brüchle, 20.4.2018 (Mainz Univ.)

Hansruedi von Gunten was the first full professor for Radiochemistry in Switzerland (University of Bern, 1971 – 1993). He studied chemistry at the University of Bern and finished his studies with a licence, including an experimental study on complex iron compounds in 1954, followed by a doctoral thesis under Profs. W. Buser and F. Houtermanns, which he finished 1956 - just before his successful ascent of Mt. Everest on May 24, 1956. The topic of his thesis was the application of ^{210}Pb to study geochemical processes in volcanology.

He then started his scientific career in 1957 at the former EIR (Eidg. Institut für Reaktorforschung in Würenlingen) and negotiated a one-year stay at the Argonne National Laboratory. He topped up his salary with small honorariums for talks on the Everest expedition, and he came to a certain fame in the community. This was quite uncomfortable for him as he felt like an "exhibition piece". He returned to Argonne National Laboratory in 1965/66, and he described this sabbatical as particularly educational, building the base for part of his later research. EIR was renamed in 1988 to Paul Scherrer Institut, and Hansruedi worked first as group leader in the *Abteilung Chemie*, later on renamed laboratory for radiochemistry and environmental chemistry. He stayed at this institute until his retirement in fall 1993. With his employment at EIR, a nuclear research and technology-oriented institute, his scientific focus broadened and now also included nuclear fission studies using chemical techniques (nuclear chemistry).

He started his academic career at the University of Bern in 1967 as a lecturer, and in 1969, he submitted a habilitation in which he discussed the double-humped mass distribution in nuclear fission at low energy. In 1970, he became an associate and, in 1971, a full professor for Radiochemistry at this university. His employment as a full professor at the University of Bern was partly triggered by a very attractive offer at the Institute of Nuclear Chemistry at the University of Mainz, which he turned down partly on compassionate grounds.

His research interest was remarkably broad. It included nuclear fission studies using novel techniques such as the spinner (developed by B. Hahn for experiments at CERN) to measure half-lives of spontaneously fissioning nuclides or search for long-lived superheavy elements in nature. Another focus was the determination of nuclear charge distributions in thermal neutron-induced fission of several nuclides such as ^{235}U, ^{233}U, ^{239}Pu and ^{249}Cf, respectively. During a sabbatical leave to LBNL Berkeley in 1980/81, where he worked with the Nobel laureate Glenn T. Seaborg, he became involved in studies of nucleon transfer reactions in heavy-ion-induced reactions. Besides his scientific engagement in nuclear physics oriented research, he applied his knowledge to environmental sciences. There, his primary focus was the investigation of sorption processes of radionuclides on different minerals to contribute to the research activities at EIR/PSI in nuclear waste oriented topics. He also stayed interested in applications of ^{210}Pb, e.g., using this natural radionuclide to determine accumulation rates of lake sediments or to determine the ages of glacier ice cores. Worth mentioning is his brilliant idea to use ^{222}Rn to determine the water inflow from the river Glatt into the nearby groundwater aquifer. This method is still used to measure the water exchange rates between rivers and adjacent aquifers.

Mainly at University of Bern, because of the engagement of its physics department in lunar missions, he participated in chemical studies of lunar samples, also to investigate evaporation/adsorption processes under atmospheric conditions of the moon.

Besides his truly widespread scientific activities it is of utmost importance to mention his very kind and emphatic personality and his modesty. Generations of students in the field of radiochemistry and nuclear chemistry were impressed by his competence and guidance in all facets of professional problems. Moreover, he was always also interested in the private and personal situation of his students.

H.W. Gäggeler, U. von Gunten

Wide bandgap semiconductors for α-spectroscopy beyond 200°C

G. Tiebel (ETHZ/PSI), M. Carulla Areste (PSI/PSD), M. Camarda (SenSiC), R. Dressler (PSI), E. Griesmayer (CIVIDEC/TU Wien), D. Herrmann (PSI), P. Steinegger (ETHZ/PSI), C. Weiss (CIVIDEC/TU Wien), J. Wilson (ETHZ/PSI)

Introduction

The determination of chemical properties of transactinide elements (Z ≥ 104) is carried out at the so-called one-atom-at-a-time level. Their scarce availability requires an efficient and fast identification using highly reliable, time-resolved α- and fission-fragment-spectroscopy. The need for higher stationary surface temperatures in chromatographic investigations of so far uncharacterized transactinide elements demands for dedicated detector developments suitable for high-temperature environments. Currently used Si-based semiconductor solid state detectors (band gap of 1.11 eV [1]) are only operable up to ≈50°C. Single crystal, chemical vapor deposition (scCVD) diamond (band gap of 5.5 eV [2]), as a wide bandgap semiconductor, offers promising prospects in this regard. The material's suitability for temperatures of up to 200°C was shown [3]. 4H-SiC (band gap 3.27 eV [4]) represents another promising, less cost-intensive candidate for high temperature α-spectroscopy. Here, we present the current status of measurements performed with a 140-µm-thin scCVD diamond-based detector and a 4H-SiC-based detector.

Experimental

The heating setup and the source-to-detector configuration corresponded to the one used in [3]. However, the bias voltage was applied to the front electrode, while the signal was extracted from the rear side. Two sensors with outer dimension of 4.5 x 4.5 x 0.1 mm^3 (diamond) and 5 x 5 mm^2 (4H-SiC) were used. The scCVD diamond sensor was set up in a parallel plate geometry with electrode dimensions of 4 x 4 mm^2. Meanwhile the 4H-SiC sensor was fabricated as shown in [5]. A negative bias voltage of -150 V was applied in both cases. The temperature was increased continuously from ≈20°C to about 500°C with a rate of ≈6°C min^{-1}. The signal readout was established via a CIVIDEC C2 broadband amplifier in conjunction with a LeCroy Waverunner oscilloscope. A minimum of 10000 signals were stored and analyzed with respect to their full widths at half maximum (FWHM) as well as their peak areas. Whereas, dark current measurements were conducted for the scCVD diamond-based sensor, comparable measurements for the 4H-SiC-based detector are currently in progress.

scCVD diamond-based detector

The FWHM of the analog signal, as a measure for the drift time of electrons, was evaluated and plotted as a function of the sensor temperature (Fig. 1). The drift time gradually increases up to 150°C. Between 150°C and 200°C a peak is visible. Above this temperature threshold the drift time rapidly decreases up to 250°C before increasing again.

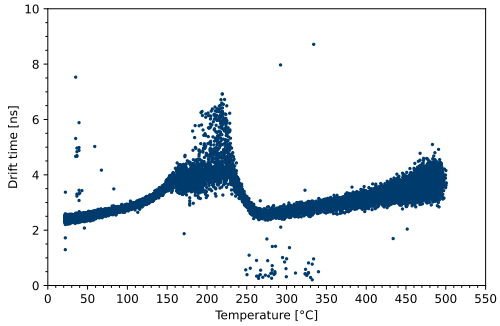

Figure 1: FWHM of the analog signals as a function of the sensor temperature (sweeping heating mode; bias voltage: -150 V); errors are too small to be shown.

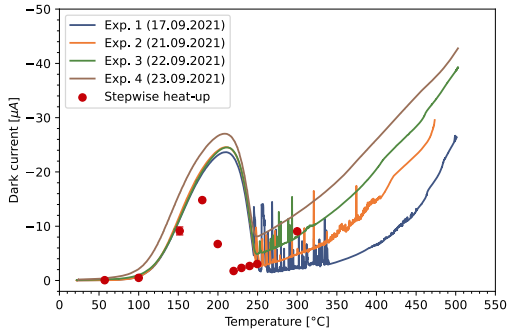

Figure 2: Dark current measurements of multiple experiments as a function of temperature (lines: sweeping heating mode; dots: stepwise heating mode).

The dark current shows comparable trends as the above-shown drift times in the investigated temperature range (see Fig. 2). Between 100°C and 250°C, a clear and reproducible maximum of the dark current is observed. With a stepwise heating (as opposed to the generally applied sweeping temperature mode), a maximum was reached at a somewhat lower temperature and amplitude. Thus, the effect causing an increase in dark current appears to be a time-delayed process, which seems distorted due to a comparably fast heating rate. In general, the effect(s) affecting the drift times and the dark current

behavior is/are attributed to solid-state physical phenomena in the bulk of the sensor, which remain to be explained in the future.

The peak area of the current signal, as a measure of the charge carrier collection efficiency, shows a rather stable behavior up to 240°C (see Fig. 3). At this temperature, an instantaneous decrease of the peak area to a continued stable behavior could be observed up to 400°C (see added regression lines in the respective regions in Fig. 3). The lower but stable values at higher temperatures indicates an unperturbed operation of the sensor at a somewhat lower charge carrier collection.

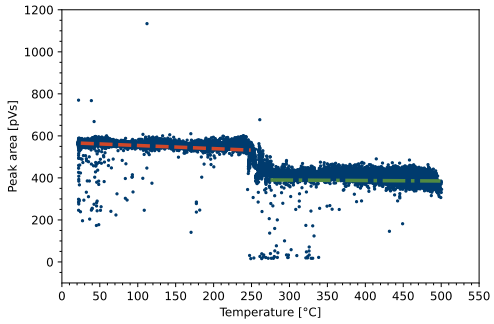

Figure 3: Peak areas of the analog signals as a function of the sensor temperature (sweeping heating mode; bias voltage: -150 V, electron drift mode); errors are too small to be seen. The dashed lines represent individually fitted linear regressions of the data of the two plateaus.

4H-SiC-based detector

The first high-temperature experiments with 4H-SiC-based detectors were performed in an analogous manner as in case of the scCVD diamond sensor.

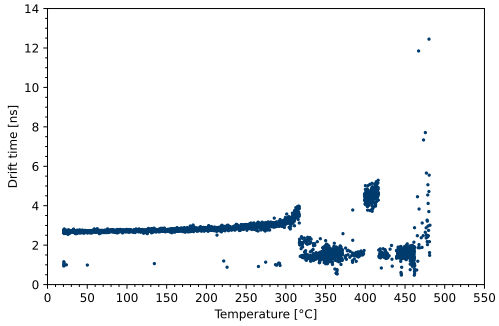

Figure 4: FWHM of the analog signals as a function of the sensor temperature (sweeping heating mode, bias voltage: -150 V); errors are too small to be shown.

As seen from the drift time behavior up to 300°C, stable detector operation was observed (see Fig. 4). By exceeding this threshold, the sensor becomes unstable, before recovering for a short period at roughly 400°C. In contrast to the scCVD diamond-based detector, the drift time for this material decreases abruptly with increasing temperature, only to increase again briefly at 400°C. The peak area is similarly stable and nearly constant up to 300°C (see Fig. 5). Above this temperature, a decrease of the peak area is observed, which briefly recovers around 400°C (as it is the case for the electron drift times).

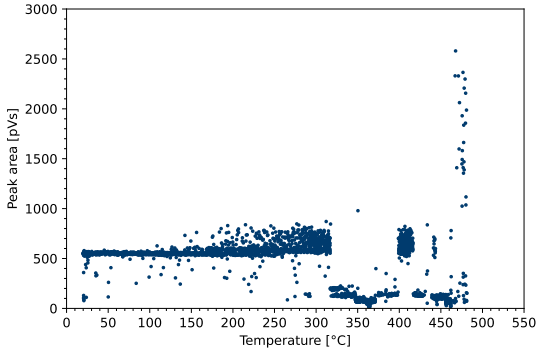

Figure 5: Peak areas of the analog signals, as a function of the sensor temperature (bias voltage: -150 V); errors are too small to be shown.

Conclusion and outlook

Previous experiments with scCVD diamond sensors encountered an upper temperature threshold for a stable detector operation at around 200°C. This limitation has been surpassed with the herein presented experiments. In summary, current-sensitive measurements of α-particles-induced charge carriers could be carried out with both sensor materials up to 500°C. Thus, both, the scCVD diamond-based and the 4H-SiC sensor provide stable operation beyond 200°C. The presented results are preliminary and further investigations are needed with both sensor materials, in order to show the reproducibility. In the future, besides characterizing further and already available 4H-SiC-based detectors (in particular larger sensor areas), the level of understanding regarding the solid state effects at elevated temperatures shall be improved. Furthermore, reliable and stable high-temperature contacting remains a priority to ensure the continuous, months-long operation of such wide band gap detector materials at elevated temperatures in the framework of gas-adsorption chromatography experiments with transactinide elements.

References

[1] B. Streetman et al., *Solid State Electronic Devices*, 5th ed., Prentice-Hall, 2000

[2] C. Kittel, Introduction to Solid State Physics, 9th ed., Wiley, 2018

[3] B. Kraus et al., *Nucl. Instrum. Methods Phys. Res., Sect. A.*, **989** (2021), pp. 164947

[4] T. Kinoshita et al., *Mater. Sci. Forum*, **264-268** (1998), pp. 295-298

[5] M. Jotterand et al., *LRC Annual Report 2020* (2021), pp. 9-10

Comparison of two setups for a next-generation vacuum adsorption chromatography experiment using MONTE CARLO simulations

G. Tiebel (ETHZ/PSI), R. Dressler, R. Eichler (PSI), P. Steinegger (ETHZ/PSI)

Introduction

MONTE CARLO simulation-based (MCS) approaches are routinely used during analysis of gas-phase adsorption chromatography experiments of superheavy elements (SHEs) [1]. The fundamental idea is to apply a microscopic-kinetic description of adsorption and desorption processes on an atomic scale [2]. This model can be used to describe both thermo- and isothermal chromatography experiments at ambient pressure as well as in vacuum. The half-lives of the investigated radioisotopes but especially the adsorption enthalpies of the corresponding element have a decisive influence on the outcome of such experiments. Aside of approaches employing gas-catchers [3], vacuum chromatography experiments may allow for the characterization of SHEs with very short-lived radioisotopes in the millisecond regime (for more details see [4]). However, the stopping of nuclear reaction products in an evacuated environment remains a major challenge. On the one hand, produced radioisotopes of SHEs can be directly implanted in a so-called hot catcher following physical pre-separation. This approach requires a fast thermal release of deeply implanted nuclear reaction products, while rising questions regarding long-term operation (>24 h). On the other hand, nuclear reaction products may be thermalized and extracted as a low-energy ion beam using a gas-catcher. Such ions with translational energies in the keV-regime lead to a sub-surface implantation and thus to a presumed faster release [5]. The downside is a loss in efficiency due to the interposed gas-catcher with extraction efficiencies <30%.

Here, we present the results of a MCS-based approach targeting two versions of a vacuum chromatography setup employing a low-energy product ion beam (sub-surface implantation). These will help to decide on the more favorable version of the two setups for a next-generation isothermal vacuum adsorption chromatography experiment. Stated goal is the verification of velocity of transported species in a vacuum chromatography experiment.

The MCS algorithm

The above-mentioned algorithm developed by I. Zvára and B. Eichler [1] was parallelized using Python to improve the calculation time. The much-improved MCS code allows for continuous tracing of Cartesian coordinates of simulated particles in the three-dimensional space. With this approach, a description of axially asymmetric columns is feasible (e.g., a hole in the outer wall of a column).

Two conceivable versions of an experimental setup have been considered in the herein discussed simulations:

A. A one-side open column with a detector facing the far end; a central hole in the detector serves as particle inlet (see Fig. 1, top).

B. A two-side open column with a detector at either side; a hole in the center of the column serves as particle inlet (see Fig. 1, bottom).

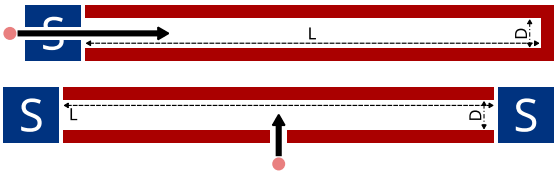

Figure 1: Schematic sketch of the two setups with **S** indicating the detector position, **L** the column length and **D** diameter of the column (top: setup **A**, bottom: setup **B**; see

The dimensions of the above-presented settings were optimized with respect to the column length and the diameter (the diameter of the inlet hole remains the same throughout all simulations). Since the distance between the inlet hole and the detector surface is decisive, the column length for setup B was doubled, thus allowing for a direct comparison between the two setups. The starting points of all particles were set as uniformly distributed coordinates on the opposite side of the inlet hole (area dimension: projection of inlet hole). For each L/D-combination for setups A and B, 10'000 atoms were simulated using the radioisotope ^{284}Nh (nihonium, Z=113) with a half-life of 0.97 s [6], an adsorption enthalpy of -58 kJ mol^{-1} [7] and an isothermal temperature of 1000°C (negligible retention loss).

Results

The relationship between the yield and the number of adsorptions is apparent: more adsorptions lead to a longer retention time and thus, to an increased probability of decay inside the column (i.e., lower yields). At the same time, a certain number of adsorptions is instrumental in order to reliably probe the adsorption energy of the investigated SHE. Hence, a balance needs to be established between a

sufficient yield (>90%) and a minimum number of surface interactions. A further constraint was established by the largest high-temperature alpha-detectors currently available in our laboratory. As of now, these can only cover the exit of a column with a diameter of 20 mm. The simulated yields for both setups A and B behave similarly, showing an expected decrease with increasing column length at constant diameter (see Fig. 2 and 3). This is a direct consequence of increasing retention times and the limited lifetime of the simulated particles. Thus, more particles decay in the column and are therefore not detected at the outlet(s). Meanwhile, and likewise expected, the number of adsorption interactions increases with increasing column length at constant diameter. The opposite case of an increasing column diameter at a constant column length leads to a higher yield, but less wall interactions. The parameters of a chromatography column for setups A and B in consideration of the above outlined constraints (>90% yield and 20 mm diameter) is indicated accordingly (Figs. 2 and 3).

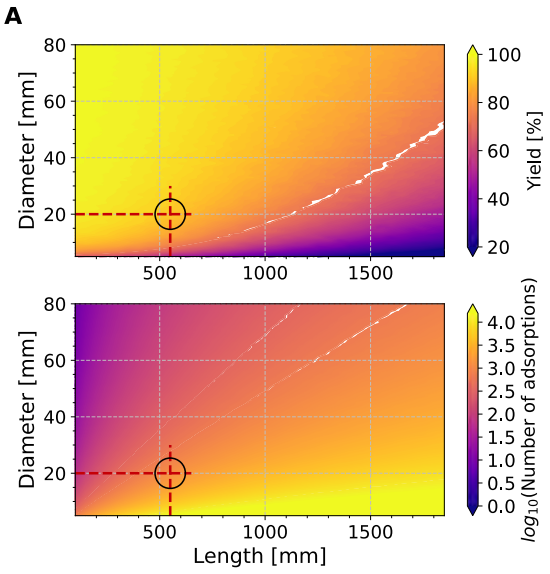

Figure 2: Results of the simulations of setup **A** (axial injection) with respect to the collected yield at the outlet (top) and the number of surface interactions (bottom) as functions of the column diameter and length; mind the log(Number of adsorptions) in case of the lower graph.

Exiting particles through the inlet hole is of particular importance in case of setup B, as seen by comparing the simulated yields for both settings at low diameters. In the case of setup B, a high number of wall interactions near the inlet leads to an increased probability for an escape through the very same inlet hole (comparably large inlet hole diameter to column diameter ratio).

Conclusion and outlook

In conclusion, setup A (axial insertion) shows a higher number of interactions (≈1000 for setup A and about 100 for setup B) under the considered constraints, thus favoring this setup. Moreover, setup A may be advantageous in terms of its seemingly less complicated technical realization (e.g., only one isothermal zone and one detector).

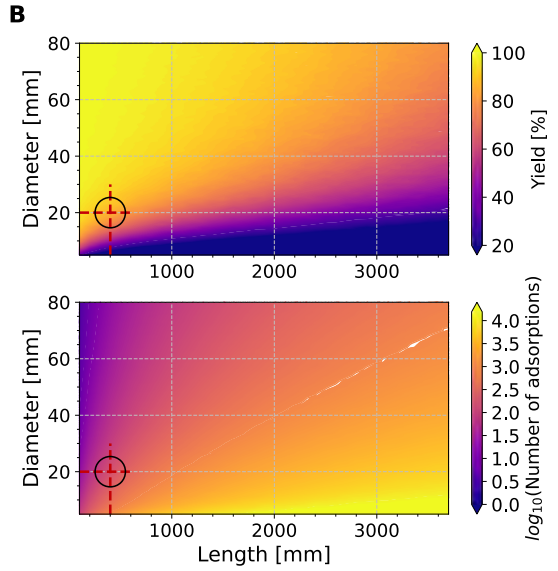

Figure 3: Results of the simulations of setup **B** (axial injection) with respect to the collected yield at the outlet (top) and the number of surface interactions (bottom) as functions of the column diameter and length; mind the log(Number of adsorptions) in case of the lower graph.

The gained knowledge will be used to for the optimization and realization of a next-generation vacuum adsorption chromatography experiment. For doing so we are currently planning a first experiment following a design approach according to setup A. First test experiment will be focusing on demonstrating the applicability of vacuum chromatography to radionuclides with half-lives in the millisecond regime.

References

[1] I. Zvára, *The Inorganic Radiochemistry of Heavy Elements: Methods for Studying Gaseous Compounds,* Springer-Verlag, Berlin, 2008

[2] R. Eichler, B. Eichler, 'Thermochemical Data from Gas-Phase Adsorption and Methods of their Estimation' in: M. Schädel, D. Shaughnessy (eds.), *The Chemistry of Superheavy Elements*, 2nd ed., Springer-Verlag, Berlin Heidelberg, 2014

[3] V. Varentsov, A. Yakushev, *Nucl. Instrum. Methods Phys. Res. Sect. A*, **940** (2019), pp. 206-214.

[4] P. Steinegger et al., *J. Phys. Chem. C*, **120** (2016), pp. 7122-7132

[5] P. Steinegger et al., *LRC Annual Report 2015* (2016), p. 5

[6] Z. Sóti et al., *EPJ Nuclear Sci. Technol.*, **5**(6) (2019), pp. 1-11

[7] V. Pershina, *J. Phys. Chem. C*, **120** (2016), pp. 20232-20238

Removal of ^{235}U fission products from contaminated water using a whey-protein-based activated charcoal hybrid filter material

G. Tiebel (ETHZ/PSI), S. Bolisetty (BluAct Technologies GmbH/ETHZ), R. Eichler (PSI), L. Melnik (JINR/FLNR), R. Mezzenga (ETHZ), P. Steinegger (ETHZ/PSI)

Introduction

Radioactively contaminated wastewater is an important issue in the fields of, e.g., radiochemistry, nuclear medicine and nuclear energy. Therefore, techniques for the removal of radioactive contaminants are of great interest. In that regard, a relatively new approach is the application of a novel filtration material consisting of whey-protein-based amyloid-fibrils mixed with activated carbon [1]. The applicability of this filter material for the removal of radionuclides from aqueous solutions has been successfully demonstrated [2,3].

Whereas first experiments focused on filtering off individual radioisotopes of elements Tc and Cs, we show here the applicability of the above-mentioned filter material to a broad mixture of different radioisotopes from a variety of chemical elements. For this purpose, the recently recommissioned PSI SINQ gas-jet facility was used [4], which allows for the continuous provision of fission products of ^{235}U from the irradiation position to a radiochemical laboratory.

Experimental

A KCl-aerosol-loaded carrier gas (N_2 at 0.9 L min^{-1}, 1.44 bar in the fission chamber) was used for the transport of the fission products. The neutron beam shutter was fully open throughout all experiments. While radioisotopes of volatile elements were transported directly, radioisotopes of non-volatile elements adsorb onto the aerosol particles. These aerosols were collected on a glass fiber filter for 30 minutes (volatile radioisotopes are mostly not retained). The collected salt aerosols were washed off the glass filter with 10 ml distilled water. After the recording of a γ-spectrum of the obtained solution, it was filtered through the hybrid filter material. The filtrate was then examined again by γ-spectroscopy.

Results

A variety of fission fragments could be identified in the originally prepared radioactive solution (Fig. 1, blue spectrum). Besides radioisotopes of non-volatile elements, such as Mo, Ce or Sb, more volatile species were likewise identified (e.g., Kr or I). The solution can be classified as weakly to moderately radioactive (≈1 mSv/h in close proximity). Thus, the diverse inventory may serve as a model for most radioactive wastewaters, as encountered at, e.g., hospitals, low-activity laboratories as well as in case of voluminous liquid waste from nuclear power plants.

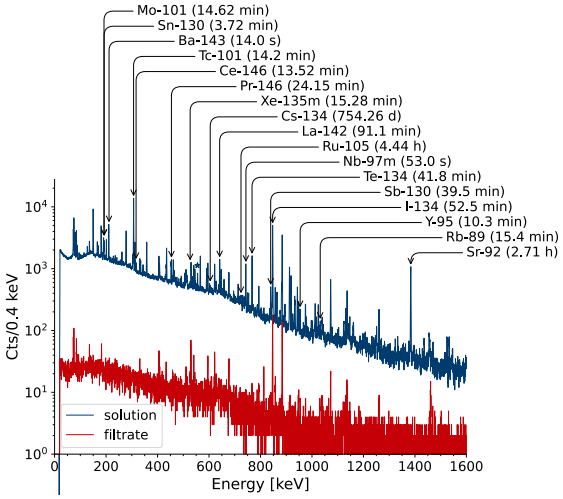

Figure 1: γ-spectrum (t_{live}=30 min) of the radioactive solution before (blue) and after (red) filtration; for reasons of clarity only one radioisotope per element is labelled. Radionuclides in the filtrate (red spectrum) are ^{133}I (529.9 keV), ^{130}Sb (793.5 keV), ^{129}Sb (812.8 keV) and ^{134}I (847.0 keV).

After a single filtration step, the filtrate contained significantly less radionuclides, thus indicating an efficient filtration (Fig. 1, red spectrum) with a reduction of the activity by a factor of ≈50. Only isotopes of iodine and antimony managed to pass through the hybrid filter.

Conclusion and outlook

It has been shown that the whey-protein-based amyloid-fibrils activated carbon filters are well applicable even to a broad mixture of radionuclides. With the removal of almost all chemical elements, these results indicate a low elemental selectivity, thus rendering the filter material suitable for the use with low-activity wastewater.

Future studies will investigate the filtration capacity, the long-term stability (e.g., radiation damage) as well as the extraction mechanism. The last point is of particular importance to understand the selectivity of the filter.

References

[1] S. Bolisetty, R. Mezzenga, *Nature Nanotechnology*, **11** (2016), pp. 365-371
[2] S. Bolisetty et al., *Environ. Sci.: Water Res. Technol.*, **6** (2020), pp. 3249-3254
[3] N. M. Chiera et al., *RSC Adv.*, **11** (2021), 32454-32458
[4] A. Vögele et al., *LRC Annual Report 2019* (2020), pp. 17-18

Online Gas Chromatography with Tl/TlOH in Preparation for Nh/NhOH

J. Wilson (ETHZ/PSI), N. V. Aksenov, Yu. V. Albin (FLNR/JINR), Z. Asfari (UDS), A. Y. Bodrov , G. A. Bozhikov, V. I. Chepigin, I. Chuprakov, S. N. Dmitriev (FLNR/JINR), R. Eichler (PSI), B. Gall (UDS), N. S. Gustova (FLNR/JINR), D. Herrmann (PSI), A. V. Isaev, A. Sh. Madumarov, O. N. Malyshev (FLNR/JINR), E. Pishchalnikova (FLNR/JINR, MSU), Y. A. Popov, A. V. Sabelnikov (FLNR/JINR), P. Steinegger (ETHZ/PSI), A. I. Svirikhin, M. G. Voronyuk (FLNR/JINR), V. Zobnin (MSU)

Introduction

Chemistry experiments with superheavy elements (SHEs) present multiple challenges ranging from low production rates to ambiguous chemical results. Although results are still debated for flerovium (Z=114) [1], elemental copernicium (Z=112) has been chemically characterized successfully [2]. Currently, no conclusive chemical results have been obtained for nihonium (Nh, Z=113) [3,4]. With the help of the lighter homologs, chemistry experiments at the one-atom-at-a-time level are carefully prepared before addressing the corresponding SHE. Here, we present the current state of preparation for a next nihonium experiment using its lighter homolog thallium in an isothermal gas adsorption chromatography study.

Thallium has been the subject to multiple predictions and experiments varying in agreement. In online vacuum chromatography experiments, the authors determined an adsorption enthalpy of elemental thallium on quartz of $-\Delta H_{ads}^{SiO_2}(\mathrm{Tl}) = 158\ \mathrm{kJ/mol}$ [5]. This is in good agreement with theoretical predictions of $-\Delta H_{ads}^{SiO_2} = 150.2\ \mathrm{kJ/mol}$ using ADF BAND calculations on fused silica [6]. Offline chromatographic studies in the laminar flow regime found $-\Delta H_{ads}^{SiO_2}(\mathrm{TlOH}) = 134\ \mathrm{kJ/mol}$ on likewise fused silica [7]. At this time no theoretical enthalpies have been published for TlOH on quartz. Unfortunately, the offline and online results for TlOH did not readily agree [7,8]. It was theorized that an interfering Tl(III) species forms during online experiments. In fact, Tereshatov et al. showed the possibility of a predominant production of Tl(III) readily obtained at a cyclotron, i.e., a production pathway similar to the one discussed here [9]. Thus, to diminish the higher oxidation state, a hot tantalum getter was placed at the exit of the recoil transfer chamber to reduce all thallium before entering the subsequent chromatographic section. Based on previous experiments, TlOH is expected to form in combination with a fused silica surface (even in reducing atmospheres) [7].

Experimental Setup

^{184}Tl was produced at the U400 accelerator facility of the Flerov Laboratory of Nuclear Reactions (FLNR) in Dubna, Russian Federation. Further details regarding the production and physical pre-separation (SHELS), as well as the direct catch measurements, can be found in [8]. Direct catch measurements were carried out at three different ion beam intensities, i.e., 1.2 µA, 1.9 µA, and 3.1 µA. This resulted in ^{184}Tl production rates of 25 s^{-1}, 38 s^{-1}, and 67 s^{-1} respectively.

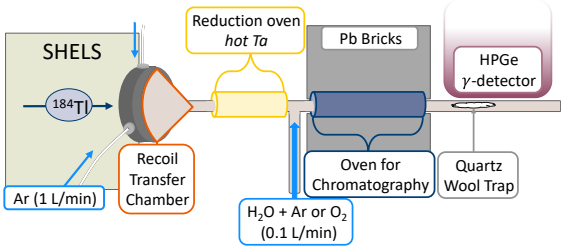

Figure 6. Schematic of the chemistry setup shown with the T-shaped column; the reduction oven and the lateral dosing of reactive gases represent the main changes in comparison with [8].

The above-mentioned major modification in comparison to earlier experiments concerned the inclusion of a Ta getter. Thereto, a second heated section was included between the recoil transfer chamber (RTC) and the chromatography section (see Fig. 1). In order to dose O_2 and H_2O, T-shaped fused silica columns were employed. This allowed for careful addition of reactive species without consuming the Ta getter itself. Due to the generally too short chromatography section (construction limitation), the temperature profiles were far from uniform (see Fig. 2), thus complicating data analysis. However, using the measured temperature profiles in conducted Monte Carlo simulations (MCS) allows for the extraction of meaningful thermodynamic data.

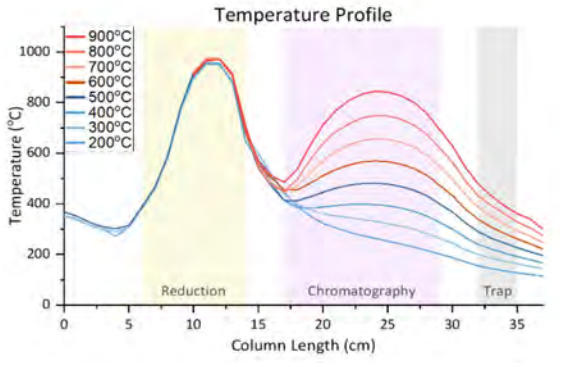

Figure 2. Actual "isothermal" temperature profiles measured in steps of 100°C starting at the exit of the recoil transfer chamber; 'Reduction' refers to the Ta getter oven, 'Chromatography' to the oven for chromatography, and 'Trap' is the quartz wool plug for catching escaping radionuclides in front of the HPGe-γ detector.

Simulations, following the approach outlined in [10], were used to reproduce the measured external chromatograms under full consideration of all experimental parameters (e.g., gas flow and the temperature profiles).

Results and Discussion

Shown here are two external chromatograms as obtained with one chromatography column (Fig. 3; mind experiment order). Ar (1 L/min) was flushed through the RTC (heated to 400°C), with an addition of O_2 and H_2O (0.1 L/min) through the secondary inlet. The two distinct onsets pertain to two chemical species observed, i.e., likely TlOH and elemental Tl. The unexpected preservation of the latter is attributed to the dehydroxylation of the fused silica surface around 400°C [11] with temperature and time. The reduced density of reactive surface sites seemingly helps to preserve Tl in its elemental state.

The surface hydroxyl concentration does not stay constant with increasing temperature. In fact, it starts to decrease at 200°C and stabilizes around 500°C [11]. Typical fused silica surfaces have a small film of water and many hydroxyl-groups. While the surface water is lost at ≈100°C, dehydroxylation is promoted with increasing temperature. At approximately 400°C, the number of hydroxyl surface concentration quickly decreases and the ability to rehydroxylate the surface reduces [11]. Multiple hydroxyls can bond on one silicon atom, but the final hydroxyl is the hardest to remove. Final hydroxyl removal occurs through two pathways: chain or special adjacent ring formation. Chain adjacent hydroxyls form an unstable, easily decomposing 4-member siloxane ring, but spatially adjacent hydroxyls form a more favorable multimember siloxane ring [11]. Consequentially, there are still hydroxyls on the surface even at 1000°C [11].

The levelling off, in the case of experiments 6 and 7, as well as the immediate drop with experiment 8, shows the impact of disappearing hydroxyl-groups on the surface. As experiments 6 and 7 are assumed to be heavily affected by a progressing dehydroxylation, these two points were excluded from further analysis. The diminished hydroxyl-groups seem to allow Tl to be preserved in its elemental state and pass through the column without reacting to TlOH (see green curve/points in Fig 3). However, as there are still hydroxyls on the surface, TlOH may still form, thus creating an offset seen in the second set of points (see again green curve/points in Fig 3).

Without considering this offset, MCS were carried out with dependent fits of both external chromatograms. The goodness of fit between experiment and simulations were evaluated using a minimum least-squares method similar to the one described in [5]. This entails a large range of possible enthalpies and simulation scaling factors tested. The thereby derived, *preliminary* adsorption enthalpies of both chemical species amount to: $-\Delta H_{ads}^{SiO_2}(\mathrm{TlOH}) = 132\ \mathrm{kJ/mol}$ and $-\Delta H_{ads}^{SiO_2}(\mathrm{Tl}) = 178\ \mathrm{kJ/mol}$. Full consideration of the mentioned offset due to persisting TlOH formation is on-going.

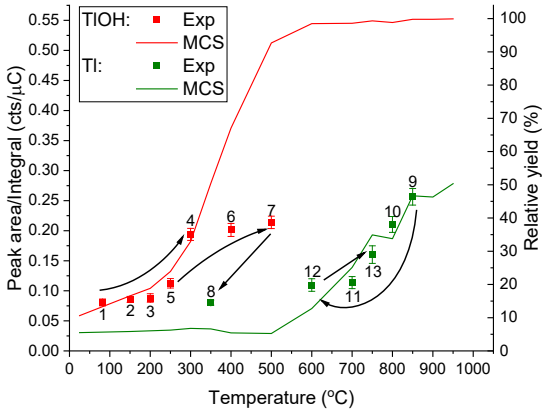

Figure 3. External chromatograms of thallium on silica in O_2/H_2O-added experiments (squares; left axis) overlapped with best current fit (based on MCS; lines; right axis). The experiment order is indicated with numbers and black arrows.

Conclusion

Within one set of experiments, both Tl and TlOH were likely observed with isothermal gas chromatography in preparation for an unambiguous chemical characterization of nihonium. Although data analysis is still on-going, these results illustrate the importance of a thorough preparation for chemical characterization of nihonium. Only based on intensive (online) studies with the lighter homologs experiments can be designed that address conclusively chemical information for the corresponding SHE.

References

[1] R. Eichler et al., *Radiochim. Acta,* **98** (2010), pp. 133-139
[2] Eichler, R., et al., *Nature*, **447** (2007), pp. 72-75
[3] N. V. Aksenov et al., *Eur. Phys. J. A,* **53** (2017), pp. 1-5
[4] A. Yakushev et al. (2021). *Front. Chem.,* **9** (2021), 1002
[5] P. Steinegger et al., *J. Phys. Chem. C,* **120** (2016), pp. 7122-7132
[6] V. Pershina, *J. Phys. Chem. C,* **120** (2016), pp. 20232-20238
[7] A. Serov et al., *Radiochim. Acta,* **101** (2013), pp. 421-425
[8] P. Steinegger et al., *LRC Annual Report 2017* (2018), pp. 12-13
[9] E. E. Tereshatov et al., *New J. Chem.*, **45** (2021), pp. 3377-3381
[10] I. Zvara, *The Inorganic Radiochemistry of Heavy Elements,* Springer Science, 2008
[11] A. S. D'Souza et al., *J. Am. Ceram. Soc.*, **85** (2002), pp. 1499-1504

Electrochemical separation of Co-60 for radioanalytical applications

P. Dutheil (ETHZ/PSI), D. Herrmann (PSI), P. Steinegger (ETHZ/PSI), M. Heule (PSI/ASI)

Introduction

The high activity of Co-60 in activated matrices (e.g., activated steel) can be a problem during routine radioanalysis of gamma- and beta-emitters in samples of different origin. A simple method for quantitative removal of Co-60 would reduce background level in gamma spectrometry significantly and avoid interference with minor beta emitters in liquid scintillation counting. Thus, a good chemical separation is required to provide a reliable quantification of other radionuclides. In contrast to well-established separation procedures, such as ion-exchange chromatography, precipitation and co-precipitation, extraction chromatography or liquid-liquid extraction, we explore here an electrochemical approach. Such electrochemical systems exploit differences in electrochemical potentials for a different selectivity than traditional methods and have the advantages of being more readily automatized and they may be integrated in flow-controlled systems.

Transition metal ions can be separated by taking advantage of the difference of their respective reduction potentials [1]. As an example, cobalt is electrochemically reduced according to the following reaction:

$$\mathrm{Co}^{2+} + 2\,e^{-} \rightarrow \mathrm{Co}$$

Since the standard reduction potential of Cobalt ($-0.280\ V_{vs\ \mathrm{SHE}}$) is higher than that of other, more electropositive elements (e.g., for Cs with a standard reduction potential of $E^0 = -3.026\ V_{vs\ \mathrm{SHE}}$). Thus, Co-60 is expected to reduce readily onto a solid electrode and to be separated from radionuclides of more electropositive elements such as Sr-90, Ba-133, Cs-137 or Am-241. In order to investigate the feasibility of such an approach, cyclic voltammetry (CV) was used to study the reduction of cobalt on glassy carbon electrodes in different electrolytes. The outcome of the studies employing CV led in a second step to the implementation of a separation procedure using controlled-potential electrolysis. This procedure was used for the separation of selected radionuclides. A simple example of which, i.e., the separation of carrier-added Co-60 from Cs-137 is presented here.

Results

Cyclic voltammetry

Several CV cycles were carried out in different electrochemical systems containing stable cobalt ($CoCl_2$, Alfa Aesar). Investigations in acidic aqueous electrolytes (HNO_3 and HCl, Merck) revealed that the reduction of cobalt happened simultaneously with the hydrogen evolution reaction, thus, making it difficult to determine the reduction potential in those media. In chloride containing aqueous electrolytes (KCl and NaCl, Merck), CV led to clear reduction and oxidation peaks (see Fig. 1). This allowed for choosing an adequate electrode potential to be used in a second step in procedures of controlled-potential electrolysis.

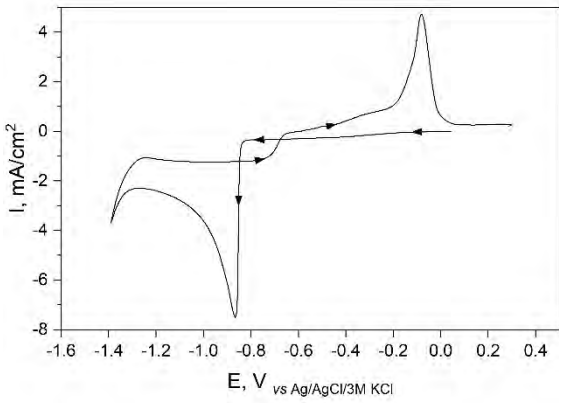

Figure 1: Cyclic voltammogram of 0.01 M Co^{2+} in 0.1 M KCl at a glassy carbon electrode (scan speed: 50 mV/s).

Controlled-potential electrolysis

Carrier-added Co-60 was electrodeposited at a glassy carbon electrode in 0.1 M KCl electrolyte at potentials $< -1.35\ V_{vs\ \mathrm{Ag/AgCl/3M\ KCl}}$ and recovered by electro-oxidation at $0.5\ V_{vs\ \mathrm{Ag/AgCl/3M\ KCl}}$ in a clean 0.1 M HNO_3 solution (see procedure outlined in Fig. 2). Recoveries in each fraction were measured with γ-spectrometry. The procedure yielded high recoveries (> 99%) for electrodeposition times in excess of 7 hours and allowed for good separation of Co-60 from individual co-contaminants like Cs-137, Ba-133, and Sr-85 (see Fig. 3). The procedure of controlled-potential electrolysis required potentials lower than the one found by CV for an exhaustive electrodeposition. The reason for this is the decreasing concentration of Co-60 in the mixture during the electrolysis shifting the Nernst potential and the diffusion kinetics relevant for deposition. Eu-152 could not be separated from Co-60 and was partly co-deposited onto the electrode, probably because of hydroxide precipitation at neutral pH. This suggests that radioisotopes of chemical elements prone to hydrolysis (e.g., Am-241) might behave in the same way. Acidic solutions may be used to avoid such precipitations, probably at the expense of good current efficiency because of the simultaneously occurring hydrogen evolution reaction.

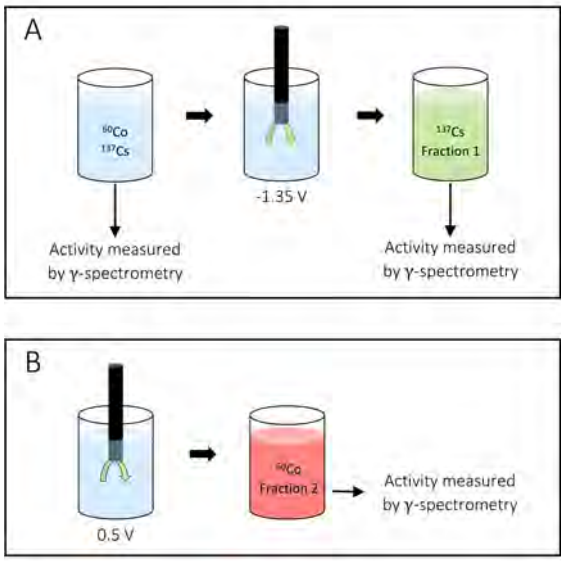

Figure 2: Electrochemical procedure, with **A** the reduction of Co-60 at a glassy carbon electrode (leaving Cs-137 in solution) and **B** the oxidation and removal of Co-60 into a second, clean solution.

Conclusion and outlook

The procedure of controlled-potential electrolysis was successfully used for the removal of Co-60 from simple mixtures of radionuclides at high yields. Such a separation scheme may be used in combination with traditional separation methods to provide complete analytical procedures. In addition, an electrochemical flow-cell setup with a high surface-to-volume ratio will considerably increase the electrodeposition rate and allow for much faster separations [2]. A first flow-cell system was built recently and will be tested (see Fig. 4).

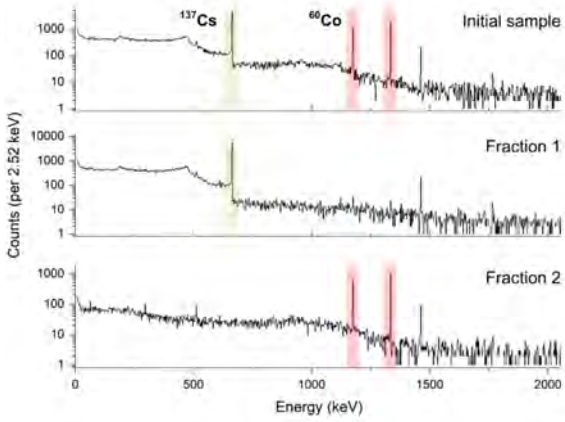

Figure 3: γ-spectra of a mixture of Co-60 (marked in red) and Cs-137 (marked in green) before and after separation with controlled-potential electrolysis in two fraction at $-1.35\ V_{vs\ \mathrm{Ag/AgCl/3M\ KCl}}$ for 8 hours.

The method explored here is highly dependent on the electrolyte, the working electrode material, the presence of coordinating ligands, and the concentration of the deposited element. Consequently, all parameters need to be considered to implement a selective electrodeposition procedure for characteristic samples. One should also keep in mind that mixtures of increasing complexity might behave differently because of the simultaneous deposition of other elements (e.g., Ni, Fe, or Cu). These parameters will be systematically studied, using the above-mentioned flow-cell system.

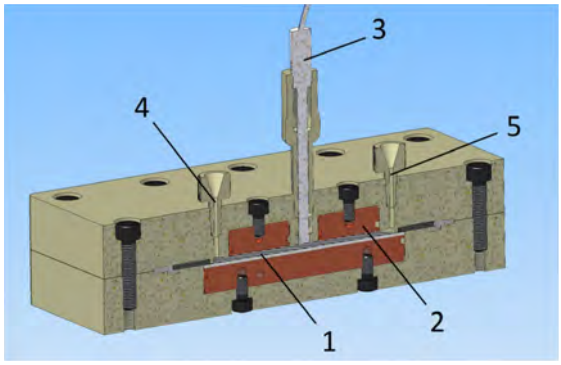

Figure 4: Cross-sectional view of the proposed design for the electrochemical flow-cell in thin-layer mode with 1 the working electrode, 2 the counter electrode, 3 the reference electrode and 4 the inlet as well as 5 the outlet; the same cell can be used in flow-through mode, where the electrolyte flows directly through a porous working electrode.

Acknowledgements

This work is funded by ENSI/PSI-ASI R&D program, contract no. CTR00491.

References

[1] A. J. Bard and L. R. Faulkner, *Electrochemical methods: Fundamentals and applications*, 2nd Ed., 2001

[2] T. Fujinaga and K. Sorin, *Crit. Rev. Anal. Chem.*, **6**(3) (1977), pp. 223-254

Development of the Trace-gas Reaction Analyzer for Chemistry (TRACY)

P. Ionescu (Univ. Bern/PSI), R. Eichler, D. Herrmann (PSI), P. Steinegger, G. Tiebel (ETHZ/PSI), A. Türler (Univ. Bern), J. Wilson (ETHZ/PSI)

Introduction

The study of newly discovered transactinide elements ($Z \geq 104$) is a fundamental topic of radiochemistry. Beginning in the 1960s, scientists have been racing to create the next-heavy element in the periodic table using heavy-ion-induced nuclear fusion-evaporation reactions to achieve this goal [1]. The chemistry of these superheavy elements is of high interest as relativistic effects, increasing with atomic number *Z*, influence chemical properties. Although the drive to discover ever-heavier elements and their chemistry is strong, past experiments have been shown to distinctly suffer from residual impurities in the mobile phase in gas-chromatographic investigations [2]. A need for better understanding the chemical behavior in single-atom gas chromatography (GC) gave rise to the development of the Trace-gas Reaction Analyzer for Chemistry (TRACY). The system is capable of analyzing gas compositions of a chromatography experiment in real-time, while also being able to intentionally functionalize or dope the carrier gas. The system was intended for use in a joint experiment with the Japan Atomic Energy Agency (JAEA) at their Tandem Accelerator Facility using short-lived mercury radioisotopes, produced in nuclear fusion-evaporation reactions. However, due to travel restrictions in Spring 2021, the experiment has been postponed.

Experimental Setup

The TRACY setup (see Fig. 1) for GC was modelled after the gas loop system of the Cryo On-Line Detector (COLD) used in the first successful chemical characterization of Cn [4]. On-line, evaporation residues are thermalized in the carrier gas flushed through a recoil chamber. H_2, O_2 and H_2O can be selectively dosed into the otherwise inert carrier gas (He/Ar mixture, 70/30), allowing to assess their effects on the transport yield. The evaporation residues are transported from the recoil chamber via an in-situ volatilization oven [5] followed by a Perfluoroalkoxy PFA capillary at room temperature to a COLD-like detector array (half-sized version of the COLD). Thus, fusion products only come into contact with quartz and PFA surfaces before entering the detector array. The gas composition is monitored in real-time using an atmospheric pressure mass spectrometer (MKS Cirrus®2). Gas flows in the loop can be established between 0.8 l/min and 2.2 l/min. The setup offers particularly short dry-down times, i.e., the dew point reaches -100°C within less than 24 hours.

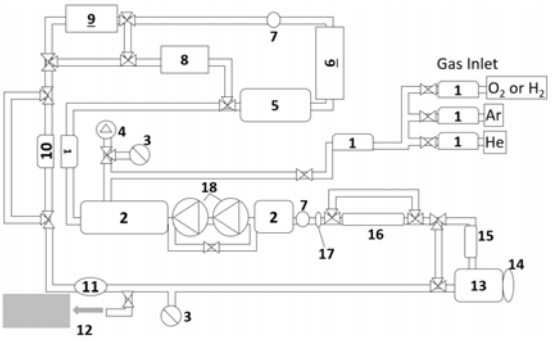

Figure 1: Schematic of the TRACY with **1** the mass flow controller, **2** the buffer volume, **3** a pressure gage, **4** the vacuum pump, **5** a placeholder for optional equipment, **6** the SICAPENT® gas cleaning cartridge, **7** a particle filter, **8** the gas humidifier, **9** the Ta getter oven, **10** the SAES MicroTorr 902 gas cleaning cartridge, **11** the dew point meter, **12** the mass Spectrometer, **13** the recoil chamber (optional), **14** the target (optional), **15** the aerosol filter oven (optional), **16** the α-particle & SF detector array (or general GC experiment), **17** a charcoal trap, **18** the loop pump(s).

Commissioning of TRACY at PSI (offline experiments)

^{197m}Hg was produced at the IP2 beam line of the Paul Scherrer Institute in Switzerland via the nuclear reaction $^{nat.}$Au(p,n)^{197m}Hg to establish the transport efficiency of a carrier gas doped with oxygen as a contaminant (offline experiments). The irradiated gold foil with the embedded ^{197m}Hg was placed in a starter oven connected to the TRACY (instead of 13 in Fig. 1) and heated to ≈500°C to release the radioisotope into the gas stream. This mimicked the recoil chamber as used for online experiments with short-lived radionuclides (e.g., radioisotopes of superheavy elements). The thermally released ^{197m}Hg was then transported to and collected on a charcoal trap (instead of 16 in Fig. 1), where it was quantified using γ-spectrometry.

Results from preliminary tests

The ability to dope and monitor the carrier gas in real-time was tested. The detection limit for the oxygen and water content in the carrier gas was determined with respect to the mass spectrometric measurements (the direct quantification of the gas composition by atmospheric mass spectrometry is not possible due to, e.g., quenching effects).

Oxygen doping

A series of well-known O_2-volumes were added to the known 6.0 L total volume of TRACY. Based on a

series of different admixtures, a calibration curve was recorded (see Fig. 2). The oxygen detection limit was established to be 100 ppb.

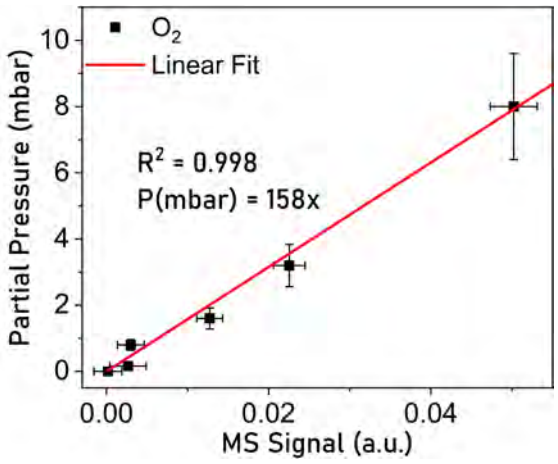

Figure 2: Calibration curve for the careful oxygen additions to the total volume of the TRACY setup as a function of the corresponding mass spectrometric measurements (arbitrary units).

To determine the effect of the oxygen content on the transport efficiency of ^{197m}Hg from a simulated recoil chamber to the detector, relative transport efficiencies were measured (with respect to the lowest O_2-content; see Tab. 1).

TABLE 1: The relative transport efficiency of ^{197m}Hg with respect to the oxygen content in the carrier gas.

O_2 [PPM]	RELATIVE TRANSPORT EFFICIENCY
< 0.1	100%
2720 (540)	56%
≈500'000	1%

Water doping

In a second step, the humidifier was tested with respect to its ability to control the water content in the carrier gas of TRACY. To do so, a second calibration curve was recorded in order to relate the added water contents (determined using the dew point meter) to the mass spectrometric measurements. The detection limit of water in the gas loop was determined to be > 600 ppb.

Conclusion

The TRACY gas loop was successfully built-up and used to selectively dope an otherwise inert carrier gas with water and oxygen contaminants. The detection limits of the used mass spectrometer in the current setting for oxygen and water was established at ≈100 ppb and ≈600 ppb, respectively. It has been demonstrated that the transport efficiency of ^{197m}Hg can be readily influenced by the addition of oxygen. Thus, the TRACY gas-loop system for GC experiments is not only suitable for the use in future online experiments (e.g., at an accelerator facility), but also qualifies for its employment in every-day offline investigations (radiochemical laboratory). TRACY will proof instrumental for studying the effects on the transport yields in dependence of residual gas impurities in experiment with single atoms. Furthermore, TRACY was designed in a compact form for easy transportability to international accelerator facilities (such as e.g., the Tandem Accelerator of JAEA).

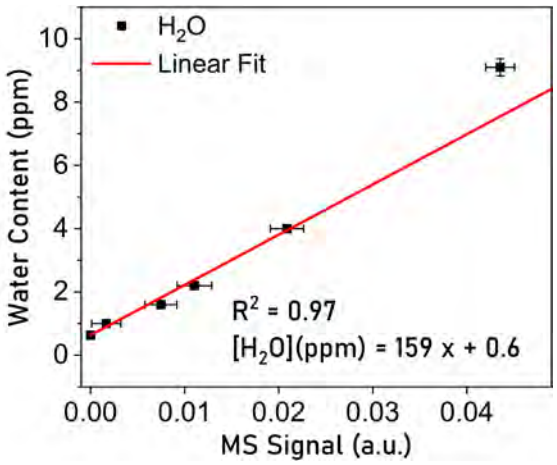

Figure 3: Calibration curve relating the measurements of the dew point meter (H_2O-content adjusted with humidifier) to the mass spectrometry measurements.

References

[1] M. Schädel, D. A. Shaughnessy (eds.), The Chemistry of the superheavy elements, 2nd ed., Springer-Verlag, Berlin Heidelberg, 2014
[2] R. Eichler, *J. Phys.: Conf. Ser.*, **420** (2013), pp. 012003
[3] R. Eichler et al., *Angew. Chem., Int. Ed.*, **47** (2008), pp. 3262–3266
[4] R. Eichler et al., *Nature*, **447** (2007), pp. 72–75
[5] C. E. Düllmann et al., *Nature*, **418** (2002), pp. 859–862

First Results on the Characterization of Targets Prepared by the Coupled Reduction Method for Heavy-ion-beam Irradiations

E. Pishchalnikova (FLNR/JINR, MSU), N. V. Aksenov (FLNR/JINR), R. Eichler, E. Maugeri (PSI), E. Müller Gubler (PSI/LNB), P. Steinegger, G. Tiebel, I. Zivadinovic (ETHZ/PSI)

Introduction

Currently, the synthesis of new superheavy elements in nuclear fusion-evaporation reactions requires long-term irradiations of actinide targets with high-intensity heavy-ion beams. The induced stress (e.g., by the high temperatures, radiation-enhanced diffusion, sputtering and chemical reactions) leads to the destruction of the targets over time [1]. Increasing ion beam intensities of new accelerators, such as the DC-280 of the Flerov Laboratory in Dubna, intensify the problem, thus demanding for a stable target technology. It has been reported that intermetallic compounds exhibit superior properties [2]. The aim of this work is to refine the method of coupled reduction (CR), which was successfully employed for intermetallic target development in the past [3].

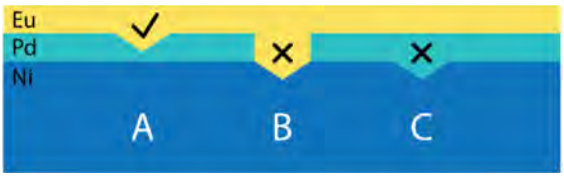

Figure 1: Refinement strategy of CR using a thin layer of Pd deposited onto of a suitable backing foil (e.g., Ni): electroplated element (e.g., Eu) is envisaged to form an intermetallic compound with the underlying Pd by CR (A), whereas a diffusion into the backing foil (B) has to be minimized; diffusion of Pd into the backing is likewise unfavorable (C).

In order to prevent the target (radio)isotope to spread across the entire backing foil [3], we envisage to implement a layered structure of defined composition to confine the (radio)isotope of interest in a thin (inter)metallic Pd-layer on top of our backing foil (strategy outlined in Fig. 1). By combining this with a selected backing material (based on low/positive solid solution enthalpies as calculated by the MIEDEMA approach [4]) as well as under full consideration of the conditions set for a target for synthesis experiments (e.g., low *Z*), one may prevent the above-mentioned spreading of the target (radio)isotope across the backing foil. Using an oxide layer between Pd and the backing could further improve constraining the target material in a thin metallic layer on the backing foil. However, this may come at the cost of mechanical stability. The targeted refinement of the approach presented in [3] may lead to a suitable method for the preparation of high-power (radioactive) targets that meet the requirements of today's experiments at new accelerator facilities.

Experiment details

Two samples resulting from two different CR approaches are presented. One was prepared according to [3] for comparative reasons, using a 25 µm thick Pd foil ("Eu/Pd"). The second sample relied on the approach presented above, employing a thin Pd-layer (800 nm) evaporated on a 25 µm Ni backing foil (Eu/Pd/Ni"). Nickel was chosen due to its low atomic number as well as based on the calculated much lower solution enthalpy of Eu at infinite dissolution in Ni of $\Delta H_{sol}^{\mathrm{Eu/Ni(s)}} = -56\ \mathrm{kJ/mol}$ as compared to the value in Pd of $\Delta H_{sol}^{\mathrm{Eu/Pd(s)}} = -333\ \mathrm{kJ/mol}$ [4]. For both samples, europium was electroplated on palladium by molecular electroplating (MEP) in a Teflon cell with a diameter of 13 mm regarding the deposition area. Before deposition, the foils were cleaned with acetone and ethanol, followed by 10 minutes in the UVO cleaner to remove organic surface contaminations. Afterward, the samples were placed on a Ta boat inside a Ni tube before being subjected to CR in a flow of H_2 at 1100°C (see Fig. 2).

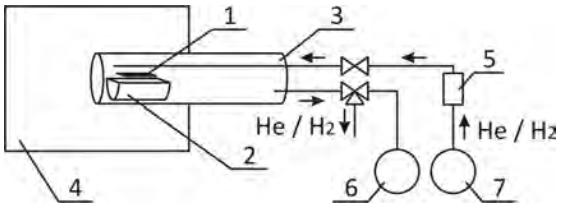

Figure 2: Setup for CR with the sample (1), the Ta block (2), the sealed Ni tube (3), the furnace (4), the mass flow controller (5), the vacuum pump (6), the gas supply line (7).

Both samples were analyzed by scanning electron microscopy (SEM; NVision40, Zeiss) coupled with energy dispersive X-ray spectroscopy (EDX).

Results and discussion

The SEM images of both samples before and after CR are shown in Fig. 3 (a, c vs. b, d). Before CR the surface morphology of both samples Eu/Pd and Eu/Pd/Ni reveal an island-like structure, that is typical for target surfaces prepared by MEP using isopropanol as solvent [5]. After CR both samples have a metallic appearance. The corresponding SEM images illustrate the similar surface morphology modification after CR, when comparing the two samples. The surface of both samples is characterized by the

presence of clearly visible grain boundaries of the Pd crystal phase, which is typical for metals, metal alloys, or intermetallic compound surfaces.

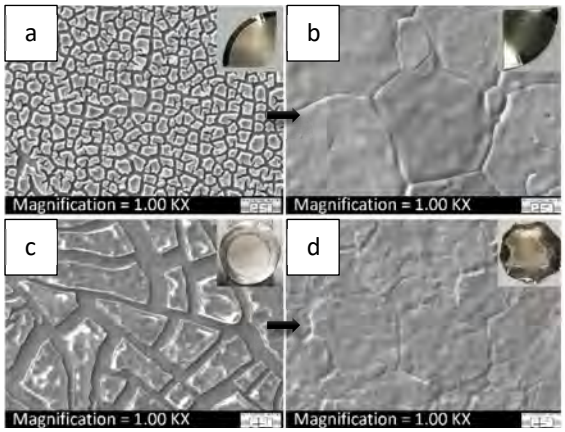

Figure 3: SEM pictures of the Eu/Pd (top row) and the Eu/Pd/Ni (bottom row) sample, before (a, c) and after (b, d) the CR process for 30 min, respectively; photographs of each investigated sample are depicted on the top corner f each SEM picture.

SEM images of the Eu/Pd/Ni sample with a 5000-fold magnification before (left side) and after (right side) CR are presented in Figure 4. We additionally studied the sample using EDX in order to identify the distribution of different elements, namely Eu, O, Pd, and Ni. Before CR (see Fig. 3, left side), Eu and O are observed in the same area, thus being deposited as hydroxidic/oxidic europium species, whereas Pd appears underneath these Eu-O-islands. These results are in good correspondence with [5]. The Ni K_{α}-signal from the backing foil was clearly distinguished too.

After the CR process, the sample acquired the above-mentioned surface morphology with visible grain boundaries. EDX analysis revealed a homogenous distribution of Eu, Pd, and Ni across the sample surface (see Fig. 4, right side) and the absence of oxygen (represented by less than 1% of the mass concentration). It follows that the reduction of Eu and its subsequent diffusion in the underlying Pd-layer was successful. These observations for the Eu/Pd/Ni sample are in agreement with EDX measurements of the Eu/Pd sample, where obtained elemental maps feature a similar distribution regarding Eu, O and Pd before and after the CR process.

Conclusion and Outlook

We successfully produced a thin Pd-Eu-layer (likely an intermetallic phase) using refined CR approach (see Fig. 1). The obtained sample was characterized using SEM coupled with EDX. This analysis approach allowed for determining the surface morphology as well as the elemental distribution and indications on chemical compound formation. Further studies will analyze such samples by SEM coupled with EDX and the focused ion beam technique, in order to get information on the Eu distribution across the thickness of the sample. Additional XPS and XRD studies will be used to retrieve further chemical and crystallographic information, respectively.

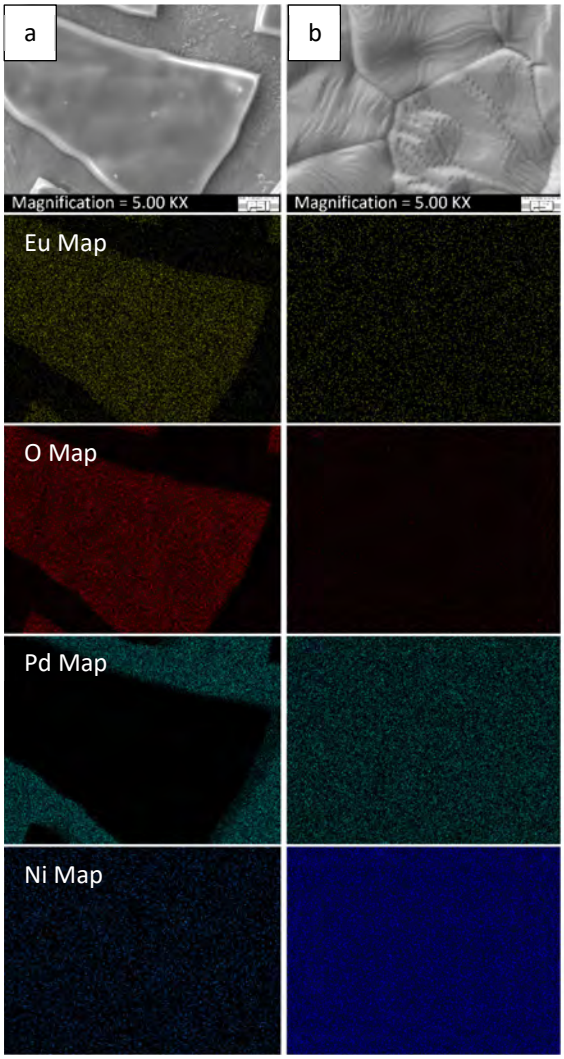

Figure 4: SEM images (top row) and EDX elemental maps of the Eu/Pd/Ni sample before (left side, a) and after (right side, b) CR; elemental EDX-maps of Eu (yellow), O (red), Pd (cyan), Ni (blue) are shown.

References

[1] S. N. Dmitriev et al., *J. Radioanal. Nucl. Chem.*, **305** (2015), pp. 927-933
[2] C. C. Koch, *Mater. Sci. Eng., A.*, **244** (1998), pp. 39-48.
[3] I. Usoltsev et al., *Nucl. Instrum. Methods Phys. Res., Sect. A*, **691** (2012), pp. 5-9
[4] H. Rossbach et al., *Mater. Sci. (B2240)*, ZFK-527 (1984), pp. 65
[5] A. Vascon et al., *J. Radioanal. Nucl. Chem.*, **299** (2014), pp. 1085-1091

DGFRS III (GRAND) simulation using DSIM: The ^{48}Ca on ^{242}Pu reaction using a He-filled separator

R. Eichler (PSI), P. Steinegger (ETHZ/PSI), O. N. Malyshev, A. V. Yeremin (FLNR/JINR)

Introduction

In the previous annual report [1], we have established the DSIM code for the Dubna Gas-Filled Recoil Separator II simulating the trajectories of recoiling evaporation residues produced in heavy ion induced nuclear fusion-evaporation reactions from targets of variable thicknesses. This code is based on the ion transport code (BSIM), developed at LBNL for describing the Berkeley Gas-filled Separator [2]. Such simulations support the optimization of the magnetic field settings to obtain highest possible transmission yields into the focal plane at desired image sizes. Furthermore, the simulation provides the energy distribution of the recoils arriving after their separation in the focal plane. The understanding of these parameters is crucial for the design of chemical devices: Their inner volume needs to be optimized in order to minimize losses during gas-phase transport of thermalized nuclear reaction products [3]. Here, we present the results of simulations of the Dubna Gas-filled Recoil Separator III (GRAND), a new helium-filled separator recently commissioned at the Superheavy Elements Factory (SHE Factory) of the Flerov Laboratory of Nuclear Reactions, Dubna, Russian Federation [4]. A significant difference between the designs of separators DGFRS II and III is related to the additional, symmetric dipole magnet at the end of DGFRS III. This allows for switching between two separate focal-plane positions at ±15° bending angle. Whereas one is reserved for physics experiments, the second position is dedicated for chemical investigations.

Simulation

The initial ion distribution and trajectories of the nuclear reaction products at the beginning of the separator were generated for a 0.56 mg/cm^2 $^{242}PuO_2$ target using SRIM2013 [5]. Initially, starting points (i.e., points of creation) of evaporation residues inside the target need to be determined. This was achieved by calculating the energy loss of the incident 252 MeV ^{48}Ca ion beam in the Ti backing (0.90 mg/cm^2) as well as the $^{242}PuO_2$ target. A superposition with the known excitation function of the nuclear reaction [6] defines the local distribution of the origin of the recoiling products within the target within an assumed round beam spot of 5 mm inner diameter. The products are scattered through the remaining part of the target thickness losing part of their momentum, defining their magnetic rigidity. The most likely Bρ of the recoiling ^{287}Fl into the 0.7 mbar He was calculated as 2.179 Tm.The energy and angular distribution of 10'000 recoiling ions is calculated as input for DSIM using SRIM [6]. Subsequently, the statistical electron exchange and straggling of the ion with the helium filling gas held at 0.7 mbar [2] is superimposed with the momentum of the ions under the influence of the magnetic fields of the GRAND (QDQQD-type). The simulation generates detailed information about the place, their momentum in the separator as well as the energies of the recoiling ions in the focal plane, as function of the magnetic settings and the magnetic rigidity of the products. We will present here, results of simulations using the evaporation residues produced in the nuclear fusion reaction $^{242}\mathrm{Pu}(^{48}\mathrm{Ca}, 3\mathrm{n})^{287}\mathrm{Fl}$ $(E_{COT} = 242.5\ \mathrm{MeV})$ [6] for the optimization of the forthcoming transactinide gas-phase chemistry experiment at this dedicated facility with Fl/Cn.
DSIM yields product distributions in the focal plane as functions of the transmission yields

Results: ^{242}Pu(^{48}Ca, 3n)^{287}Fl (prediction)

The magnetic rigidity of the product is decisive for the magnet settings of D1 and D2, which was thus kept constant at $\mathrm{D1} = 530\ \mathrm{A}$ and $\mathrm{D2} = 447\ \mathrm{A}$ for both CONFIG I and CONFIG II, to position the products in the center of the focal plane. A screening for the optimum configuration of the quadrupole magnets was performed to obtain the smallest focal plane images with the highest transmission yields. Therefore, a parameter sweep over quadrupole lens currents $\mathrm{Q2}$ & $\mathrm{Q3}$ (see Fig. 1) was performed using a constant setting for $\mathrm{Q1} = 300\ \mathrm{A}$.

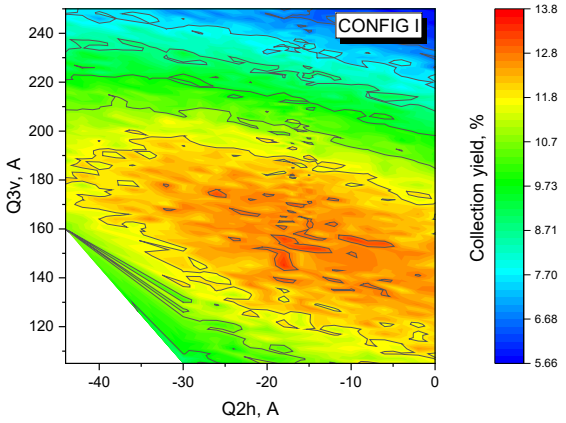

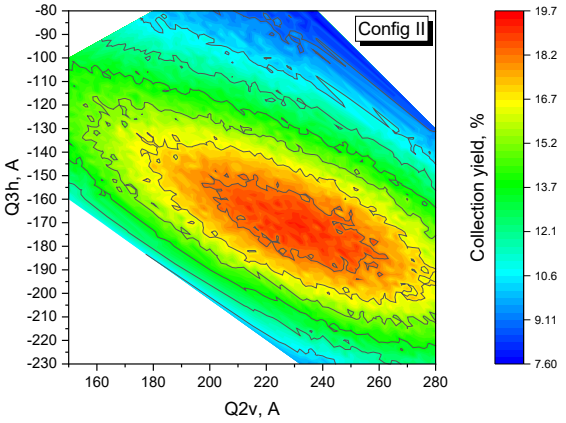

Figure 1: Collection efficiency into a $8 \times 6\ \mathrm{cm}^2$, oval-shaped recoil chamber as a function of quadrupole lens currents $\mathrm{Q}2h$ and $\mathrm{Q}3v$ (CONFIG I, upper panel) and $\mathrm{Q}2v$ and $\mathrm{Q}3h$ (CONFIG II, lower panel)

Thus, the "optimum" magnet current configurations of the GRAND separator with a $\mathrm{Q_vDQ_hQ_vD}$ (CONFIG I) and $\mathrm{Q_vDQ_vQ_hD}$ (CONFIG II) arrangement were determined (see Tab. 1).

TABLE 1: The currents for the quadrupole lenses in configurations CONFIG I and CONFIG II; a negative current corresponds to a horizontally focusing quadrupole. The dipole settings were set at $\mathrm{D}1 = 530\ \mathrm{A}$ and $\mathrm{D}2 = 450\ \mathrm{A}$

CONFIG	Q1	Q2	Q3
I	300 A	-18 A	160 A
II	300 A	220 A	-165 A

Thus, for both configurations the transmission efficiencies as function of recoil chamber size was generally assessed (see Figure 2). Here, the simulated shapes of the optimized focal plane images for configurations CONFIG I and CONFIG II of GRAND are shown. The optimization focus was put on the highest transmission yield into the smallest focal plane area. The planned chemistry experiment (spring 2022) relies on a fast transport of short-lived ^{287}Fl, having a half-life of about 0.5 s. Therefore, the flushing time of the Recoil-Transfer Chamber (RTC) was investigated in [3]. From the herein derived focal plane image size at highest transmission yields, an optimum RTC covers an area of $8 \times 6\ \mathrm{cm}^2$ in the focal plane of DGFRS III. Based on the obtained energy distribution of evaporations residues in the focal plane, a depth of 1.5 cm was chosen. Stopping range calculations of evaporation residues within the RTC volume will further support the selection of the gas mixture and the pressure in the RTC for a fastest transfer of Fl into the COLD array (thermochromatography detector). Test experiments are planned at FLNR in spring 2022 to bolster the drawn conclusions by experimental data.

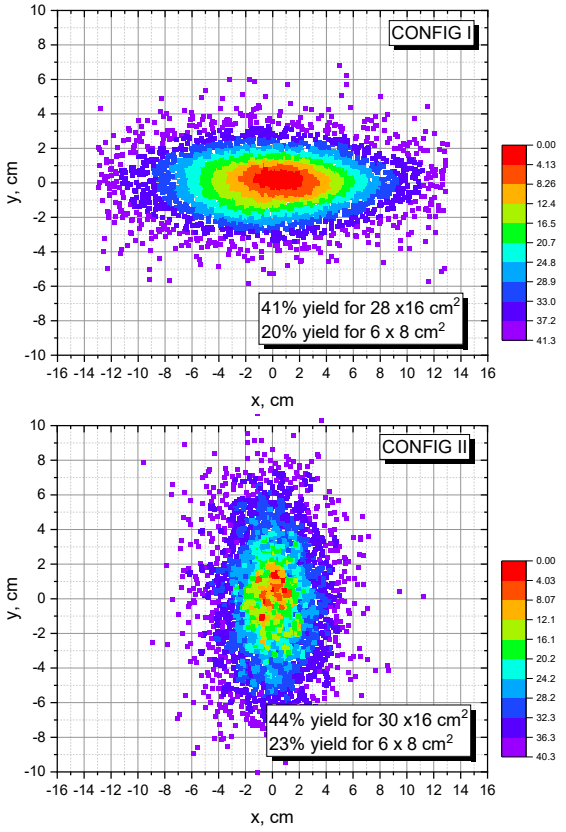

Figure 2: Distributions of 10'000 ^{287}Fl ions passing DGFRS III in the focal plane with a $\mathrm{Q_vDQ_hQ_vD}$-configuration (CONFIG I, upper panel) yielding 20% transmission and a $\mathrm{Q_vDQ_vQ_hD}$-configuration (CONFIG II, bottom panel) yielding 23%. For configurational details, refer to Tab. 1.

With a transmission yield of 23% (CONFIG II) one would expect for the given conditions – assuming ion beam intensities of about 5 puA – up to three ^{287}Fl ions entering the RTC [3] per day.

The work was performed with support from the Russian Federation Scientific Research Work grant НИР № 500/3652.

References

[1] R. Eichler et al., *Annual report LRC 2020,* pp. 11-12
[2] K. E. Gregorich, *Nucl. Instrum. Methods Phys. Res., Sect. A*, **711** (2013), pp. 47-59
[3] P. Steinegger et al., *Annual report LRC 2021*, pp. 18-19
[4] A. G. Popeko, *Nucl. Instrum. Methods Phys. Res., Sect. B*, **376** (2016), pp. 144-149
[5] J. F. Ziegler et al., *Nucl. Instrum. Methods Phys. Res., Sect. B*, **268** (2010), pp. 1818-1823
[6] Yu. Ts. Oganessian, *J. Phys. G: Nucl. Part. Phys.*, **34** (2007), pp. R165-R242

The Design and Analysis of a Recoil Transfer Chamber for Fl and Cn

P. Steinegger (ETHZ/PSI), R. Eicher, D. Herrmann (PSI)

Introduction

In preparation of the first chemistry experiment at the new Superheavy Element Factory of the Flerov Laboratory of Nuclear Reactions (FLNR), Dubna, Russian Federation, a recoil transfer chamber (RTC) was designed. The design was optimized for fastest transport times of thermalized nuclear reaction products, e.g., ^{287}Fl with $t_{1/2} \approx 0.3$ s using finite element analysis with COMSOL Multiphysics [1]. Computations were carried out on the Euler cluster of ETH Zürich.

Geometry of the Recoil Transfer Chamber

The cross sectional area (gray area in Fig. 1 corresponding to the Mylar® entrance window) of the RTC represents a compromise between largest coverage of the focal plane image size [2] of the Dubna Gas-Filled Recoil Separator III (GRAND) and a smallest inner volume of the RTC. The inner volume is furthermore restricted by the stopping range of the penetrating evaporation residues in an assumed argon atmosphere.

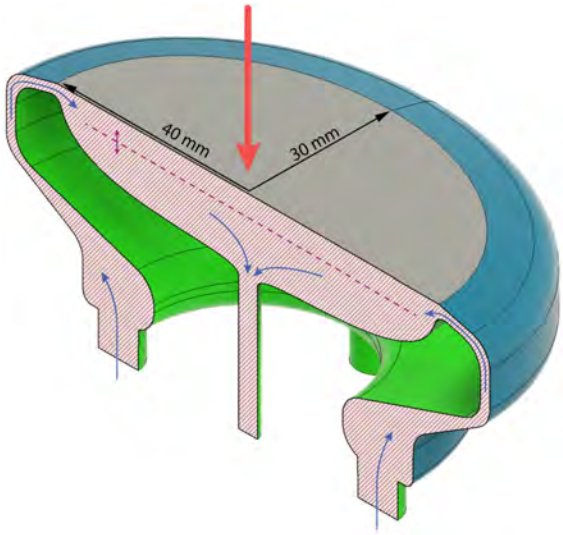

Figure 1: Sliced view of the inner volume of the RTC as a basis for the finite element analysis with the small blue arrows indicating the argon gas flow (four identical inlets and one outlet with an inner diameter of 4 mm), the red arrow representing the pathway of arriving evaporation residues; the size of the ellipsoidal cross section of the RTC (gray area) is likewise indicates. The dashed violet line represents the ellipsoidal starting face (principal axes: $70\ \text{mm} \times 50\ \text{mm}$) of the 10'000 particles used to simulate the flushing out times from different positions of the starting face (i.e., different distances from the entrance window).

The inner volume, as derived from Autodesk Inventor, was simplified within COMSOL using a variety of virtual geometry operations (e.g., create composite faces). This led to a stable meshing procedure, needed for the following modelling steps.

Internal flow

The internal flow at 2 slm of argon was modelled using the kω turbulence flow model of the computational fluid dynamics (CFD) module of COMSOL (see Fig. 2). These required a manually introduced boundary layer mesh, which was complemented by a CFD-matched ultrafine mesh for the remaining volume.

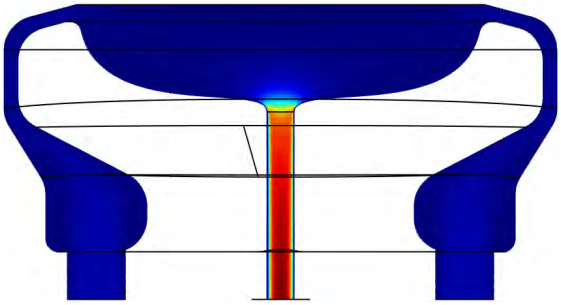

Figure 3: Sliced view along the short axis of the ellipsoidal chamber showing the flow pattern inside the RTC at 2 slm of argon (4 inlets and 1 outlet); the resulting flow speeds reach values from 0 m/s (dark blue areas) up to 4 m/s (dark red areas).

Whereas turbulences were aimed at in the circular volume directly after the four inlets to homogenize the inflow, a steady flow is needed in the ellipsoidal chamber for a smooth and uniform flushing-out of the thermalized nuclear reaction products (see Fig. 3).

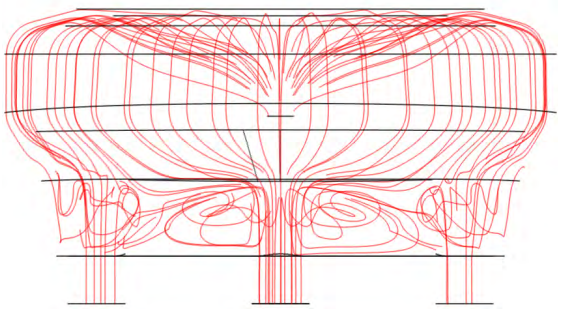

Figure 3: Side view along the short axis of the ellipsoidal chamber showing the stream lines (red lines) inside the RTC at 2 slm of argon (four inlets and one outlet).

Flushing-out times

In order to derive associated transport times of thermalized nuclear reaction products out of the presented RTC at 2 slm (standard liter per minute) argon, particle tracing calculation were carried out with the corresponding module of COMSOL. Thereto, the trajectories of 10'000 particles were computed at different injection depths representing different penetration length of stopped evaporation residues. At these injection depths each time 10'000 particles were randomly distributed on an ellipsoidal face (principal axes: 70 mm $\times$ 50 mm) positioned at different distances (1 to 9 mm) from the entrance window (see Fig. 1).

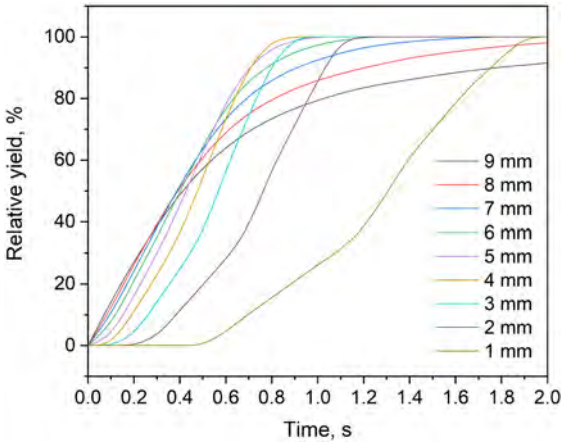

Figure 4: Results of the parametric sweep (1 mm to 9 mm distance of the starting face from the entrance window) showing the relative yield, as collected at the outlet face, as a function of time.

The parametric sweep (10'000 particles per distance of the starting face from the entrance window) of this time-dependent study was computed in steps of 0.1 s in a time interval from 0 seconds to 2 seconds (see Fig. 4).

Conclusions

The results indicate that evaporation residues, which are stopped close to the entrance window, lead to longer residence times within the RTC. This would be particularly unfortunate for the rather short-lived ^{287}Fl with $t_{1/2} \approx 0.3$ s. However, extrapolated stopping range calculations for ^{287}Fl using SRIM [3] lead to penetration depths between 3 and 8 mm (see Fig. 5). The latter were based on an initial energy and angular distribution of nuclear reactions products emerging at the focal plane of GRAND as obtained by the DSIM program [2].

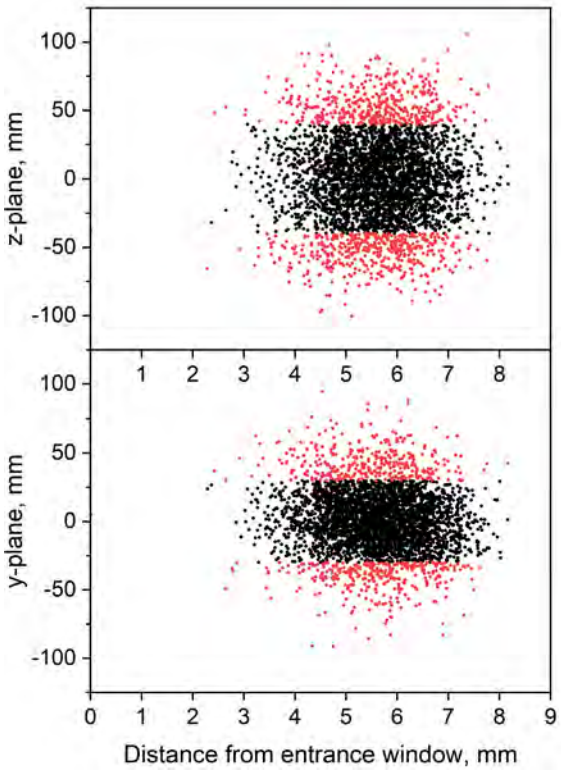

Figure 5: Penetration depth of ^{287}Fl in the RTC at 1 bar argon after a 3 µm Mylar entrance window as obtained with SRIM (red dots lay outside of the RTC cross sectional area); the initial energy and angular distribution was obtained with DSIM [2].

The same calculations have been carried out for slight modifications of the geometry presented in Fig. 1. These will be concluded in the beginning of 2022, thus allowing for a swift production of the optimum RTC and its employment during the upcoming experiments with flerovium and copernicium in spring 2022.

References

[1] COMSOL Multiphysics 5.5 (via Euler@ETHZ)
[2] R. Eichler et al., *LRC Annual Report 2021*, pp. 16-17
[3] J. F. Ziegler et al., *Nucl. Instrum. Methods Phys. Res., Sect. B*, **268** (2010), pp. 1818-1823

First determination of the excitation function for the $^{nat}V(p,X)^{26}Al$ and $^{nat}V(p,X)^{41}Ca$ reactions at high proton energies

M. Veicht (EPFL/PSI), I. Mihalcea (PSI), C. Vockenhuber, P. Gautschi, S. Maxeiner (ETHZ), J.C. David (Univ. Paris-Saclay, IRFU, CEA), S. Chen (SFU), D. Schumann (PSI)

Introduction

From the very first experiment-based cross-section determination for spallation products from vanadium (^{nat}V) targets, reported in 1953 [1], an ever-increasing number of spallation products have been investigated. Nevertheless, cross-section data for the production of ^{26}Al and ^{41}Ca from this target material remain elusive. This lack of data is possibly caused by the difficulties in detection and quantification of the two radionuclides as spallation products.

The ^{26}Al radionuclide, decaying with the emission of a very distinct, high energetic gamma-line at 1808.7 keV ($I\gamma$ = 0.9976), has a relatively long half-life of $7.17(24)\cdot10^5$ y. This makes activity determination using γ-ray spectrometry close to impossible unless a sufficient amount of this isotope is produced. Similar difficulties are encountered for ^{41}Ca ($T_{1/2}$ = $9.94(15)\cdot10^4$ y), which decays via electron capture (X-rays with < 4 keV) only. To mitigate these issues, our focus was first on the radiochemical separation to produce pure fractions and secondly, to utilize accelerator mass spectrometry (AMS) for determining the specific number of produced atoms with high precision and at a very low detection limit. Although AMS requires efforts in the sample preparation, it became more accessible and available for routine analyses. Measurement methods for the two presented nuclides were first developed by Kilius et al. 1979 [2] and Fint al. 1936 [3] for ^{26}Al, and ^{41}Ca, respectively.

In this work, the excitation functions for ^{26}Al and ^{41}Ca were calculated using the Liège Intranuclear Cascade (INCL)/ABLA algorithm and compared to the experimental values. Such experimental data are vital for nuclear databases and thus help improve the theoretical models.

Experimental

The target material consisted of discrete vanadium metallic discs (99.75% purity) with a diameter of 1.5 cm and a mass averaging at 0.14 g. The origin of the irradiated targets, the irradiation conditions, and chemical processing down to the dissolution of the metallic vanadium targets have been previously reported [4]. The development and implementation of the wet radiochemical separation process were also described in a previous report [5].

AMS sample preparation and measurement

Following the radiochemical separation, the resulting ^{41}Ca solutions were evaporated to dryness using 5 ml conical glass vials by successively adding the solution. To raise the temperature to 150°C, an electric heating mantle was used. The solid residues were dissolved in 0.5 ml H_2O, and the resulting solutions were transferred into 2 ml centrifuge plastic vials. Moreover, 0.25 ml 1M HF was added, and the solutions were left undisturbed overnight for CaF_2 precipitation. The dispersion was then centrifuged, and the supernatant was discarded. The solid residue was dispersed again in 0.75 ml H_2O, and the centrifugation process was repeated. The obtained solids were dried for 24h at 80°C before being sent to ETHZ-LIP for the AMS analysis. The AMS measurement was performed at the 300 kV MILEA AMS facility [6], following the procedure described by Vockenhuber et al. [7]. A ^{41}K correction based on ^{39}K measurement was applied using a factor of 0.05. Standards B10 and B9 were used for normalization. Nominal values are taken from [8]. A blank correction based on the average of three blanks was applied, and a sample scatter of 3% was added to the uncertainty budget.

For the separated ^{26}Al solutions, the initial sample volume of 30 ml was reduced to 5 ml by evaporation. The concentrated solutions are transferred to 50 ml conical centrifugation vessels, and for each, the pH is adjusted to 9.6(3) with a half-concentrated ammonia solution. The resulting precipitate was allowed to settle overnight, the solution was centrifuged, the supernatant was discarded, and the solids were dried at 105°C in a glazed crucible for 12h. Once dried, the solids are calcined at 900°C for 8h before being sent for AMS analysis. The nominal $^{26}Al/^{27}Al$ ratio of the internal standard ZAL94N is $4.80(18)\cdot10^{-10}$. The nominal $^{26}Al/^{27}Al$ ratio of the internal standard ZAL02 is $4.64(1)\cdot10^{-11}$. The internal standard is calibrated against the primary standard KN 01-4-1 (nominal $^{26}Al/^{27}Al$ ratio $7.444(268)\cdot10^{-11}$ by [9]). The half-life of ^{26}Al was considered $0.705(24)\cdot10^6$ years.

Results and Discussion

The theoretical calculations predicting cross-section values for the $^{nat}V(p,X)^{26}Al$ and the $^{nat}V(p,X)^{41}Ca$ reactions were performed using the Liège Intranuclear Cascade model INCL++ [10, 11] combined with the

de-excitation codes ABLA07 [12]. These combined models were previously used to calculate the production yields in spallation reactions [13].

Generally, the AMS measurements provide isotopic ratios between the artificially produced nuclide and a naturally abundant one, present as an added carrier. For our experiments, the determined ratios were $^{26}Al/^{27}Al$ and $^{41}Ca/^{40}Ca$. Their activity (A) was calculated according to Eq. (1) and Eq. (2):

$$A_{^{26}Al} = {}^{^{26}Al}\!/_{^{27}Al} \cdot N_{^{27}Al} \cdot \lambda_{^{26}Al} \quad (1)$$

$$A_{^{41}Ca} = {}^{^{41}Ca}\!/_{^{40}Ca} \cdot N_{^{40}Ca} \cdot \lambda_{^{41}Ca} \quad (2)$$

The obtained activity was then used to obtain the specific nuclide's production cross-section applying Eq. (3):

$$\sigma = \frac{A \cdot e^{\lambda \cdot t_w}}{N_T \cdot \Phi_E (1 - e^{-\lambda \cdot t_{irr}})} \quad (3)$$

This equation was used and described in a previous report [4].

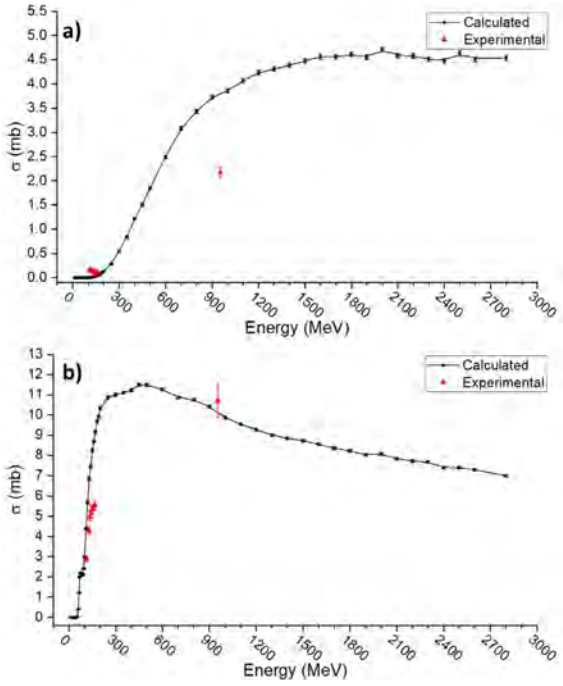

Figure 1: Calculated and experimentally obtained excitation functions, for the nuclear reactions (a) $^{nat}V(p,X)^{26}Al$, and (b) $^{nat}V(p,X)^{41}Ca$

Comparing the predicted excitation function with the experimental values for the production of ^{26}Al, the theoretical model seems to slightly underestimate the cross-sections values at low proton energies (up to 200 MeV) and overestimate them at higher energies. Nevertheless, the experimental data confirm the predicted low reaction probability for ^{26}Al production by vanadium spallation at incident proton energies below 200 MeV. In the case of ^{41}Ca production, the experimental values show an excellent agreement with the predicted theoretical model, confirming both the accuracy of the experimental method as well as the predictive power of the theoretical model. A graphical representation of the excitation functions, showing both the experimental and the predicted cross-sections values, is shown in Fig 1.

Conclusions

Seven vanadium targets were proton irradiated at discrete energies, up to 954 MeV. Following the radiochemical separation, the number of produced ^{26}Al and ^{41}Ca nuclides was determined using AMS. This allowed the calculation of the experimental cross-sections based on the nuclear reactions: $^{nat}V(p,X)^{26}Al$, and $^{nat}V(p,X)^{41}Ca$. The resulting excitation functions were compared with theoretically calculated ones and showed a very good fit for the production of ^{41}Ca, while slight differences are observed for the production of ^{26}Al.

Acknowledgements

This project has received funding from the European Union's Horizon 2020 research and innovation program under the Marie Skłodowska-Curie grant agreement No. 701647.

References

[1] S. G. Rudstam, Lond. *Edinb. Dublin philos. mag. j. sci.*, **44** (1953), pp.1131-1141
[2] L. R. Kilius et al., *Nature*, **282** (1979), pp. 488-489
[3] D. Fink, et al., *Nucl. Instrum. Methods Phys. Res., Sect. B*, **5** (1984), pp. 123-128
[4] M. Veicht et al., *Phys. Rev. C: Nucl. Phys.*, **104** (2021), 014615
[5] M. Veicht et al., *LRC Annual Report 2019* (2020), pp. 30-31
[6] S. Maxeiner et al., *Nucl. Instrum. Methods Phys. Res., Sect. B*, **439** (2019), pp. 84-89
[7] C. Vockenhuber et al., *Nucl. Instrum. Methods Phys. Res., Sect. B*, **361** (2015), pp. 273-276
[8] M. Christl et al., *Nucl. Instrum. Methods Phys. Res., Sect. B*, **294** (2013), pp. 29-38
[9] K. Nishiizumi, , *Nucl. Instrum. Methods Phys. Res., Sect. B*, **223** (2004), pp. 388-392
[10] D. Mancusi et al., *Phys. Rev. C: Nucl. Phys.*, **90** (2014), 05460
[11] A. Boudard et al., *Phys. Rev. C: Nucl. Phys.*, **87** (2013), 014606
[12] A. Kelic et al., arXiv:0906.4193 (2009)
[13] J. C. David, *Eur. Phys. J. A*, **51** (2015), 68

Solubility of cesium iodide in heavy liquid metals

L. Liu (PSI), I. Zivadinovic (ETHZ/PSI), D. Herrmann, A. Vögele, J. Neuhausen (PSI)

Introduction

Heavy liquid metals (HLM) such as molten lead and lead-bismuth eutectic (LBE) present particular interest as the coolant of generation IV nuclear reactors and accelerator-driven systems (ADS) due to their good thermophysical properties (high boiling point and thermal conductivity). However, radionuclides present in the coolant, originating from the activation of the liquid metal itself and from potential contamination with fission products, are a challenge for the safe application of these materials. It is therefore important to investigate the release behavior of these radionuclides from HLM. In the framework of the PASCAL project [1], we are interested in the radioisotopes of cesium and iodine, which are among the most problematic fission products. Compared to the single elements dissolved in LBE, modeling of the chemical equilibrium of the LBE/O/Cs/I system has indicated that Cs and I may show increased evaporation attributed to the formation of CsI [2]. This prediction needs to be experimentally verified, since it is not evident that the chemical equilibrium required to form CsI will be quickly established. In this context, a primary work is to quantify the solubility of Cs-I compounds in heavy metals such as Pb, Bi and LBE. These measurements should provide information on thermodynamic activity, which allows having a better understanding of their behavior.

Experimental

The LBE was supplied by the Belgian Nuclear Research Centre in Mol (SCK·CEN) and represents the material to be used within the MYRRHA project [3]. The lead and bismuth samples used are lead granules (1-5 mm, 99.9999%) and bismuth granules (1-5 mm, 99.9999%) purchased from Chempur. Cesium iodide (99.9%) was purchased from Alfa Aesar. All metals and chemicals were used without pretreatment. Cesium iodide and the individual metal (Pb, Bi or LBE) with a mass ratio of roughly 1:100 were put into a quartz tube under ambient atmospheric conditions. Note that the quartz tubes were washed with strongly oxidizing acids (mixture of H_2SO_4 (97%) and H_2O_2 (> 35%) with 2:1 volume ratio) and dried in a furnace at 100°C in order to get rid of potential surface contaminations. The tubes were then sealed by a torch flame to get the ampoules under vacuum (pressure < 10^{-4} mbar). These sample-containing ampoules were afterwards placed in a furnace whose temperature was set to 1000°C and were heated for 24 hours. During this period, the samples were agitated vigorously several times in order to mix the cesium iodide and the metals. Finally, the ampoules were quenched from 1000°C to room temperature by putting them in a water bath. We obtained three metal rods corresponding to Bi-CsI, Pb-CsI and LBE-CsI mixtures.

The outside surfaces of metal rods were examined by Scanning Electron Microscope (SEM) and Energy-Dispersive X-ray (EDX) techniques to identify the present phases. The bulk metals inside the metal rods were taken out by an electrical drill. These wire-like samples were then sent to be activated by thermal neutrons at the SINQ facility at PSI, together with a pure cesium iodide reference sample. Two irradiations were performed; the first one was 300 seconds in order to produce ^{128}I, while the second irradiation lasted 10'000 seconds to produce measurable amounts of ^{134}Cs. The activities of ^{128}I and ^{134}Cs at the end of the irradiations in the different metal-CsI samples as well as in the CsI reference sample were measured by γ-spectrometry.

Results and discussions

SEM and EDX characterizations

Two samples have been examined so far: the LBE-CsI sample and the Bi-CsI sample (see Fig. 1). For both of them, two phases can be clearly observed from the SEM images, evident from the contrast. From the corresponding EDX analysis, one phase is mainly composed of the metal matrix (LBE or Bi), while the other one consists of Cs and I. Besides this, oxygen is also observed on the surface, especially on the Cs-I phase part. Based on these results, one can conclude that at the end of the reaction, there are still two phases (CsI and the metal), which means that CsI does not fully dissolve in the metal.

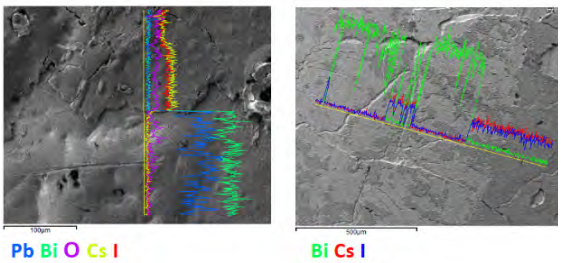

Figure 1: SEM and EDX analysis of metal-CsI mixture sample. Left: LBE-CsI sample; right: Bi-CsI sample.

Mole fractions of I and Cs in LBE, Pb and Bi

Considering that the ratio between the activated cesium and iodine in the metal samples should be the same as that in the reference CsI sample because

they received the same neutron fluence, the mole fraction of I (x_I) and Cs (x_{Cs}) in the metal samples can be approximately calculated according to the following equation (1) and (2);

$$x_I = \frac{n_I\,(\text{metal})}{n_{\text{metal}}} = \frac{A_{128_I}\,(\text{metal})}{A_{128_I}\,(\text{CsI})} \times \frac{m_{\text{CsI}}}{\text{M}_{\text{CsI}}} \times \frac{\text{M}_{\text{metal}}}{m_{\text{metal}}} \quad (1)$$

$$x_{Cs} = \frac{n_{Cs}\,(\text{metal})}{n_{\text{metal}}} = \frac{A_{134_{Cs}}\,(\text{metal})}{A_{134_{Cs}}\,(\text{CsI})} \times \frac{m_{\text{CsI}}}{\text{M}_{\text{CsI}}} \times \frac{\text{M}_{\text{metal}}}{m_{\text{metal}}} \quad (2)$$

where n_I (metal) and n_{Cs} (metal) are the amounts of iodine and cesium in the metal sample, respectively; n_{metal} is the amount of the metal sample; A_{128_I} (metal) and A_{128_I} (CsI) are the activities of ^{128}I at the end of the short irradiation in the metal and CsI samples, respectively; $A_{134_{Cs}}$ (metal) and $A_{134_{Cs}}$ (CsI) are the activities of ^{134}Cs at the end of the long irradiation in the metal and CsI samples, respectively; m_{metal} and m_{CsI} are the masses of the metal and CsI samples, respectively; M_{metal} and M_{CsI} are the molar mass of the metal and CsI, respectively.

Finally, the experimentally determined mole fractions x_I and x_{Cs} in LBE, Pb and Bi are shown in the logarithmic scale in Figure 2.

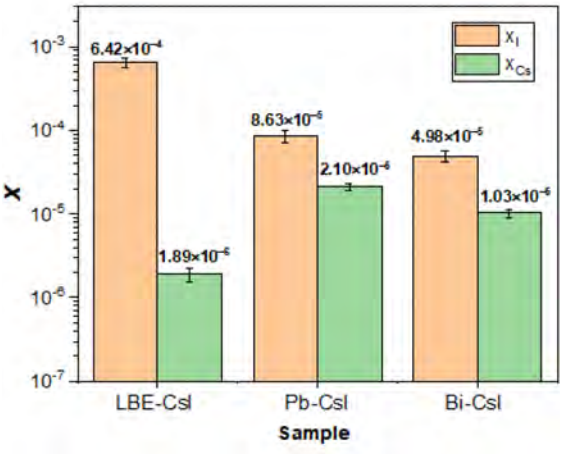

Figure 2: Mole fractions of Cs and I in LBE, Pb and Bi

In all these three metals, x_I is always clearly higher than x_{Cs}, while the exact values differ in different metals. In Pb and Bi, x_I is roughly 4 times x_{Cs}, while this ratio is about 34 in LBE. These results imply that the dissolution reaction cannot be simply expressed as $\text{CsI(s,l)} \rightarrow \text{Cs(metal)} + \text{I(metal)}$, but other reactions are also taking place. Considering that the initial materials were used without any pretreatment, the oxygen dissolved in the metals may play a role. A plausible explanation for the depletion of Cs in the metals may be the formation of $\text{Cs}_x\text{M}_y\text{O}_z$ (M = Pb or Bi) compounds, which remain on the surface. Indeed, information on this kind of Cs(Pb,Bi)-oxides exist in crystallographic databases, however their thermodynamic data is lacking. The only compound listed in the thermodynamic database implemented in HSC Chemistry [4] is CsBiO_2, however only for a very narrow temperature range. Equilibrium calculations based on these data indicate that the formation of this compound from mixtures containing CsI and oxygen-containing metals could indeed be possible. In order to confirm experimentally that oxygen played a role in the reactions described above, the same experiments will be repeated using metal pieces as precursors, which have been reduced beforehand by pure H_2 in the liquid state. They are supposed to contain only minuscule amounts of oxygen [5].

Conclusions

The solubility of cesium iodide in lead, bismuth and lead-bismuth eutectic was investigated by mixing CsI salt and the corresponding metal at 1000°C. The mole fractions of Cs and I were determined by neutron activation with the help of a referential CsI sample. The uneven ratios of x_I and x_{Cs} in metals indicate that the involved reaction cannot be simply described as dissolution of CsI in metal, but may also involve the formation of Cs(Pb,Bi)-oxides. More experiments with metal samples with lower oxygen concentrations will be performed to verify this assumption.

Acknowledgments

This work was funded by the PASCAL project under EURATOM HORIZON2020 Grant Agreement No. 945341.

References

[1] https://www.pascal-project.eu/
[2] A. Aerts, SCK·CEN, private communication.
[3] https://myrrha.be/
[4] https://www.hsc-chemistry.com/
[5] B. Gonzalez, SCK·CEN, private communication.

Preparation of LBE samples containing refractory metals for volatilization studies

I. Zivadinovic (ETHZ/PSI), J. Neuhausen (PSI), P. Steinegger (ETHZ/PSI)

Introduction

Continuing previous studies [1], the HORIZON2020 project PATRICIA aims, amongst other things, at further investigating the release behaviour of different safety-relevant radionuclides from the liquid lead-bismuth eutectic (LBE) employed as coolant in accelerator driven systems. Radioisotopes of refractory metals such as ruthenium, rhodium, rhenium and osmium fall into this category. Although the volatilization of these elements in their metallic state is expected to be completely negligible due to their low vapour pressure, their volatile oxides are believed to be of potential concern. Therefore, it is planned to study the formation of such volatile compounds of these elements in contact with LBE and possibly quantify the release of these compounds with the help of radiotracers. The challenge for such studies lies in the production of LBE samples containing suitable radioisotopes of the aforementioned elements. A prerequisite for performing experiments that allow for the extraction of thermodynamic information of the spallation and high-energy fission products in question is to ensure that the radiotracers form a homogeneous and dilute solution in liquid LBE. For this purpose, it is helpful to investigate the microstructure of such mixtures in order to try to grasp whether some kind of segregation phenomena affect the homogeneous distribution of the radioisotope(s) in question. The most straightforward approach for producing LBE samples containing refractory radioisotopes in dilute conditions is to mix elemental powders with molten LBE and subsequently irradiate the mixtures with neutrons. An alternative approach is the employment of a neutron activation of the refractory metals beforehand, followed by their addition to molten LBE in a second step.

Sample preparation

The phase constitution and microstructure evolution of LBE samples containing small quantities of refractory elements was studied. The nominal compositions of the respective samples contained 2-atom% of the respective refractory metal. The LBE base material used for all samples was supplied by the Belgian Nuclear Research Centre (SCK·CEN). Rh powder (99.9%, Fluka), Ru powder (99.95%, abcr), Re powder (99.9%, Fluka), and Os Powder (99.9%, Fluka) were used without pretreatment. Small chunks of LBE were filled into quartz tubes together with calculated amounts of the metal powders. The tubes were evacuated ($p < 10^{-4}$ mbar) and then sealed using an oxygen-hydrogen torch flame. Before use, the quartz tubes were cleaned by filling them with "piranha solution" (i.e., a 2:1 volume ratio mixture of 97% H_2SO_4 and >35% H_2O_2) overnight in order to minimize surface contaminations. The sealed and evacuated ampules were annealed at 1000°C for at least 18 h using a muffle furnace. During annealing, the liquefied samples were vigorously shaken multiple times to ensure a complete mixing of the chemicals. Afterwards, the samples were slowly cooled down to room temperature in ambient air.

Polishing

In order to properly investigate the microstructure, small vertical slabs of the as-cast samples were cut off with a cutting machine equipped with a diamond-cutting blade. The cut samples where embedded in a cold hardening epoxy resin and cured overnight. The surface of the cured specimen was subsequently ground using progressively finer grit (up to P4000) and polished using diamond paste with decreasing grain size (6 µm, 3µm, 1µm and 0,25µm). During the polishing procedure the sample surfaces were repeatedly etched using an etching solution (mixture of HNO_3, 65 %), acetic acid, H_2O_2, >35 % and deionized water in a 2:2:2:5 ratio) to reveal the microstructure, since the soft LBE matrix tends to smear easily during polishing.

Characterization

The polished surfaces were characterized by employing scanning electron microscopy (SEM) and energy-dispersive X-ray spectroscopy (EDX). An acceleration voltage of 20 KV was used for the resulting pictures as well as their corresponding EDX mappings. In addition, powder X-ray diffraction (XRD) measurements using Cu K-α radiation with a wavelength of 1.5406 Å as a source were performed for investigating the phase constitution of the samples.

Results and Discussion

For simplicity reasons we will focus in this report solely on the Ru-LBE samples. The results of the alloys containing the remaining above-mentioned refractory metals will be discussed in a separate report.

The microstructure of the Ru-sample can be observed quite clearly in the SEM picture (see Fig. 1). It is comprised of rod like primary crystals, which are

embedded in a soft metal matrix. With the corresponding EDX analysis and mapping the primary crystals could be identified as a pure Ru-phase. The soft metal matrix on the other hand shows a typical eutectic morphology and consists of LBE. The concentration of Ru in LBE is below the detection limit of the EDS detector (approx. 1 atom-%) and thus could not be measured.

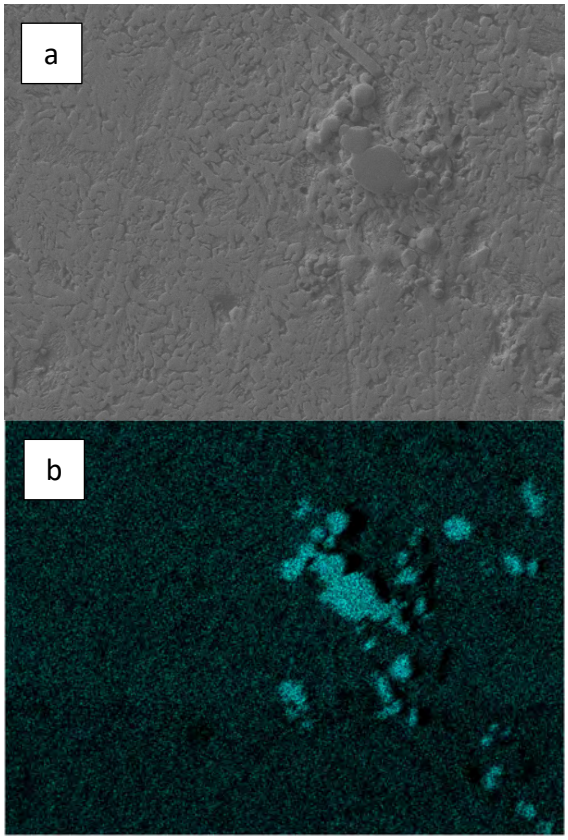

Figure 1: SEM picture of the polished Ru sample (a) and corresponding EDX mapping (b) with the concentration of Ru marked in cyan.

The powder XRD measurements did confirm the presence of Bi and ε-phase that comprise LBE. The above observed Ru-phase could not be detected. This most likely can be attributed to the low quantities of sample powder and short measurement times used in the measurement.

There could be two explanations for why large Ru crystals can be observed in our LBE samples. On the on hand the initial Ru powder could be simply suspended and immobilized within the melt upon solidification due to the vigorous shaking of the ampule and an incomplete dissolution of the initial Ru powder. Another possibility would be the complete dissolution of the added elemental Ru at high temperature and the subsequent re-precipitation from the melt as large primary crystals upon reaching its saturation concentration in LBE as the temperature decreases. Given the fact that both, the binary Pb-Bi [2] and the Bi-Ru-systems [3], form low melting eutectics, the latter assumption is more likely. Under these circumstances it is reasonable to assume that in the ternary Bi-Pb-Ru-system a ternary low-melting eutectic exists. This would ensure that at elevated temperatures a complete dissolution of all elements occurs. By further diluting the sample with pure LBE in order to achieve very dilute conditions, a homogeneous melt is guaranteed to form, which can be used to quantify the release of ruthenium from molten LBE in transpiration experiments [4].

Conclusion and Outlook

In the next step, the preparation of samples containing ^{97}Ru and ^{103}Ru as radiotracers (produced by neutron irradiation) will be attempted. Although the direct neutron activation of the prepared inactive alloys is possible, it comes with a few downsides, such as an increased background of co-produced radiotracers within LBE. Thus, the neutron irradiation of elemental Ru and the subsequent production of the alloys is preferred. More importantly, it allows us to reach higher total activities of the desired Ru radiotracers, which can still be safely handled in the radiochemical laboratory. The samples produced in this way will be employed in evaporation experiments in order to measure the volatilization of Ru from LBE.

Acknowledgements

This work was funded by the PATRICIA project under EURATOM HORIZON2020 Grant Agreement No. 945077.

References

[1] J. Neuhausen, *Chimia*, **74** (2020), pp. 976-983
[2] Martins, V.B., Nagasima, T.P., Eleno, L.T.F. et al. *J. Phase Equilib. Diffus.* **38** (2017), pp. 195–200
[3] Okamoto H.: *Bi-Ru (Bismuth-Ruthenium)*. Binary Alloy Phase Diagrams, Second Edition, Ed. T.B. Massalski, ASM International, Materials Park, Ohio 1 (1990), pp. 783-785
[4] H. Kvande, P. G. Wahlbeck, R. Portanova, R. Hesse, M. Sandström, *Acta Chemica Scandinavica*, **30a** (1976), pp. 297-302

Half-life measurement of ^{148}Gd via the "direct method"

N. M. Chiera (PSI), Z. Talip (PSI/CRS), R. Dressler (PSI), P. Sprung (PSI/AHL), D. Schumann (PSI)

Introduction

In the framework of the ERAWAST project [1, 2], the half-life ($t_{1/2}$) of ^{148}Gd was re-measured applying two different techniques, namely the *decay method* and the *direct method*. Preliminary results obtained with the *decay method* pointed to a half-life of 78.4 years, with a 13% uncertainty [3]. It is expected that further sequential sets of measurements will reduce the final error.

In this report, a preliminary result on the half-life of ^{148}Gd, obtained with the *direct method*, is presented.

Experimental

A scheme of the experimental steps for the measurement of the half-life of the α-emitter ^{148}Gd (E_α = 3.182 MeV [I_α = 100%]) is given in Figure 1.

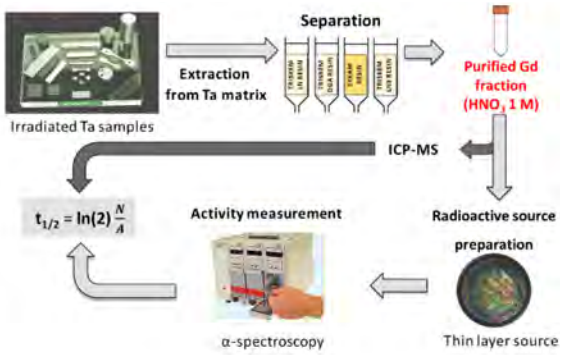

Figure 1: Gd radionuclides were extracted from irradiated Ta samples [4] and separated from other lanthanides and spallation products by applying a series of ion-exchange chromatography using LN, DGA, SYKAM, and LN3 resins, in this order. An aliquot of the retrieved Gd fraction was used to determine the number of atoms contained in the fraction itself. Successively, the very same Gd fraction was used to prepare a thin layer source by molecular plating. The α-activity of the so-prepared source was measured. Finally, the combination of the ICP-MS and the α-activity results allowed for an estimation of the half-life. Details for each procedure are given in the text.

Separation: A pure Gd fraction containing ^{148}Gd was retrieved from radioactive Ta samples applying the method described in [5]. During separation, the short-lived gamma-ray emitter ^{153}Gd ($t_{1/2}$ = 144.4 d, E_γ = 97.43 keV [29%]) was used for monitoring. The separated fraction, in 1 M HNO_3, was analyzed by mass-spectrometry without further purification.

Mass-spectrometry analysis: The absolute number of ^{148}Gd atoms in the retrieved fraction was determined by "reverse isotope dilution" [6] and "gravimetric standard addition with an additional internal standard" [7] – here Eu. All analyses were conducted on the Nu Instruments Plasma 3 MC-ICP-MS collecting simultaneously the signals at masses 142, 145, 147-157, 159, 160, and 163. Analytes were introduced in 0.28 M HNO_3 using an Elemental Scientific APEX HF nebulizing system. Online instrumental mass discrimination was corrected online using Eu [8]. Successively, offline reprocessing adjusted and improved this correction using the relative magnitude of Gd [9] and Eu mass discrimination defined using mixed solution standards analyzed alongside the samples at matching intensities.

Radioactive source preparation: A thin ^{148}Gd α-source was prepared with the molecular plating technique, using an aliquot (0.516547 g) of the Gd fraction. In order to estimate the number of atoms of ^{148}Gd deposited on the carbon foil, the plating yield was calculated. The latter was determined by measuring the activity of the ^{153}Gd γ-ray tracer contained in the Gd sample before deposition, and comparing it to the activity of the ^{153}Gd deposited on the carbon foil. Efficiency calibration was performed with a reference ^{133}Ba ($t_{1/2}$ = 10.54 y, E_γ = 80.99 keV [32.9%]) source certified by PTB, allowing for the quantification of the activity of the ^{153}Gd tracer in both geometries (i.e., in solution and in the thin layer).

The molecular plating cell used for the deposition of Gd on a carbon foil is described in [10]. The plating cell, the carbon foil (15 µm), and the Pt wire (anode) were rinsed with iPrOH. The copper block (cathode), was cleaned with citric acid 0.1 M, and successively rinsed with MilliQ-2 water and iPrOH, in this very same order. To maintain a constant temperature of 15°C during deposition, the cell was implemented with a Peltier cooler at the cathode. The plating solution was prepared as follows. The Gd aliquot was dried at 70°C under a N_2-flow, and then dissolved in 3 ml of 0.1 M HNO_3. The solution was again evaporated at 70°C under a N_2-flow, re-dissolved in 10 ml of isopropanol (iPrOH), and put in an ultrasonic bath for 5 minutes at normal temperature and pressure conditions. Successively, the solution was transferred to the plating cell. The deposition of Gd on the graphite foil was achieved in 4 hours, by applying a constant voltage of 100 V (starting current: 2.58 mA). The distance between the two electrodes was 10 mm.

Activity measurement: The activity of the ^{148}Gd plated on the graphite foil was quantified by α-spectrometry. The measurement was performed for 500 s. The efficiency of the α-spectrometer was derived by measuring the count rate of a certified

^{241}Am source with activity A = (535 ± 11) Bq at the time of the α-measurements.

Results and Discussion

Repeated mass spectrometry analyses at 1) high mass resolution, 2) medium mass resolution, and 3) low mass resolution settings yielded consistent results. Interferences from Nd, Sm, and Dy (stable Gd nuclides) were monitored and found to be insignificant assuming natural isotopic compositions. The obtained ^{148}Gd/$^{152,154-157}$Gd values of the pure Gd fraction, in conjunction with the content of stable $^{152,154-157}$Gd nuclides from reverse isotope dilution using ^{148}Gd as an isotope tracer and standard addition normalizing to both ^{151,153}Eu, yielded overlapping results for the number of ^{148}Gd atoms. The concentration of ^{148}Gd in the retrieved fraction was found to be 0.383 nmoles per gram of solution (solvent: 1 M HNO_3), with a combined uncertainty of 1.17% (1 SD), as determined from Monte Carlo uncertainty estimations.

γ-spectrometric measurements of the Gd solution before electrodeposition obtained a ^{153}Gd activity of (21.02 ± 0.23) Bq @03.03.2021. After molecular plating, the activity of the ^{153}Gd tracer deposited on the foil was determined to be (0.31 ± 0.01) Bq @29.09.2021. Considering the decay of the ^{153}Gd tracer between the activity measurement before deposition and the measurement after deposition (i.e., 210 days), a (2.71 ± 0.08)% plating yield was calculated. Therefore, the amount of ^{148}Gd plated on the carbon foil corresponds to (3.23 ± 0.10) × 10^{12} atoms. From the α-spectrum (see Fig. 2) of the ^{148}Gd deposited on the graphite foil, it was possible to calculate a ^{148}Gd activity of (954 ± 21) Bq.

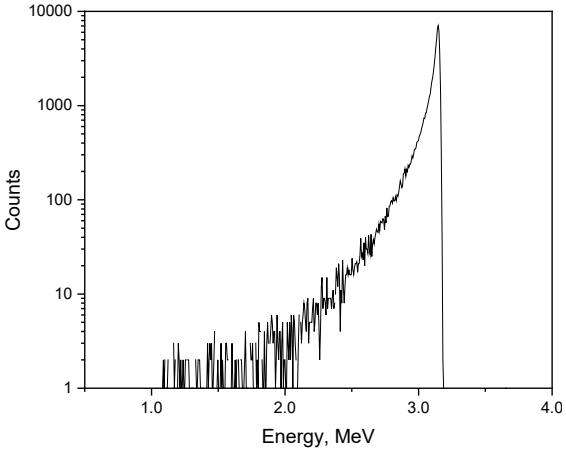

Figure 2: α-spectrum (measurement time: 500 s) of the electrodeposited ^{148}Gd on a graphite foil. No other α-emitters were detected.

The half-life of ^{148}Gd was obtained by applying Equation 1:

$$t_{1/2} = \frac{N \cdot \ln(2)}{A} \quad (1)$$

Where N is the number of ^{148}Gd atoms plated on the carbon foil, and A refers to their activity.

In this work, a preliminary half-life value of 74.3 y for ^{148}Gd was determined, with an estimated total uncertainty of 3.8%. This result is in perfect agreement with the $t_{1/2}$ = (74.6 ± 3.0) y value from [11], currently reported in the ENDF/B-VIII.0 database, and it is as well in agreement, within the error bars, with the preliminary half-life value obtained by the decay method (i.e., 78.4 ± 10.2) y reported in [3].

Acknowledgement

This project is funded by the Swiss National Science Foundation (SNF grant no 200021-159738).

References

[1] D. Schumann et al., *J. Phys. G: Nucl. Part. Phys.*, **35** (2007), pp. 014046-01052
[2] D. Schumann et al., *Radiochim. Acta*, **101** (2013), pp. 501-508
[3] N.M. Chiera et al., *LRC Annual report 2019* (2020), pp. 36-37
[4] Y. Dai et al., *J. Nucl. Mat.*, **343** (2005), pp. 33-44
[5] N.M. Chiera et al., *Plos One*, **15** (2020), pp. 0235711
[6] J. Vogl, W. Pritzkow, *Mapan – J. Metrol. Soc. India,* **25** (2010), pp. 135
[7] A. L. Hauswaldt et al., *Accred. Qual. Assur.,* **17** (2012), pp. 129-138
[8] T. L. Chang et al., *Int. J. Mass Spectrom. Ion Processes* **139** (1994), pp. 95-102
[9] J. He et al., *Anal. Chem.,* 92 (2020), pp. 6103-6110
[10] E.A. Maugeri et al., *J. Instrum.,* **12** (2017), pp. P02016-P02037
[11] R. J. Prestwood et al., *Phys. Rev. C*, **24** (1981), pp. 1346-1347

Removal of ^{137}Cs from radioactive aqueous samples by an innovative amyloid-carbon hybrid filter

N. M. Chiera, R. Eichler (PSI), S. Bolisetty (BluAct Technologies GmbH/ETHZ), R. Mezzenga (ETHZ), P. Steinegger (ETHZ/PSI)

Introduction

Among the different fission products in nuclear power reactors, caesium-137 (^{137}Cs) is of particular importance. In fact, with a half-life of roughly 30 years, this radionuclide represents the primary source of penetrating gamma (γ) radiation for decades after discharge of, spent nuclear fuel. Similarly to the other alkali metals, it is water-soluble and prone to bioaccumulation in marine and freshwater ecosystems due to its capability of substituting potassium in living organisms. Although many methods are currently available for decontamination of radioactive wastewater from nuclear fission products [1-4], most of the existing technologies show strong limitations, such as low efficiencies, high production and operational costs, or slow kinetics. Recently, an innovative natural filter membrane based on a blend of whey protein amyloids and activated carbon was developed [5]. This filter material demonstrated to be applicable to a large variety of contaminants, including viruses, under varied chemical conditions [6-8]. In this work, preliminary tests on the performance of the filter material were carried out by measuring the radioactivity of ^{137}Cs before and after filtration of a radioactive sample in aqueous phase. The obtained results were published in [9].

Experimental

Hybrid composite membranes having 10 wt.-% amyloid fibrils were prepared by initial mixing of a β-lactoglobulin solution, activated carbon and paper pulp in the ratio of 10:40:50 wt.-% respectively. Water was removed from this mixture by vacuum filtration followed by a pressing and drying process similar to paper manufacturing. The obtained membranes (3 mm in thickness) were used without further purification to filter the radioactive water samples containing ^{137}Cs. Experiments were conducted with the syringe-aided setup shown in Fig. 1a. The hybrid membrane filter was cropped to a disk with a diameter of 50 mm (2.8 g in weight), and placed inside the filter holder (see Fig. 1b and 1c). γ-ray spectrometry using an HPGe detector in conjunction with the Genie2k® data acquisition software from Mirion Technologies, Inc. was utilized to monitor and quantify the amount of ^{137}Cs in each sample. Radioactive test solutions were prepared by diluting 100 µL of a ^{137}Cs stock solution to 50 mL with ultrapure MilliQ water. Each test solution was acidified to a pH = 4 using 1 M HCl in order to mimic a corrosive environment. The resulting average ^{137}Cs activity per unit volume amounted to $2.5 \cdot 10^5$ Bq·L^{-1}. This is comparable to the highest measured concentration of ^{137}Cs in the seawater just off the coast of the Fukushima Daichii Nuclear Power Plant one month after the accident [10]. After a pre-treatment of the filter with 5 mL MilliQ water at pH = 4, aliquots of 5 mL of the above-mentioned radioactive sample solution were passed through the filtration cell by applying gentle pressure with the syringe at a flux of approx. 1 mL·min^{-1}. In a second step, the retention capacity of the membrane was investigated by performing consecutive filtrations of carrier-added CsCl solutions (10 ppm) spiked with ^{137}Cs for monitoring purposes.

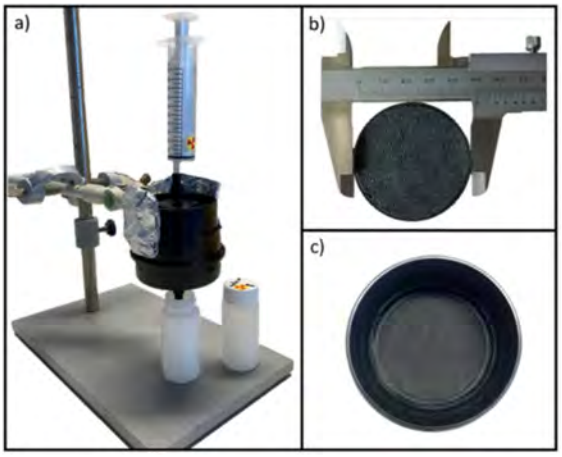

Figure1: a) Syringe-aided filtration setup for the removal of ^{137}Cs from aqueous samples; b) top view of filter disk (50 mm diameter); c) top-down view of the filter holder containing the amyloid-carbon hybrid filter. Figure taken from [9].

Results and Discussion

The γ-spectrometric measurements demonstrated that after a single filtration cycle the ^{137}Cs-content in 20 mL of radioactively contaminated water is reduced by a factor of approximately 340 to about 700 Bq·L^{-1}, corresponding to a decontamination efficiency of 99.7% (see Fig. 2a). According to the International Commission on Radiological Protection, the guidance level value of ^{137}Cs in drinking water amounts to 10 Bq·L^{-1} [11]. Hence, two consecutive filtering cycles are sufficient to render an initial sample of radioactively contaminated water suitable for human consumption. To clarify the role played by the amyloid fibrils in the adsorption process, reten-

tion experiments were performed with the same typology and mesh-size of filter support deprived of the amyloid-carbon hybrid admixture. As shown in Fig. 2b, the retention of ^{137}Cs with the amyloid-carbon hybrid filter is about 100 times more efficient, clearly indicating that the protein aggregates are the main contributors to the chemical binding and retention of Cs. Test experiments with macroscopic amounts of ^{nat}CsCl solution (10 ppm) spiked with ^{137}Cs showed that, after six consecutive filtration cycles of 5 mL each, 102 µg of Cs were retained, without still reaching saturation. This indicates a specific sorption capacity of at least 36 µg of Cs per gram of filter material, at the applied conditions. Based on these results, it is expected that radioactivity levels up to 0.2 TBq per kilogram of filter material can be extracted from radioactively contaminated water in a single filtration step.

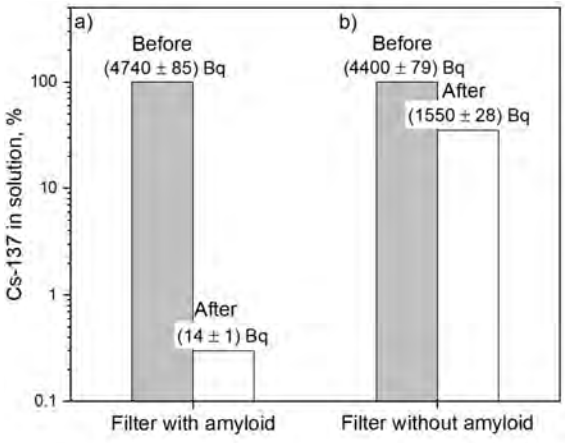

Figure 2: Activity of ^{137}Cs in [Bq] before and after the filtration of a radioactive aqueous sample (volume = 20 mL) through a) an amyloid-activated carbon hybrid membrane, b) a quartz fiber membrane. Uncertainties refer to counting statistics only.

For comparison, the Cs sorption capacities of various materials at pH = 4 and at room temperature are listed in Table 1. Different experimental settings (e.g., flux, pH of the filtered water, and the percentage of amyloids contained in the filter material) might further increase the observed sorption capacity. The effective removal of ^{137}Cs can be considered as a benchmark for the successful application of the above-mentioned filtering material in the cleaning of low- to medium-level radioactive aqueous waste containing fission products. Additional investigations on the stability of the amyloids against radiation damage (i.e., degeneration of the protein-based binding sites) are envisaged. This will help to understand whether this filter material can be efficiently applied in the treatment of high-level radioactive liquid waste as well. Finally, it is important to mention that, since the membranes are completely made of natural components, their controlled combustion to ashes further minimizes the final volume of radioactive waste.

TABLE 1: Caesium sorption capacities of diverse filter materials at pH = 4 and T = 25 °C. (a)Potassium nickel hexacyanoferrate loaded-silica gels and chabazite; (b) PAN = polyacrylonitrile; (c) Hydrous manganese oxide; (d) Hydrous stannic oxide.

ADSORBENT	CAPACITY (mg/g)	CONTACT TIME
KNiFC (a)	0.123	7 days
CLINOPTILOLITES	1.31	48 hours
MnO_2-PAN (b)	0.942	35 min
BENTONITE	0.54	7 hours
HMO (c)	0.11	25 min
HSO (d)	0.12	20 min
AMYLOIDS (this work)	0.62	6 min

References

[1] X. Zhang et al., *Chemosphere*, **215** (2019), pp. 543–553

[2] D. Rana et al., *Desalination*, **321** (2013), pp. 77–92

[3] M. Jiménez-Reyes et al., *J. Environ. Radioact.*, **233**, (2021), pp. 106610–106622

[4] X. Zhang and Y. Liu, *Environ. Sci.: Nano*, **7** (2020), pp. 1008–1040

[5] S. Bolisetty and R. Mezzenga, *Nat. Nanotechnol.*, **11** (2016), pp. 365–371

[6] S. Bolisetty et al., *Chem. Comm.*, **53** (2017), pp. 5714–5717

[7] M. Peydayesh et al., *Langmuir*, **35** (2019), pp. 4161–4170

[8] S. Bolisetty et al., *Environ. Sci.: Water Res. Technol.*, **6** (2020), pp. 3249–3254

[9] N. M. Chiera et al. *RSC Advances,* **11** (2021), pp.32454-32458

[10] H. Kaeriyama, *Fisheries Oceanography*, **26** (2017), pp. 99–103

[11] A. Wrixon et al., *J. Radiol. Prot.*, **28** (2008), pp. 161–168

Separation and recovery of Se from PbSe

N. M. Chiera, A. Vögele, D. Schumann (PSI), M. Veicht (EPFL/PSI)

Introduction

In a previous work [1], a technique for preparing enriched $^{208}Pb^{78}Se$ and $^{208}Pb^{79}Se$ targets for neutron capture studies was presented. Here, a method for extracting Se from (used) PbSe targets is discussed. The separation process can also be applied to the purification of elemental Se.

Experimental

The chemical separation of Se from PbSe was followed by using radioactive $Pb^{75}Se$ as tracer. $Pb^{75}Se$ was produced by irradiation for 3600 seconds of a PbSe sample (total mass: 0.04 g) with thermal neutrons at the spallation neutron source SINQ, PSI. Before separation, the count rate of the main γ-ray lines of ^{75}Se ($t_{1/2}$ = 119.6 d, E_γ = 136 keV [59.2%]) was recorded. γ-spectrometric measurements were performed with a Broad Energy Germanium (BEGe) detector (Mirion Technologies Inc.). The energy calibration of the spectrometer was done with a certified ^{152}Eu standard γ-ray source from PTB. All γ-ray spectra were recorded and analyzed with the Genie™ 2000 Gamma Analysis software (Mirion Technologies Inc.). The separation and extraction of selenium proceeded in two steps, as depicted in Figure 1.

STEP A: Dissolution of PbSe. A mixed sample of PbSe and $Pb^{75}Se$ tracer (total mass: 0.05 g) was placed inside a 3-neck round-bottom glass flask immerged in a water bath kept at 80°C. The material was dissolved in modified aqua regia, i.e., by adding in this very same order conc. HCl (37%, Sigma-Aldrich), conc. HNO_3 (EMPLURA®, Merck), and H_2O_2 (35%, Sigma-Aldrich) in a 4:1:1 ratio, under N_2 flow (50 mL/min). Circa 12 mL of modified aqua regia were necessary to completely dissolve the PbSe sample in 1 hour. Undesired H_2Se that might have been produced during dissolution was trapped in a glass bubbler filled with a saturated Na_2SO_3 (100% iodometric, Sigma-Aldrich) solution.

STEP B: Extraction of Se. The dissolved PbSe was transferred to a glass beaker, and the solution was heated to 40°C while stirred with a magnetic hotplate stirrer. Successively, solid Na_2SO_3 *quantum suffit* was carefully added with the immediate formation of an insoluble red precipitate. The addition of solid Na_2SO_3 continued until no reaction was further observed. Then, the beaker was removed from the heating plate, and cooled down to room temperature. Afterwards, the content of the beaker, including the red precipitate, was transferred into a separatory funnel. 5 ml of MilliQ-2 water were used to rinse the beaker, and added to the separatory funnel. Extraction of the red precipitate was performed with a volume of CS_2 (ACS ≥ 99.9%, Sigma-Aldrich) equivalent to the aqueous phase (i.e., 17 ml circa). The collected CS_2 was evaporated at room temperature inside a variable air volume fume hood, and the red evaporation residue was stored. The aqueous phase left in the separatory funnel was transferred back to the glass beaker, heated to 40°C while stirred with a magnetic hotplate stirrer. Successive steps of additions of solid Na_2SO_3 and extractions with CS_2 were repeated until ^{75}Se in the aqueous phase was no longer detected. After five consecutive steps of the above-mentioned process, the γ-ray spectrum of the retrieved ^{75}Se was recorded, allowing for its quantification.

Figure 1: Scheme of the two-step process for the separation and extraction of Se from PbSe. Further details are given in the text.

The purity of the separated Se was checked by ICP-OES. For these measurements, an aliquot of 50 mg of separated Se was digested in 5 ml of aqua regia (4 ml HCl + 1 ml HNO_3). Successively, two samples for analysis, namely Se-I and Se-II, were prepared by diluting 0.01 ml of the digested Se sample with 2% HNO_3 (prepared from conc. HNO_3, TraceSELECT™, Honeywell Fluka™) to a final volume of 13.996 ml (dilution factor: 1400.5; acidity: ~0.32 M). The ICP-

OES measurements were performed with a sequential ICP spectrometer (Agilent 5110, Agilent Technologies, Inc. U.S.A.), equipped with an Agilent SPS 4 Autosampler. External calibration with Pb (1000(3) mg/l) and Se (1000(2) mg/l) standards (TraceCERT®, 2% w/w HNO_3, Sigma-Aldrich) was performed at 10, 1, 0.1, 0.01, and 0.001 ppm.

Results and discussion

The only radioactive products obtained by irradiation of ^{nat}Pb with thermal neutrons at our experimental conditions are the quasi-stable ^{205}Pb ($t_{1/2}$ = 1.5 × 10^7 y) and the short-lived ^{209}Pb ($t_{1/2}$ = 3.253 h), as a consequence of the neutron capture by the stable ^{204}Pb and ^{208}Pb isotopes, respectively. The calculated activities immediately after irradiation were (4.9 × 10^{-5}) Bq of ^{205}Pb and 19 kBq of ^{209}Pb. However, after a cooling time of 24 hours, only ^{205}Pb was present, due to its longer half-life. Since the β^- decay of ^{205}Pb is not accompanied by γ-ray emissions, the peaks in the γ-spectra therefore correspond only to the radiations emitted by ^{75}Se. Integration of the main ^{75}Se gamma line at 136.0 keV gave a count rate of (24 ± 0.3) cps before separation and (17 ± 0.5) cps after the removal of Pb, indicating thus an efficiency of the Se retrieval process of (70 ± 3)%. Due to the absence of γ-lines associated with radioactive Pb, γ-spectroscopy allowed only for a quantitative estimation of the Se obtained after separation, without providing any information on the purity of the retrieved Se. Therefore, ICP-OES analysis was performed. The results, given in Table 1, indicate a purity of the separated Se of ≈99%.

In the following, a reaction mechanism for the separation of Se from PbSe is proposed. It is known that aqua regia dissolves several sulphide salts like galena (PbS), with release of H_2S [2]. Being PbSe a chalcogenide as PbS, the same effect is thus expected on selenide salts. However, for the purpose of this separation, losses of Se by formation of the volatile H_2Se had to be prevented. This was achieved by oxidation of the selenide ion Se^{2-} by addition of H_2O_2 during the dissolution process, leading to the formation of selenous acid:

$$Se^{2-} + 3H_2O_2 \rightarrow SeO_3^{2-} + 3H_2O \quad (1)$$

$$SeO_3^{2-} + H^+ \rightarrow HSeO_3^- \quad (2)$$

$$HSeO_3^- + H^+ \leftrightarrow H_2SeO_3 \quad (3)$$

Even though the formation of volatile Se(IV) chlorinated species cannot be excluded, their rapid decomposition in water-based solutions occurs:

$$SeCl_4 + H_2O \rightarrow SeOCl_2 + 2HCl \quad (4)$$

$$SeOCl_2 + 2H_2O \rightarrow H_2SeO_3 + 2HCl \quad (5)$$

Successively, the addition of sodium sulfite promoted the reduction of the selenous acid to elemental Se, with concomitant oxidation of the sulfite(IV) ion to the sulfate(VI) one:

$$H_2SeO_3 + 2Na_2SO_3 \rightarrow Se\downarrow + 2Na_2SO_4 + H_2O \quad (6)$$

Following Ostwald's rule of stages, the precipitated Se is in the form of its least stable allotrope, i.e., red amorphous selenium (red α-Se). Since during precipitation the solution was kept at 40°C, the change of phase from red α-Se to black amorphous selenium or trigonal selenium was prevented. This is crucial for the extraction step, since among all the Se allotropes, only red α-Se is soluble in CS_2. The high purity of the retrieved Se is explained by the fact that most of the contaminants (e.g., Co, Zn, Pb, etc.) are not soluble in CS_2, whereas red α-Se is readily dissolved in this organic solvent.

TABLE 1: Concentration (in ppm) of Pb and Se in the separated selenium fraction deduced by ICP-OES analysis. For each element, the measurements were performed at two wavelengths, as indicated. The standard deviation (SD, in ppm) of the calculated concentrations is given as well.

	WAVELENGTH (nm)	CONC. (ppm)	SD (ppm)
Se-I	Pb (220.353)	0.003	0.001
	Pb (283.305)	0.005	0.001
	Se (196.026)	3.789	0.040
	Se (203.985)	3.818	0.042
Se-II	Pb (220.353)	0.003	0.001
	Pb (283.305)	0.004	0.001
	Se (196.026)	4.582	0.271
	Se (203.985)	4.606	0.271

References

[1] I. Danilov et al., *LRC Annual Report 2019* (2020), pp. 42-43

[2] T. T. Chao et al., *J. Research U.S. Geol. Survey.,* **5** (1977), pp. 409-412

Preparation and Characterization of Holmium Sources *via* Drop-On-Demand for Measuring the Electron Neutrino Mass

N. Cerboni (ETHZ/PSI), E. Müller Gubler (PSI/LNB), D. Ferri (PSI/LBK), E. A. Maugeri (PSI)

Introduction

The radioactive isotope ^{163}Ho decays by electron capture (EC) with a proposed *Q*-value between 2.5 and 2.8 keV [1]. This low transition energy makes ^{163}Ho an interesting candidate for the direct measurement of the electron neutrino mass with a calorimetric method. The HOLMES experiment is an international project aiming to perform this measurement with a sub-eV sensitivity by implanting about 300 kBq of ^{163}Ho nuclei, equally distributed into an array of 1024 calorimetric pixels. The source of Ho consists of an Au plated Cu ring covered with the requested activity of ^{163}Ho and acts as a cathode in an ionization chamber. The release and ionization of holmium is carried out via Ar sputtering [2]. The method for the production of the ^{163}Ho source has to fulfill three main pre-requisites:

1. Uniform surface distribution to guarantee a homogeneous release of the ^{163}Ho during the sputtering.
2. Chemical homogeneity, to avoid chemical shift of the end-point.
3. High yields, due to the elevated costs associated with the production of ^{163}Ho.

So far, sources, which have been produced by thermal reduction [3] and molecular plating [4], do not satisfy all three criteria. In this work, the drop-on-demand inkjet printing is considered as a promising alternative deposition technique. Herein, we present a detailed chemical and morphological characterization of the droplets produced by this method.

Experimental

The drop-on-demand inkjet printing consists in depositing one drop (5 µL) of an aqueous solution of a Ho salt (ca. 6 mM) deposited onto a solid substrate, which corresponds to the outer layer of the final source (Au). Subsequently, the droplet was dried in the air at room temperature. The used set up is divided into two components: a dosage device (DOSTAL DOSY) and a 3D positioning system (High-Z 100T), which is controlled remotely by WinPC-NC v.2.50/04 software. The homogeneity of both the Ho surface distribution and the Ho chemical speciation of three different salts, namely $Ho(NO_3)_3$ $5H_2O$, $HoCl_3$ $6H_2O$ and $Ho(OAc)_3$ xH_2O, were investigated. $Ho(NO_3)_3$ was chosen because it is the result of the ^{163}Ho purification process, while $HoCl_3$ and $Ho(OAc)_3$ show a stronger and weaker formation enthalpy, respectively. The latter could facilitate the formation of metallic Ho during the sputtering.

The deposited droplets were characterized by means of a scanning electron microscopy (SEM; Zeiss Nvision-40) coupled with energy dispersion spectroscopy (EDX; Oxford Instruments X-Max^N 50 detector) and attenuated total reflection infrared spectroscopy (ATR-IR; Platinum ATR). In addition, time-resolved ATR-IR was used to follow the drying process. For this purpose, a drop was placed on the diamond crystal and spectra were measured every minute until the sample was dry.

A final source was prepared by depositing 190 droplets with approximately 3 µL each of $Ho(OAc)_3$ onto a 100 nm Au layer deposited on a Cu block. This sample was sent to the National Institute of Nuclear Physics in Genova for a qualitative study.

Results and Discussion

Surface Distribution

The morphology of the dried drops was investigated with SEM. The SEM images of both the $Ho(NO_3)_3$ and $HoCl_3$ are depicted in Fig. 1(a) and (b), respectively. They show a compact deposit with a smaller diameter than the wet drop by approximately one order of magnitude, while $Ho(OAc)_3$ dries with a different mechanism, known as “coffee-ring effect”, resulting in the ring-shaped deposit displayed in Fig. 1(c).

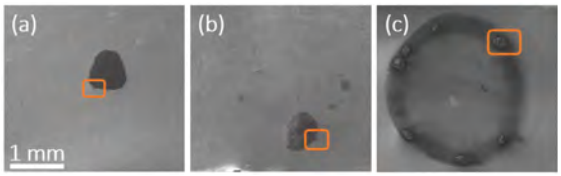

Figure 1: (a), (b) and (c) SEM images of $Ho(NO_3)_3$, $HoCl_3$ and $Ho(OAc)_3$. The orange squares indicate the selected areas where EDX spectra were taken (see Fig. 2).

In our case, the latter drying mechanism is more favorable, as it leads to a lower Ho surface concentration, which would result in a slower and more constant stream of sputtered material in the HOLMES experiment. It is worth noting that the Au surface of the backing is still visible in the middle of the $Ho(OAc)_3$ droplet. This can be avoided by using a substrate with a more hydrophilic surface than Au, which results in a better spreading of the droplet on the surface. The chemical composition of the dried droplets was determined by measuring EDX spectra,

as shown in Figure 2. In all the three samples, characteristic signals for Au (2.13 and 2.41 keV), Ho (1.05, 1.37 and 1.66 keV), O (0.525 keV) and C (0.27 keV) were observed. Additional peaks at 0.39 keV, 0.175, 2.63 and 2.815 keV confirm the presence of N and Cl for the $Ho(NO_3)_3$ and $HoCl_3$, respectively.

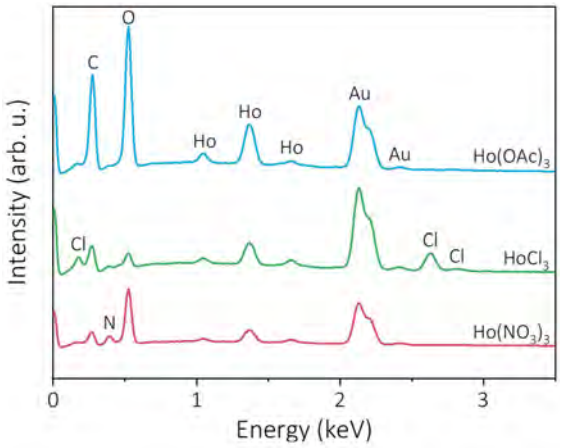

Particular attention must be drawn to the C signal present in both $Ho(NO_3)_3$ and $HoCl_3$ samples, which may be originated from C impurities on the Au surface. Overall, these results indicate that the elemental composition of the dried substances do not change upon drying. However, a more precise chemical analysis is needed to confirm the chemical speciation.

Chemical Homogeneity

The drying mechanism of $Ho(NO_3)_3$ was monitored *in-situ* by time-resolved IR spectroscopy (see Fig. 3).

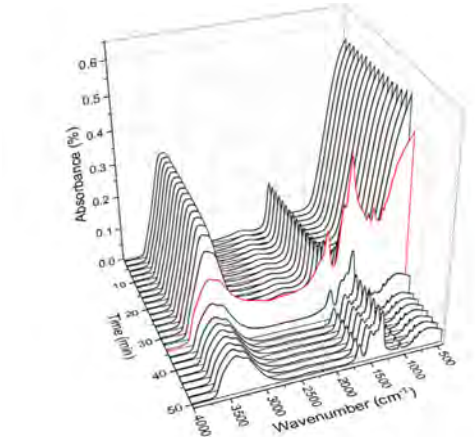

Figure 3: Time-dependent ATR-IR spectra of an aqueous solution of $Ho(NO_3)_3$. The red spectrum indicates the wet-to-dry transition.

The IR spectrum of the droplet is dominated by the vibrational modes of H_2O at ca. 3300 and 1630 cm^{-1} together with the loss of absorbance below 900cm^{-1}. As time increases, the intensity of the peaks slowly decreases, indicating the evaporation of H_2O. A drastic change in the spectrum is observed after ca. 35 min when H_2O is completely evaporated. The broad peak at ca. 3304 cm^{-1} converts into two signals at 3392 and 3255 cm^{-1}, indicating the transition from free to coordinated H_2O. In addition, new peaks arise in the fingerprint region, which correlate to the vibrational modes of the ligand, in this case the NO_3 group. Similar behavior was observed for the $HoCl_3$ and $Ho(OAc)_3$ samples.

Figure 4 compares the ATR-IR spectra of the dried droplets of the three Ho salts and of the corresponding reference materials. The main difference between the dried droplets and the references can be found in the relative peak intensity, which is probably caused by the change in coordination geometry of the Ho compounds as thin films, obtained after drying, versus the powders. Nevertheless, the identified vibrational modes of both the reference and deposited material correspond to those of the corresponding ligands (L) [5]. It is worth noting that the Ho-L bonds are only visible in the far IR range and hence not visible in Figure 4. Further investigations of the deposited material is currently evaluated by means of XRD and XPS.

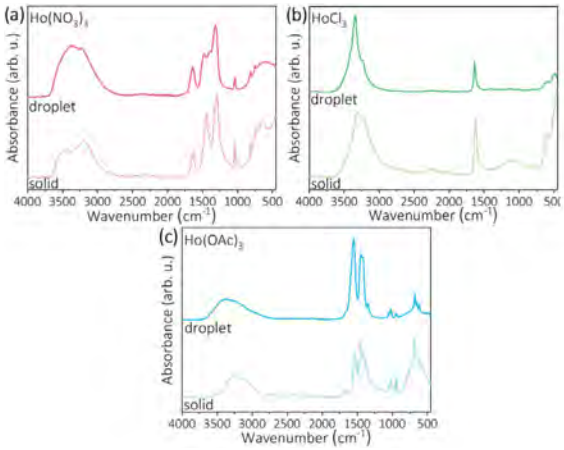

Figure 4: ATR-IR spectra of the reference solids and the dried droplets of (a) $Ho(NO_3)_3$, (b) $HoCl_3$ and (c) $Ho(OAc)_3$.

Yield

An accurate determination of the yield was obtained by measuring the γ spectra of both wet and dried droplets containing ^{166m}Ho as tracer. The studies indicate a deposition yield of about 100 %.

Source

A Ho source (100 nm of Au on Cu) was prepared by depositing 190 droplets of an aqueous solution of $Ho(OAc)_3$ (ca. 3 µL each). The source was tested at the ion implantation set up located in Genova. Preliminary results on this target show a significant signal intensity at the 165 m/z.

References

[1] R. G. H. Robertson, *Phys. Rev. C*, **91** (2015) pp. 035504
[2] B. Alpert et al., *Eur. Phys. J. C.*, **75** (2015) pp. 1-11
[3] M. De Gerone et al., *Nucl. Instr. Meth. Phys. Res. A*, **936** (2019), pp. 220-221
[4] G. De Bodin de Galembert, Master Thesis (2021)
[5] https://spectrabase.com/

Preparation of a thin ^{10}Be target for nuclear structure experiments

L. Tetley (Univ. York), E. A. Maugeri (PSI), M. Petri (Univ. York), D. Schumann (PSI)

Introduction

The emergence of the complexity of nuclear structure from the fundamental interactions between protons and neutrons, is one of the central questions of modern nuclear science. Recently, the development of chiral effective field theory (EFT) has enabled the derivation of two-nucleon (NN), three-nucleon (3N) and higher-body forces in a consistent, systematically improvable framework [1,2]. To support the developments of these calculations, cutting edge nuclear physics experiments measure key observables, that are sensitive to the subtle differences in the nuclear forces, in order to feedback to the calculations and benchmark the theoretical frontier.

Neutron-rich oxygen isotopes have proven to be ideal laboratories for the benchmarking of the chiral interactions. For the first time, valence space calculations with NN+3N forces were able to correctly place the oxygen dripline at ^{24}O [3]. More recently, large-space ab initio calculations, where all nucleons are treated as explicit degrees of freedom, have confirmed those early results [4-6]. A crucial next step is to examine the role of 3N forces in other observables. Indeed, previous work on ^{21}O has demonstrated the sensitivity of 3N forces to spectroscopic observables, such as level lifetimes [7]. In this experiment, we attempt an ambitious first measurement of lifetimes of excited states in ^{22}O, populated via the ^{10}Be(^{14}C,2p)^{22}O fusion evaporation reaction, employing a radioactive ^{10}Be target [8].

Target preparation

The requirement of a thin, homogeneous ^{10}Be target for the reaction necessitated the development of a novel ^{10}Be target. The development and production of the target took place at PSI, where the ^{10}Be is chemically extracted and purified from decommissioned proton irradiated polycrystalline graphite targets, from the Swiss Muon Source (SμS) [9]. The isotopic composition of the beryllium extracted in this way is ^{9}Be/^{10}Be = 2.110 ± 0.063 [10].

The targets were prepared by the molecular plating technique, depositing 192 μg of beryllium in form of $Be(OH)_2$ solution, onto a 7 mm diameter area of thin (1-2μm) platinum foils (see Fig. 1). A mixture of isopropanol (90 vol.-%) and isobutanol (10 vol.-%) was used as the solvent, with a constant 200 V applied, resulting in a current ranging from 0.45 mA to 0.13 mA. The yield of the deposition was estimated to be 30-40% via an activity measurement, reducing the estimated areal density of the ^{10}Be in the target to < 30 μg/cm^2.

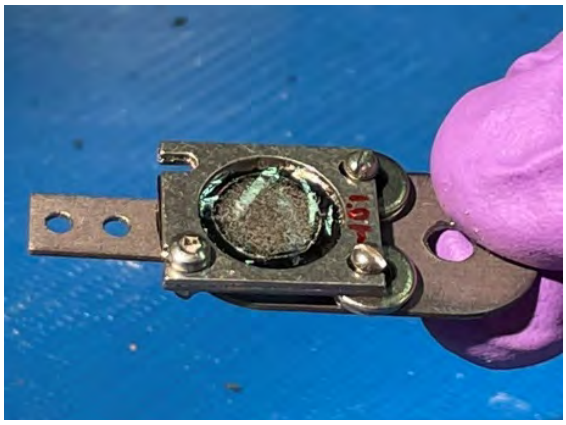

Figure 1: ^{10}Be target on a 1μm platinum foil that was used in the experiment.

Experiment

The experiment took place in April/May 2021 at Argonne National Laboratory (ANL). A ^{14}C beam with energies ranging between 50 MeV to 80 MeV was directed at the newly synthesised ^{10}Be target. The γ-rays emitted by the decaying nuclear states were detected by the state-of-the-art tracking γ-ray detector array GRETINA, which was coupled to the Fragment Mass Analyzer (FMA) to tag onto the outgoing ^{22}O fragments. The lifetime of the state of interest (3199 keV) was to be measured via the Doppler Shift Attenuation Method (DSAM), by analysing the Doppler-Induced lifetime-sensitive line shape of the peak on the γ-ray spectrum.

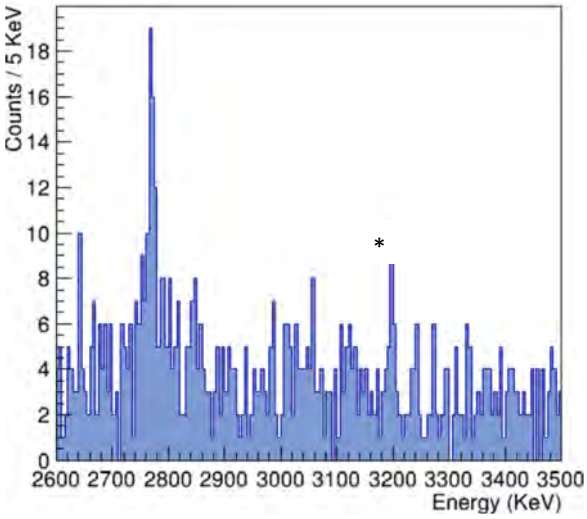

Figure 2: γ-ray spectrum of fusion evaporation residues with a mass over charge A/Q = 22/7, highlighting the potential 3199 keV peak.

Preliminary analysis of the data suggests that the cross-section of the 2-proton exit channel of the fu-

sion evaporation reaction was lower than first anticipated, which combined with the low deposition yield of the ^{10}Be has resulted in very few detected 3199 keV γ-rays originating from ^{22}O (see Fig. 2). Analysis is ongoing.

Conclusion

The development of a ^{10}Be target enables a greater experimental accessibility to the neutron rich region of the nuclear chart. The preliminary analysis of the data indicates that the deposition of the ^{10}Be onto the platinum foil was successful, albeit with a low yield. A potential 3199 keV transition from ^{22}O was observed in the γ-ray spectrum, in addition to γ-rays originating from other channels exclusive to reactions on ^{10}Be. By altering the solvents used in the deposition, future developments of the target will have an improved yield, enabling thicker and more active targets.

References

[1] E. Epelbaum et al., *Rev. Mod. Phys.*, **81** (2009), pp. 1773

[2] R. Machleidt et al., *LRC Annual Report 2017* (2018), pp. 12-13

[3] T. Otsuka et al., *Phys. Rev. Lett.*, **105** (2010), pp. 032501

[4] H. Hergert et al., *Phys. Rev. Lett.*, **110** (2013), pp 242501

[5] A. Cipollone et al., *Phys. Rev. Lett.*, **111** (2013), pp. 062501

[6] K. Hebeler et al., *Ann. Rev. Nucl. Part. Sci.*, **65** (2015), pp. 457-484

[7] S. Heil, et al., *Phys. Lett. B*, **809** (2020), pp. 135678

[8] M. Petri, experiment #1732, Argonne National Laboratory (2020)

[9] S. Heinitz et al., *Appl. Radiat. Isot.*, **130** (2017), pp. 260-263

[10] D. Schumann et al., *Radiochim. Acta*, **101** (2013), pp. 501-508

MSU – PSI: a new collaboration for implementing three important nuclear science experiments, based on the development of a ^{10}Be beam

A. Villari (FRIB/MSU), D. Schumann, E. A. Maugeri (PSI)

Introduction

The completion of the Facility for Rare Isotope Beams (FRIB) project involves a transition from operating NSLC's Coupled Cyclotron Facility to the use of FRIB's high-power superconducting linac and new rare isotope production facility. During this transition period FRIB's reaccelerator facility ReA is being used in stand-alone mode for science experiments with stable and long-lived isotopes. For this purpose, a Batch Mode Ion Source (BMIS) was developed in collaboration with ISOLDE-CERN (see Fig. 1). BMIS uses ISOLDE target modules with the material for the desired beam loaded into the target container.

As part of a collaborative effort, three ^{10}Be samples with up to 10 ng were produced by the Paul-Scherrer Institute, delivered to MSU, and used in BMIS to provide beam for three important nuclear science experiments.

Experimental

In the first experiment a ^{10}Be beam with an energy of 9.6 MeV/u was used to study different channels of the ^{10}Be+d reaction with the new solenoidal spectrometer SOLARIS in combination with an active target time projection chamber (AT-TPC). The second ^{10}Be experiment at 0.6 MeV/u aimed at understanding the beta-delayed proton emission in ^{11}Be, a very rare decay process. The latest experiment again used the SOLARIS spectrometer with a silicon detector array. This experiment with a ^{10}Be beam at 9.6 MeV/u aimed at gaining new insight into the ^{12}Be(t,p) reaction in background free conditions. ^{10}Be beam rates provided to the experiments ranged from 10^4 to 10^6 pps.

The availability of ^{10}Be samples from PSI was highly rewarding, not only for the successful outcome of all ^{10}Be experiments, but also for technical improvements achieved during the course of operating.

^{10}Be was extracted from a carbon target used for the production of muon at the Swiss Muon Source of the Paul Scherrer Institute, as described in [1]. In particular, an aliquot of a purified ^{10}Be batch was dissolved in HNO_3, 0.1 M, obtaining a solution with a concentration of 100 ng/mL. Three different tantalum cylinders were filled with 0.1 mL of the obtained solution, respectively. The solutions were let dry at room temperature under a flux of Ar, to avoid deposition of contaminant into the material.

The cylinders were then encapsulated in larger containers and shipped to the Facility for Rare Isotope Beams of the Michigan State University.

All the lab tools used were made in plastic or ceramic to prevent contamination of metals, especially titanium. In fact, the beam is made using NF_3 to convert ^{10}Be into $^{10}BeF_2$, which has the same mass of natural titanium, i.e., 48.

Figure 1: The BMIS system makes use of ISOLDE target modules coupled to front-end. Be-10 samples provided by PSI were loaded into the target container of the target modules to provide beams for reacceleration and use in nuclear science experiments.

Results

The three experiments were successfully concluded. The obtained promising results are currently under evaluation and will be soon available for publications emphasizing the success of this collaboration.

References

[1] S. Heinitz et al., *Appl. Radiat. Isot.*, **130** (2017), pp. 260-263

First tests of the UoM Frisch-grid ionization chamber at the National Physical laboratory

G. Lorusso (NPL), S. Bennett (UoM), A. Bennett, M. Bunce (NPL), E. A. Maugeri (PSI), A. Mcfarlane, A. Smith, G. Smith (UoM), D. Thomas (NPL), T. Wright (UoM)

Introduction

The goal of this project is twofold. Firstly, we wanted to test the performance of a double Frisch-grid ionization chamber newly developed by the University of Manchester (UoM) at fast neutron energies using ^{238}U(n,f) reference cross section. The second aim is to measure the ^{236}U(n,f) cross section to address discrepancies existing between previous measurements. This project is the initial step of a longer-term plan to establish at NPL an absolute cross-section measurement capability useful for example to improve reference cross sections.

The experimental setup

The novelty of the UoM chamber is the use of the relative timing of the charge integrated signals from a triply segmented anode to measure fission fragments (FF) angular distribution. The advantage of this method is that it is independent on the FF energy, depends only on the geometry of the detector and the drift velocity of liberated electrons. The energy independence means that corrections for Frisch-grid inefficiency and gain matching of pre-amplifiers are not required. The chamber was installed at the NPL monoenergetic neutron facility, which consists of a 3.5 MV Van de Graaff accelerator producing charged particle beams impinging on deuterium or tritium targets located in the center of a low neutron-scattering bay (18 x 18 x 26 m^3).

^{236,238}U targets

One of prerequisite to be able to measure cross section is the availability of thin targets. In our case the required targets were made at PSI, using molecular plating to deposit ≈700 μg of ^{236,238}U on a 180 μg/cm^2 C-foil (see Fig. 1). The relatively large size of the target (30 mm diameter) required construction of a dedicated cell. The targets were manufactured and shipped to NPL in April 2021. Figure 1 shows a picture of the ^{238}U target mounted on the UoM fission chamber cathode. The total mass was determined using a defined-solid-angle alpha counter. This measurement showed contamination of ^{234,235,236}U, which are tolerable in terms of mass fraction. Unfortunately, the contamination of ^{236}U makes it difficult to quantify ^{235}U. Despite its small mass, ^{235}U needs to be characterized because of the possible presence of thermal neutrons. This was determined to be ≈0.1% by mass spectrometry using a sample of U used for target manufacture.

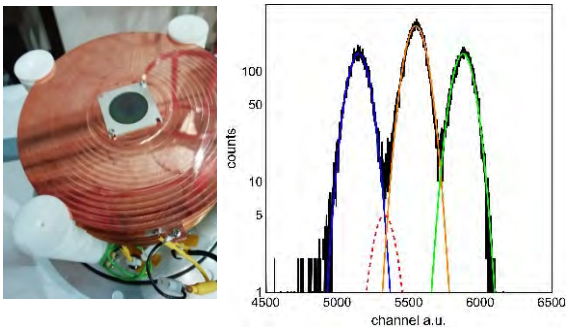

Figure 1: (left) ^{238}U target mounted on the chamber cathode, (right) target alpha spectrum. Very small tails confirm the quality of the thin deposition. The different colors corresponds to ^{238}U (blue), ^{236}U (orange), ^{234}U (green), and ^{235}U (dotted red).

Measurements

Measurements were completed for both targets using the reactions T(p,n)^{3}He, D(d,n)^{4}He, T(d,n)^{4}He, with primary beams tuned to produce neutrons of 2.5 MeV, 5 MeV, and 16.5 MeV, respectively. Figure 2 shows a picture of the experimental setup. Data analysis is currently ongoing but preliminary results for ^{238}U show that the ratios of cross sections for the three energies agree with evaluations.

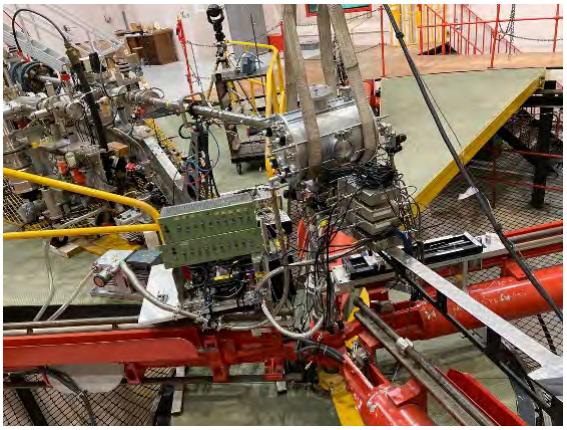

Figure 2: experimental setup with the UoM chamber in the centre of the low neutron scattering bay.

References

[1] S. Bennet et al., *Nucl. Inst. Meth. Phys. Res. A*, **951** (2020), pp. 162846

Study of the ^{171}Tm(n, γ) reaction with the DANCE array at LANSCE

A. Stamatopoulos, A. Couture, P. Koehler (LANL), E. A. Maugeri, D. Schumann (PSI), C. Guerrero (UoS), C. Fry, E. Leal-Cidoncha, G. Rusev, J. Ullmann (LANL)

Introduction

The majority of elements heavier than iron were created through the slow neutron capture process, commonly referred to as s-process [1]. The s-process proceeds by sequential neutron captures on a given elemental chain until the β-decay rate of the produced isotope exceeds the neutron capture rate. If the two rates differ substantially, the process follows the faster rate. If the β-decay and neutron capture lifetimes are comparable, however, a branching (a so-called "branch point") forms and the abundance flow splits. These branch points are often the most interesting networks in the s-process as they offer an opportunity to study the physical environment, such as the neutron density or temperature. While a plethora of studies have been completed on stable nuclei, only a limited amount of data sets on radionuclides are available. Since branch-point nuclei are essential to better understand the dynamics of the s-process, their study is of vital importance.

^{171}Tm is a radionuclide in the 170-branching mass region with a 1.9-year half-life. The amount of Tm isotopes in the universe affects the abundance of the stable Yb isotopes, especially the one of ^{170}Yb, which is an s-process-only nucleus. The knowledge, therefore, of neutron capture cross sections around the 170-mass region, can provide information on the abundance of naturally occurring Yb isotopes.

A study of the ^{171}Tm(n,γ) cross section is currently ongoing at the Los Alamos Neutron Science Center (LANSCE) making use of the Detector for Advanced Neutron Capture Experiments (DANCE), a 4π gamma calorimeter consisting of 160 BaF_2 crystals.

Sample fabrication

About 10 mL of ^{171}Tm were recovered from a sample that was previously fabricated [2] in the Paul Scherrer Institute (PSI) and used at another study at n_TOF/CERN and SARAF [3]. A new ^{171}Tm sample was fabricated at PSI, in $TmCl_3$ chemical form. The radioactive material was deposited on a 3 μm thick Ti backing which was glued on an aluminum ring. The deposit itself is 4 mm in diameter. Figure 1 shows a ^{171}Tm drop, being deposited on the Ti backing.

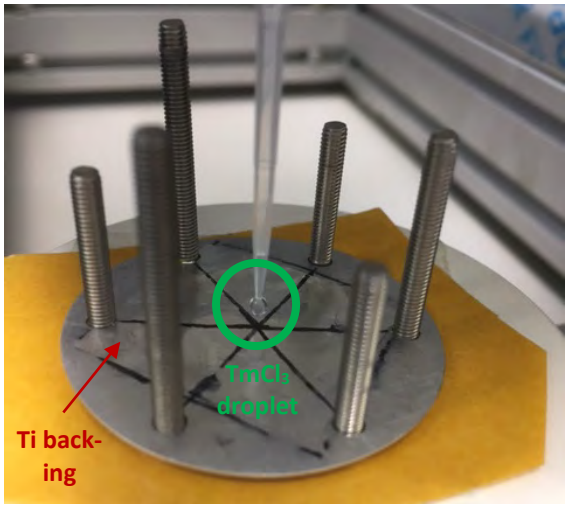

Figure 1: The ^{171}Tm sample, in $TmCl_3$ chemical format, was deposited on a 3 μm thick Ti foil.

Sample irradiation at LANSCE

The ^{171}Tm(n,γ) measurement begun on November 22nd, 2021 and is expected to finish on December 21st, 2021. While the measurement is still on going, a preliminary reconstruction of the excitation function indicates that resonances can be resolved up to at least a few hundred eV, as shown in Figure 2.

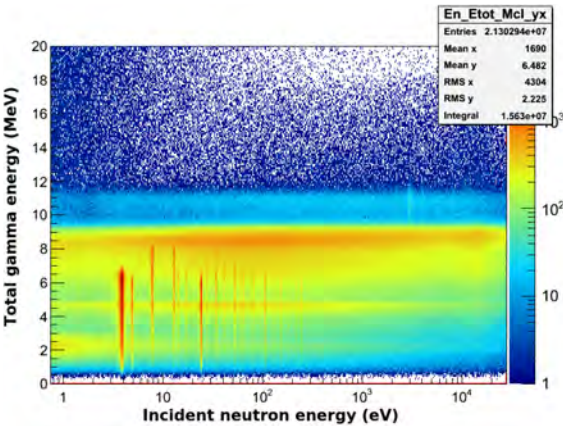

Figure 2: Preliminary results on the excitation function, reveal ^{171}Tm resonances up to ≈400 eV.

References

[1] E. Burbidge et al., *Rev. Mod. Phys.*, **29** (1957), pp. 547-650

[2] Stephan Heinitz et al., *Radiochim. Acta*, **105** (2017), pp. 801-811

[3] C. Guerrero et al., *Phys. Rev. Lett.*, **125** (2020), pp. 142701

Production of terbium-155 for application in nuclear medicine: a comparison study on the possible production routes at PSI

C. Favaretto (ETHZ/PSI), Z. Talip (PSI/CRS), H. Zhang (PSI/GFA), R. Schibli (ETHZ/PSI), R. Eichler, N. P. van der Meulen (PSI)

Introduction

^{155}Tb ($t_{1/2}$ = 5.32 d, E_γ= 87 keV [32%] 105 keV [25%] [1]) is a radionuclide potentially suitable in nuclear medicine towards the diagnosis of disease via single photon emission computed tomography (SPECT). Moreover, together with ^{161}Tb, ^{155}Tb can play an important role towards the radiotheragnostics concept, as they form a perfect "matched pair", with ^{161}Tb being a novel radionuclide produced at Paul Scherrer Institute (PSI) for β^--therapy [2,3]. Therefore, the availability of large quantities of ^{155}Tb with adequate purity would be of particular value for clinical application. The production of ^{155}Tb via ^{155}Gd(p,n)^{155}Tb and ^{156}Gd(p,2n)^{155}Tb nuclear reactions, and the radiochemical separation thereof from the target material, were recently published [4]. The aim of this work was to increase the production yield of the abovementioned nuclear reactions and to study a third possible production route at PSI: ^{nat}Tb(p,5n)^{155}Dy → ^{155}Tb.

Methods

The mass of the target material used for the ^{155}Gd(p,n)^{155}Tb and ^{156}Gd(p,2n)^{155}Tb nuclear reactions was increased from 40 mg to 100 mg, in order to increase the production yield. To maintain the same thickness of the target and in order to keep the same energy irradiation conditions, the diameter was increased from 6 mm to 10 mm, and the shape of the target capsule modified (Figure 1). The enriched gadolinium oxide targets ($^{155}Gd_2O_3$ and $^{156}Gd_2O_3$) were irradiated for up to 4 hours at PSI's IP2 irradiation station, receiving 72 MeV protons from the Injector II separated sector cyclotron. Niobium discs of thickness 3.4 mm and 2.4 mm, respectively, were used as degraders to decrease the proton energy from 72 MeV to ~10 MeV for the (p,n) reaction and ≈ 23 MeV for the (p,2n) reaction. Moreover, the ^{nat}Tb(p,5n)^{155}Dy → ^{155}Tb indirect nuclear reaction was studied by proton irradiation of 40 mg terbium oxide targets for up to 2 hours at IP2 irradiation station. After the irradiations, the targets were left to decay, before the ^{155}Tb activities were determined by γ-spectrometry using a high-purity germanium (HPGe) detector.

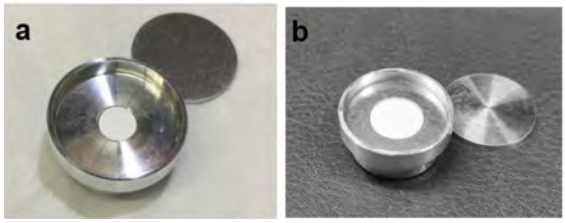

Figure 1: Open target capsule containing a 6-mm (a) and a 10-mm (b) gadolinium oxide target nestled in an indentation.

Results and discussion

In agreement with the previous results [4], the (p,2n) reaction yielded higher activities compared to the (p,n) reaction. In particular, with 4 hours irradiation of a $^{155}Gd_2O_3$ target, ≈ 90 MBq ^{155}Tb was produced, while the same irradiation time on $^{156}Gd_2O_3$ targets yielded activities up to 1.7 GBq. With the increment of the target material and the target shape changes with respect to the previous study [4], the production yield of the ^{156}Gd(p,2n)^{155}Tb reaction was doubled, while the yield obtained from the ^{155}Gd(p,n)^{155}Tb reaction did not increase. In addition, the irradiations of the 40 mg $^{nat}Tb_4O_7$ targets produced ≈ 500 MBq ^{155}Tb after 2 hours of irradiation, which is a production yield comparable with that obtained with the (p,2n) reaction for 40 mg targets [4]. However, a decreased radionuclidic purity profile was observed for this indirect production route in comparison with the ^{155}Gd(p,n)^{155}Tb and ^{156}Gd(p,2n)^{155}Tb nuclear reactions, respectively. In particular, higher activities of ^{156}Tb were measured in the $^{nat}Tb_4O_7$ irradiated targets compared to those observed in the gadolinium oxide targets after irradiation.

References

[1] N. Nica, *Nucl. Data Sheets,* **160** (2019), pp. 1-404
[2] N. Gracheva et al., *EJNMMI Radiopharm. Chem.*, **4**(12) (2019), pp. 1-16
[3] C. Müller et al., *J. Nucl. Med.,* 53 (2012), pp. 1951-59
[4] C. Favaretto et al., *EJNMMI Radiopharm. Chem.*, **6**(37) (2021), pp. 1-17

Efficient production of high specific activity ^{167}Tm at PSI and CERN-MEDICIS

Z. Talip (PSI/CRS), R. Heinke (CERN/KU Leuven), E. Chevallay, K. Chrysalidis (CERN), T. E. Cocolios (KU Leuven), C. Duchemin (CERN/KU Leuven), V. Fedosseev (CERN), S. Hurier (KU Leuven/SCK CEN), L. Lambert (CERN), B. Leenders (KU Leuven/SCK CEN/Ghent Univ.), B. Marsh (CERN), N. P. van der Meulen (PSI), P. Sprung (PSI/AHL), T. Stora (CERN), M. Tosato (PSI/CRS), S. Wilkins (CERN), H. Zhang (PSI/GFA)

Introduction

The application of radionuclides emitting Auger electrons (AE) is a promising path in radiotherapy due to their high radiotoxicity in the vicinity of the cell nucleus DNA [1,2]. Yet, the radiobiological effects are still to be fully understood. Due to their analogous coordination chemistry, radiolanthanides provide great potential for comparative clinical studies of the influence of AE. Following the clinical approval of ^{177}Lu ("LUTATHERA"®), research on no-carrier-added production of ^{175}Yb, ^{169}Er [3] and several Tb isotopes have been performed at PSI and CERN-MEDICIS, respectively.

^{167}Tm is a candidate for combined medical diagnostics and therapy ("theragnostics") due to its suitable gamma emission for SPECT imaging accompanying the conversion/Auger electron emission.

This report presents a synopsis of the recently-published article on high-specific-activity ^{167}Tm production by proton irradiation of Er_2O_3 targets at PSI, followed by mass separation at MEDICIS [4].

Mass separation efficiency

Three natural Er_2O_3 targets were irradiated at the PSI IP2 irradiation station with 72 MeV protons from the Injector II cyclotron. A 2.4-mm Nb disc was used to degrade the proton energy to ≈ 22.8 MeV. Targets of ≈ 30 mg each were exposed to 50 µA beam current for 8 h, resulting in ^{167}Tm activities of ≈ 100 to 150 MBq seven days after irradiation, after waiting for the co-produced ^{166}Tm to decay.

The irradiated Er_2O_3 pellets were sent to MEDICIS, without further processing, and mass separation was performed in a 60 keV ion beam magnetic mass separator [5], assisted by resonant laser ionization of thulium [6]. The ion beam was implanted into zinc-coated gold foils, which were subsequently sent back to PSI for quality control.

The separation efficiencies, defined as the ratio between total collected activity on the collection foils at end of the mass separation process with respect to the activity available in the irradiated Er_2O_3 pellets at the start of the process (also including decay over the ≈ 3-day process duration), varied between 11(2)% and 20(3)%.

This presents a significant difference to the previously measured ≈ 60% efficiency at a non-radioactive ^{165}Tm test run and particularly to values between 27% and 45%, measured by an in-situ γ-ray detector directly mounted to the implantation chamber during collections ("extraction efficiency") as shown in Table 1, targets #1 - #3.

TABLE 1: Overview of mass separation process efficiencies. The significant difference between extracted and collected activity is attributed to strong ion-beam sputtering on the zinc-coated collection foils. The relative effect was reduced using aluminum coatings (target #4), but more pronounced using copper (target #5). As #4 and #5 were only partially used for the respective tests, no total efficiency can be given in either case.

Target	^{167}Tm act. (MBq)	Extr. act. (MBq)	Coll. act. (MBq)
#1	83(8)	33.8 → 41%	9(2) → 11(2)%
#2	77(7)	34.4 → 45%	15(2) → 20(3)%
#3	123(12)	33.1 → 27%	19(3) → 16(3)%
#4	n.a.	18.5	13.7
#5	n.a.	18.5	3.1

It could be attributed to sputtering effects on the collection foils, leading to loss of already collected activity on the foils which then condensed on different parts in the chamber. As a mitigation method, the collection was divided over multiple foils, reducing the ion beam exposure of each one to the possible minimum. In a follow-up study, aluminum and copper coatings were tested instead of zinc. While in the case of zinc, only around half of the ^{167}Tm activity measured by the in-situ detector in the whole collection assembly was found on the foils (targets #2 and #3), for the case of aluminum this ratio increased to 75% for similar operation parameters. For copper, less than 20% of the overall extracted activity was found on the foils (targets #4 and #5). With these findings, an overall separation efficiency on the foils in the order of 40% is projected. Further improvements might be possible by investigating carbon as even more suitable implantation material and reducing the initial erbium content before the separation process, as the mass 167 ion beam comprises an up

to 1000-fold surplus of stable ^{167}Er over ^{167}Tm in the current production process.

Sample characterization

An irradiated test Er_2O_3 target and a selection of implanted zinc-coated foils were characterized by γ-ray spectrometry, ICP-MS, and ICP-OES at PSI for assessment of the mass separation process quality. While for a foil implanted under good conditions in terms of sputtering and ion beam composition no ^{168}Tm impurities could be detected three months after collections (see Fig. 1), a respective impurity of 0.04% at end of collection was found for a foil with worse conditions.

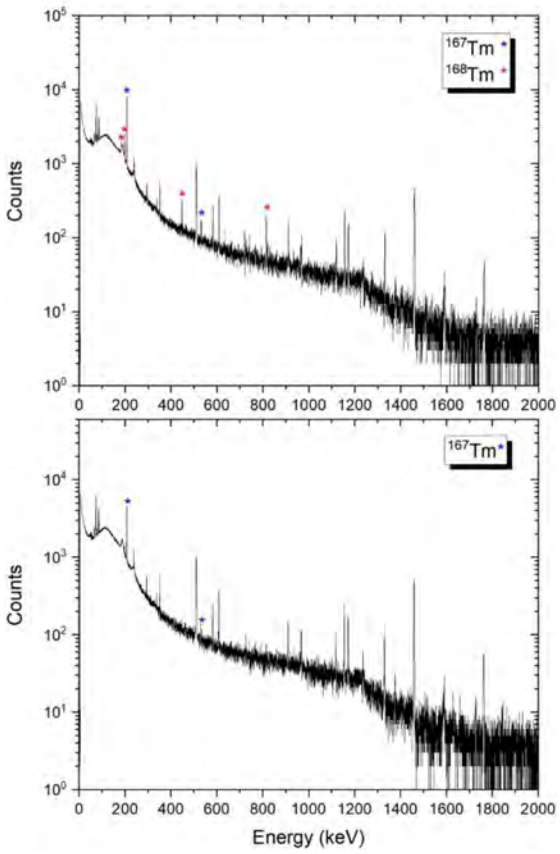

Figure 1 : Gamma-ray spectra of an irradiated Er_2O_3 target upper panel) and a sample after mass separation (lower panel). Figure adapted from [4].

Measurements using the natural erbium also present in the foils confirmed a reduced performance of a neighboring mass suppression factor of around 200 for this foil, compared to around 1000 for good conditions. This can be explained as the sputtering effect is more pronounced in the center of the implantation, where the desired species suffer more than the tailings from neighboring mass beams at the edges of the collection foils. Also, in this case, developments towards mitigation of sputtering will improve the process quality.

The combination of resonant laser ionization of thulium, yielding a 50 to 70-fold enhancement of thulium ion production over unselective surface ionization in the ion source, and favorable volatilization characteristics of thulium over erbium enable a more than 1000-fold suppression of erbium from the irradiated sample. Specific activities in the order of several MBq/μg ^{167}Tm were achieved. Yet, additional erbium removal (at any stage) is required to provide samples suitable for preclinical studies. In addition, ICP-OES results showed that DGA resin is not sufficient for the complete removal of zinc when dissolving the implanted samples, where a ^{167}Tm loss of less than 2% was confirmed.

Outlook

To date, already the achieved separation efficiency of 20(3)% presents a record value for the MEDICIS facility with external activity sources. The developments in sputtering mitigation will help to improve the process also for other isotopes. Alternative ^{167}Tm production paths such as using isotopically enriched erbium or ytterbium via ^{167}Lu decay are envisaged and will allow for preclinical studies with already developed ligands for use in targeted tumour radiotherapy.

References

[1] H. H. Ertl et al., *Phys. Med. Biol.,* **15** (1970), pp. 447
[2] L. E. Feinendegen et al., *Rad. Environ. Biophys.* **12** (1975), pp. 85-99
[3] Z. Talip et al., *Front. Med.,* **8** (2021), pp. 479
[4] R. Heinke et al., *Front. Med.,* **8** (2021)
[5] Y. Martinez Palenzuela et al., *Front. Med.,* **8** (2021)
[6] M. Mostamand, PhD thesis, The University of Manitoba (2020)

Investigation of different production routes and cross section measurements of medically relevant radionuclide ^{167}Tm

E. Renaldin (PoliMi/PSI), G. Dellepiane (Univ. Bern), A. Sommerhalder (PSI/ZRW), H. Zhang (PSI/GFA), S. Braccini (Univ. Bern), N. P. van der Meulen (PSI), Z. Talip (PSI/CRS)

Introduction

The development of an efficient production route of the radionuclide ^{167}Tm is relevant for a double application in the medical fields of therapy and diagnostics. In the latter, ^{167}Tm can be used as a radiotracer for Single Photon Emission Computed Tomography (SPECT) due to the emission of a gamma-ray of 207.8 keV with high intensity (I_γ = 42%) and half-life $t_{1/2}$ = 9.25 d. Considering that ^{167}Tm decays by electron capture (EC), it is additionally an Auger electron emitter, whose characteristics appear to be suitable for therapeutic applications [1]–[3]. Nonetheless, the radiobiological effects induced by the deposited dose of Auger electrons still need to be further investigated, thus, justifying the need to produce high activities in order to allow thorough assessments.

Investigated routes

In this study, five different production routes were investigated:

1) ^{167}Er(p,n)^{167}Tm
2) ^{168}Er(p,n)^{167}Tm
3) ^{nat}Yb(p,xn)^{167}Lu → ^{167}Yb → ^{167}Tm
4) ^{171}Yb(p,xn)^{167}Lu → ^{167}Yb → ^{167}Tm
5) ^{nat}Tm(p,3n)^{167}Yb → ^{167}Tm

($^{167}Er_2O_3$ 96.3%, $^{168}Er_2O_3$ 97.2% and $^{167}Yb_2O_3$ 95.5% enrichment, Isoflex, USA).

Direct (cases (1), (2)) and indirect (cases (3), (4), (5)) production routes, using natural and enriched target material, were explored to maximize the final activity and minimize the radionuclidic impurities.

Different irradiation parameters were tested for each of the listed routes at the IP2 irradiation station, served with a 50 µA proton current drawn from the Injector II cyclotron at Paul Scherrer Insititute (PSI). Routes (1) and (2) were also studied with an 18 MeV medical proton cyclotron in operation at the Bern University Hospital, where cross-section measurements and production tests were performed.

Comparison of different production routes

The 72 MeV proton energy available at IP2 allows the possibility of studying a wide range of reactions, where proton energy degradation is obtained with niobium discs of various thicknesses. The proton energies employed for the listed routes vary between 8.6 – 62.7 MeV at PSI, where discs of 6 and 10 mm diameter of different oxides were irradiated and their radionuclidic composition characterized via γ-ray spectrometry using a HPGe detector. **Error! Reference source not found.**1 shows the highest activities produced at end of bombardment (EOB).

TABLE 1: Maximum activities at EOB produced after 1 hour irradiation at PSI IP2 irradiation station.

Prod. route	Proton energy [MeV]	Activity EOB [MBq]
1	13.2	36
2	18.4	195
3	62.7	70
4	53.2	118
5	26.3	152

Cross section measurements

The reactions involving enriched materials of erbium oxides represent an interesting choice, since they can be triggered by proton energies available with medical cyclotrons [4]. For this purpose, they were also explored at the University of Bern, where additional cross-section studies were performed with a specific irradiation station located at the end of the Beam Transfer Line (BTL) that brings the proton beam to a research bunker with a neat control of all irradiation parameters [5].

Several targets of erbium oxide of both enrichments were irradiated with various proton energies from 18.2 MeV to 6.5 MeV, degrading the beam using aluminum foils. Immediately after irradiation, the generated activity was measured to detect and quantify

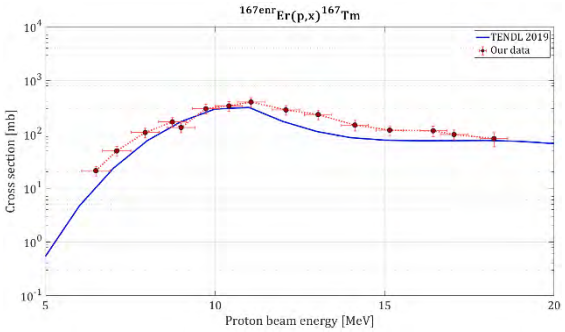

Figure 1: Production cross section of ^{167}Tm from enriched $^{167}Er_2O_3$.

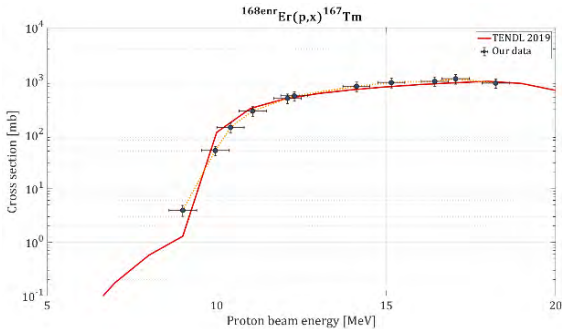

Figure 2: Production cross section of ^{167}Tm from enriched ^{168}Er.

the radionuclidic composition of each sample, retrieving the cross-sections of not only ^{167}Tm, but also of its impurities: ^{165}Tm, ^{166}Tm and ^{168}Tm.

It was observed that the theoretical calculations reported in the TENDL 2019 library [6] are in good agreement with experimental data (see Fig. 1 and 2).

Afterwards, four production tests, two for each material composition, were carried out in the BTL to validate the excitation functions and to assess the amount of activity produced.

TABLE 2: Experimental and theoretical (given between parenthesis and in italic) production yields of ^{167}Tm obtained using enriched $^{167}Er_2O_3$ and $^{168}Er_2O_3$ target materials.

Material		$^{167}Er_2O_3$	$^{168}Er_2O_3$
Proton energy [MeV]		12.6	18.2
Production yield [MBq/μAh]	Target 1	2.4 ± 0.5 *(2.9)*	8.2 ± 1.6 *(9.4)*
	Target 2	2.1 ± 0.4 *(2.6)*	8.5 ± 1.7 *(9.9)*

In **Error! Reference source not found.**2, the yields of production tests are reported with theoretical calculations based on the previously-investigated cross section. Typical proton currents in medical cyclotrons for solid target are around 25 μA, leading to activities of about 56 MBq and 208 MBq for $^{167}Er_2O_3$ and $^{168}Er_2O_3$, respectively (for 1 hour irradiation time).

Conclusions and outlook

The selected production routes have been thoroughly investigated, where routes (2), (4) and (5) gave promising results for additional analyses. Further steps will involve the increase of irradiation time and the testing with larger targets to obtain higher activities, before proceeding with radiochemical separation.

Moreover, the irradiation of $^{168}Er_2O_3$ appears to be the most efficient production route employing a medical cyclotron. However, it is advisable to use proton beams with energy slightly higher than 18 MeV to maximize the production yield. While the (p,n) reaction on $^{167}Er_2O_3$ can be exploited in any medical cyclotron, its cross-section peak is significantly lower.

References

[1] M. Neves et al., *J. Radioanal. Nucl. Chem.*, **266**(3) (2005) pp. 377-384
[2] D. Filosofov et al., *Nucl. Med. Biol.*, **94–95** (2021), pp. 1-19
[3] H. Uusija et al., *J. Nucl. Med.*, **47** (2006) pp. 807-814
[4] S. Braccini, *Proceedings of Cyclotrons 2016*, Zurich, Switzerland (2016) TUD01, p. 229 (www.jacow.org)
[5] S. Braccini, *AIP Conf. Ser. Proc.*, **1525** (2013) p. 144
[6] A. J. Koning et al., *Nucl. Data Sheets*, **155** (2019), pp. 1-55

Production of terbium-149 from spallation-induced reactions on tantalum: chemical separation and preclinical update

C. Favaretto (ETHZ/PSI), P. V. Grundler (PSI/CRS), C. C. Hillhouse (PSI), K. Johnston (ISOLDE-CERN), U. Köster (ISOLDE-CERN/ILL), S. D. Busslinger (PSI), C. Müller (PSI/CRS), N. P. van der Meulen (PSI)

Introduction

Terbium-149 is a particularly interesting radionuclide: it is one of four terbium radioisotopes that can be effectively utilized for medical purposes. It decays with 17% emission α-particle intensity (E_α= 3.97 MeV). Its half-life is relatively short (4.1 h), however, it has no α-emitting daughters and, therefore, is potentially interesting for Targeted Alpha Therapy (TAT). Thanks to its β^+-emission, its use has been demonstrated for positron emission tomography (PET), making it even more interesting as one can image what one treats [1]. As in previous ISOLDE campaigns, mass-separated beams of ^{149}Tb were implanted into Zn-coated Au foils. With collections lasting 6 to 9 hours followed by 1 to 1.5 hours decay before shipping, up to 450 MBq ^{149}Tb were transported to PSI. Due to logistics and the time taken to transport the collection from CERN to PSI, up to 250 MBq arrived on site for processing.

Methods

A Zn layer with uniform thickness had been deposited by physical vapour deposition on Au foils at CERN and, subsequently, used for the ion implantations.

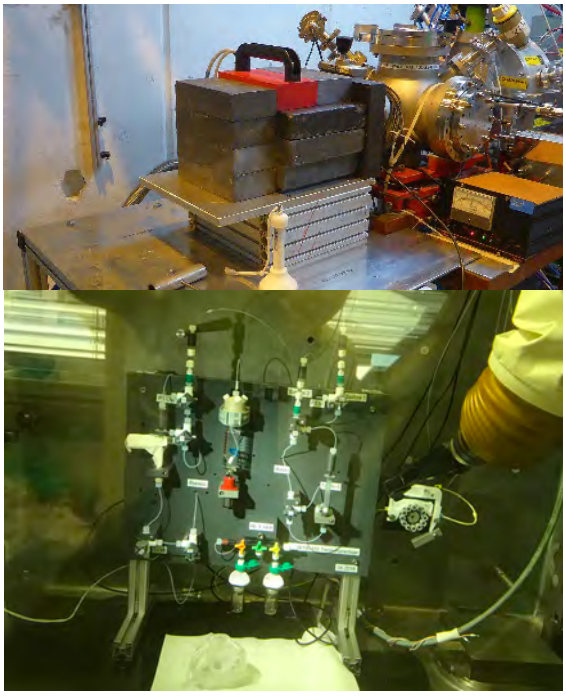

Figure 1: ISOLDE collection chamber (top); ^{149}Tb chemical separation system in a hot cell (bottom).

Upon arrival at PSI, the foil was removed, placed into a hot cell and introduced to the chemical separation system, where the Zn layer on the Au foil was dissolved in dilute nitric acid. The solution was neutralized and loaded onto a small column containing Sykam macroporous strongly acidic cation exchange resin, as previously reported [1-3] (Fig 1, right). The desired ^{149}Tb was eluted using α-HIBA and passed through a small column containing LN3 extraction resin. The final product was eluted using dilute HCl, where it could be utilized directly for radiolabelling of DOTATATE.

Results and discussion

The product was effectively separated from its (pseudo-)isobaric impurities and the Zn matrix, yielding a chemically and radionuclidically pure product at a yield of ≈ 100 MBq ^{149}Tb at End of Separation (EoS, see Fig. 2).

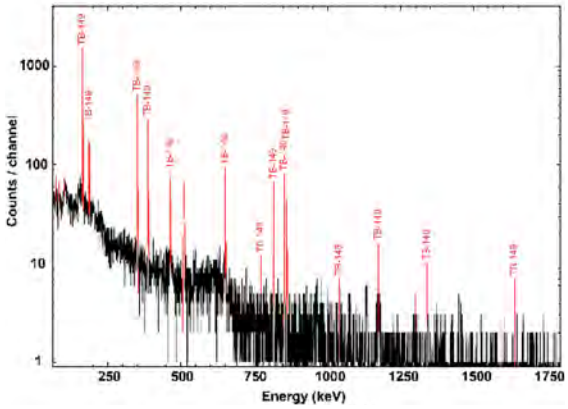

Figure 2: γ-spectrum of the ^{149}Tb final product (≈ 0.5 MBq, acquisition time 900 s), indicating its radionuclidic purity.

The product in question was successfully used for labelling of DOTATOC at high molar activity of up to 20 MBq/nmol (^{149}Tb-DOTATATE) with radiochemical purity of > 99% (see Fig. 3).

The latest run of experiments in the PSI/ISOLDE collaboration proved to be the most successful to date, with reproducibly harvesting ^{149}Tb. The radionuclide was successfully used to label the desired ligands and the ^{149}Tb-radiopharmaceutical evaluated preclinically. While initial results appear encouraging, long-term therapy evaluation results are pending.

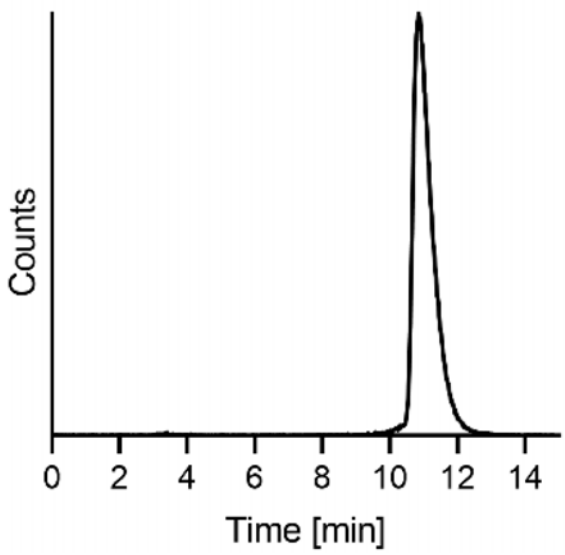

Figure 3: Representative chromatogram of the quality control performed by reversed-phase high performance liquid chromatography for [^{149}Tb]Tb-DOTATATE (retention time t_R = 10.9 min). Traces of unreacted terbium-149 appeared at t_R = 3.2 min.

References

[1] C. Müller *et al*., EJNMMI Radiopharm. *Chem.,* **1**(5) (2016) pp. 1-5

[2] C. Müller *et al.*, EJNMMI Research **6**(35) (2016), pp. 1-10

[3] N. Gracheva et al., *EJNMMI Radiopharm. Chem.*, **4**(12) (2019), pp. 1-16

[4] C. Müller et al., *J. Nucl. Med.,* **53** (2012), pp. 1951-59

Study of radionuclides towards theragnostics with the Bern medical cyclotron

P. Casolaro, G. Dellepiane (AEC/LHEP, Univ. Bern), C. Favaretto (ETHZ/PSI), P. V. Grundler (PSI/CRS), I. Mateu, P. Scampoli (AEC-LHEP, Univ. Bern), Z. Talip (PSI/CRS), N. P. van der Meulen (PSI) S. Braccini (AEC/LHEP, Univ. Bern)

Introduction

Radionuclides for theragnostics are essential for nuclear medicine developments. Their production using solid targets is challenging and requires an accurate knowledge of the production cross sections. A research program is ongoing at the Bern University Hospital (Inselspital), where an IBA Cyclone 18/18 HC medical cyclotron (18 MeV proton beams, max 150 µA, 8 out ports) is in operation [1]. The cyclotron is equipped with a Solid Target Station (STS) and a 6-m Beam Transfer Line (BTL), bringing the beam into a separate bunker with independent access. To irradiate compressed powder pellets, a novel target coin was conceived and realized, together with methods to assess the production cross sections.

Cross section measurements

For an optimized radionuclide production, the precise knowledge of the reaction cross sections is crucial. A novel method to measure cross sections using targets, in powder form, was developed by the Laboratory for High Energy Physics (LHEP) group [2]. The targets are prepared by sedimentation from a suspension of a few milligrams of material in water or ethanol on an aluminum disc with a pocket (4.2 mm in diameter, 0.6 mm deep) in its center. This results in a target thickness that is not precisely controlled. The new procedure is then based on the irradiation of the full target mass with a flat proton beam (Figure 1), instead of the usual method based on the irradiation of a homogeneously thick target. The beam is flattened by the optical elements of the BTL and its position and shape are monitored online with the UniBEaM detector [3,4], based on silica doped fibers passing through the beam. The proton current hitting the target is measured by means of a custom target station composed of a 6-mm-diameter collimator, a target holder and an electron suppressor ring. The collimator is grounded and provides a beam of controlled diameter, within which the beam flatness is better than 5%. The target holder is connected to an ammeter for current measurements on target. The electron suppressor ring is connected to a negative bias voltage to repel secondary electrons produced during the irradiation that would lead to an artificial increase in the measured beam current. The conductive parts of the target station are kept together by insulator components. The beam energy is degraded by means of aluminum attenuator discs placed in front of the target and is determined using the SRIM Monte Carlo code [5]. The activated radionuclides are measured with a calibrated HPGe detector. With this method, the production cross section of several radionuclides (^{43}Sc [2], ^{44}Sc [2], ^{47}Sc [6], ^{48}V [2], ^{61}Cu, ^{68}Ga, ^{155}Tb [7], ^{165}Tm, ^{167}Tm and related impurities) was measured.

Whenever possible, data are compared with TENDL theoretical predictions and/or other experimental data available in the literature (see Fig. 2).

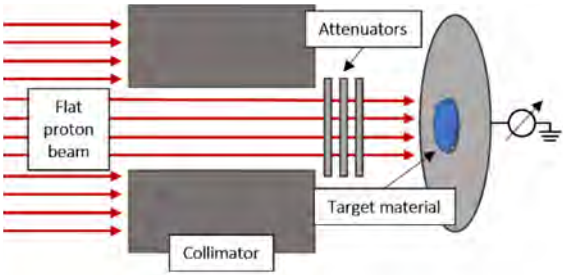

Figure 1: New cross section measurement procedure based on proton beams with a flat profile.

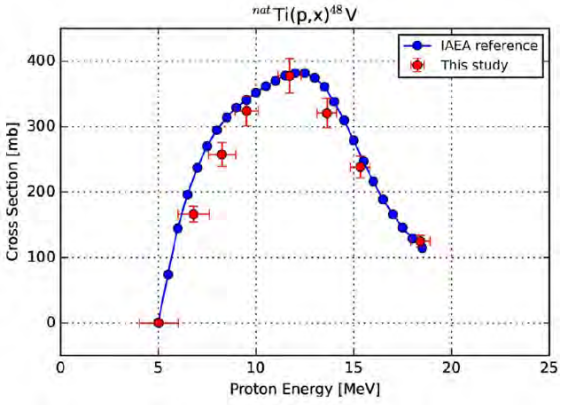

Figure 2: Measured cross section for the reaction ^{nat}Ti(p,x)^{48}V compared to IAEA reference data [2].

Solid target developments

The solid target station (STS) is installed on one outport of the cyclotron and allows the production of novel radionuclides by irradiation of solid material. To irradiate compressed-powder pellets or solid foils, a new target coin composed of two halves kept together by small permanent magnets (see Fig. 3), was conceived and realized by LHEP. Thanks to an accurate knowledge of the cross sections, the produced activity and the radionuclidic purity can be optimized by adjusting the energy of the protons reaching the target. The optimal energy is achieved

by choosing the appropriate material and thickness of the front part of the coin. The back part hosts the 6-mm pellet and an O-ring to prevent the leakage of molten material or any gas produced during the irradiation. To limit overheating, the coin is water-cooled and helium-cooled on the back and the front side, respectively.

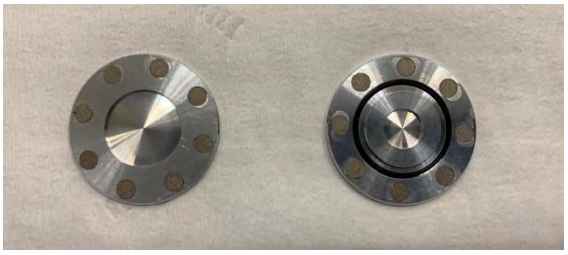

Figure 3: The coin target (24 mm diameter, 2 mm thick).

The STS was complemented with a mechanical transfer system (named Hyperloop [8]) designed by LHEP and with a pneumatic target transfer system (STTS) by TEMA Sinergie. The former allows one to load the target station without entering the cyclotron bunker, minimizing the dose to the personnel. The latter is used to deliver the irradiated target either to a hot cell in the nearby GMP radio-pharmacy or to a reception station located in the BTL bunker. To assess the activity at the End of Beam (EoB) by means of gamma spectrometry, a system based on a 1 cm^3 CdZnTe (CZT) crystal was installed in the reception station. The detector was experimentally calibrated with a High Purity Germanium detector (HPGe) and allows the measurement of the activity produced with an accuracy of a few percent [9]. Thanks to these developments, several radionuclides have been produced at the Bern medical cyclotron with the solid target station, as reported in Table 1.

TABLE 1: Main achievements in non-standard radioisotope production obtained with the STS at the Bern medical cyclotron.

Isotope	Reaction	Target	Y [GBq/µAh]
^{44}Sc [10]	(p,n)	^{enr44}CaO pellet	0.6
^{47}Sc	(p,α)	^{enr50}Ti pellet	0.001
^{48}V	(p,n)	^{nat}Ti foil	0.015
^{61}Cu	(p,α)	^{enr64}Zn pellet	0.08
^{64}Cu	(p,n)	^{enr64}Ni deposition	0.13
^{68}Ga	(p,n)	^{enr68}Zn pellet	6
^{155}Tb [11]	(p,n)	$^{enr155}Gd_2O_3$ pellet	0.005
^{165}Er	(p,n)	^{nat}Ho foil	0.015
^{165}Tm	(p,2n)	$^{enr166}Er_2O_3$ pellet	0.07
^{167}Tm	(p,n)	$^{enr167}Er_2O_3$ pellet	0.002

References

[1] S. Braccini et al., *Proceedings of Cyclotrons 2019* (Cape Town: JACoW), p. 127

[2] T.S. Carzaniga et al., *Appl. Radiat. Isot.,* **129** (2017), pp. 96-102

[3] M. Auger et al., *J. Instrum.,* **11** (2016), p. 03027.

[4] D.E. Potkins et al., *Phys. Proced.,* **90** (2017), pp. 215-222

[5] J.F. Ziegler et al., *Nucl. Instrum. Methods,* **B35** (1988), p. 215

[6] T.S. Carzaniga et al., *Appl. Radiat. Isot.,* **145** (2019), pp. 205-208

[7] G. Dellepiane et al., *submitted to Appl. Radiat. Isot.,* (2022)

[8] G. Dellepiane et al., *Proceedings of TIPP2021* (online format)

[9] G. Dellepiane et al., *IL NUOVO CIMENTO,* **44C** (2021), p. 130

[10] N.P. van der Meulen et al., *Molecules,* **25** (2020), pp. 1-16

[11] C. Favaretto et al., EJNMMI Radiopharm. Chem., **6** (2021), p. 37

Precise activity measurement of Sc-44 and half-life determination of Sc-44 and Sc-44m

S. Braccini, G. Dellepiane (Univ. Bern), M. T. Durán (IRA-CHUV), P. V. Grundler (PSI/CRS), F. Juget (IRA/CHUV), Y. Nedjadi (IRA-CHUV), Z. Talip (PSI/CRS), N. P. van der Meulen (PSI)

Introduction

A collaboration between PSI, Bern University and IRA sparked the interest in having a precise activity measurement of ^{44}Sc sources generated at PSI for the calibration of gamma spectrometry systems and dose calibrator at Bern and PSI. This calibration will allow performing quick and practical on-site activity measurements of ^{44}Sc sources generated in those facilities.

IRA performed the precise activity measurement, as they are the designated Swiss laboratory for the primary standardization of radionuclides. The half-lives of ^{44}Sc, and its associated impurity of ^{44m}Sc, were also determined by multiple techniques.

The process was also a challenging experience in terms of logistics, as the source prepared at PSI was separated into three parts: one to be measured on-site, another one to be delivered and measured at Bern University and the latter to IRA in Lausanne. The limiting factor was the half-life of ^{44}Sc, of approximately 4 hours.

Source preparation at PSI

Following production and purification of ^{44}Sc at PSI, five different sources were prepared using the same solution: two glass vials, called production and penicillin, and one plastic Eppendorf tube were each filled with 1 mL. In addition, two plastic Eppendorf tubes were filled with 0.02 mL. An aliquot of this solution was sent to IRA (referred to as M44Sc_PSI).

The glass vials and the Eppendorf tube were measured with the dose calibrator at PSI. The two low-filling Eppendorf vials were used for γ-spectrometry measurement at PSI and Bern University, respectively.

Source preparation at IRA

The ^{44}Sc source was received at IRA in the form of two solutions with different activity concentrations:

1. M44Sc_PSI: 2 g of solution at 35 MBq/g
2. M44Sc_PSI2: 0.5 g of solution at 2 GBq/g

The first solution was diluted and split into two different concentrations to be measured independently and corroborated accordingly by the measurements: M44Sc1 (3.256 MBq/g) and M44Sc2 (0.814 MBq/g). From those two solutions, ampoules, liquid scintillation vials and plastic scintillation sources were prepared for activity concentration measurement together with two vials to check the radionuclidic purity in the HPGe spectrometer and solid sources to determine the half-lives (see Fig. 1).

The second solution was stored until most of ^{44}Sc decayed in order to measure the ^{44m}Sc half-life a few days later. Two solid sources were prepared by deposition onto plastic containers and measured using two methods in parallel.

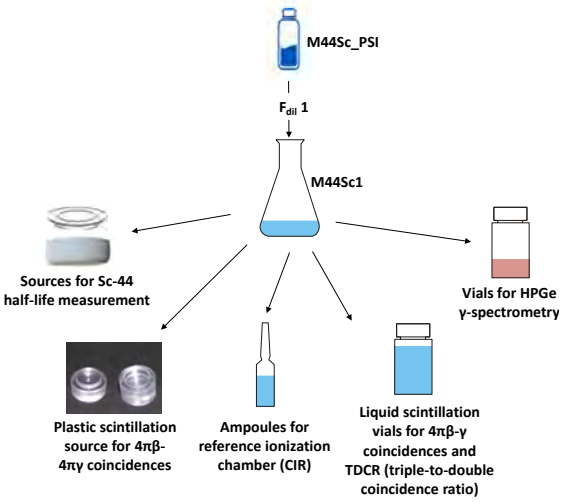

Figure 1: Scheme of source dilution for M44Sc1 solution and preparation of the measurement sources. M44Sc2 was obtained by further dilution of M44Sc1 and the following source preparation is analogous to the one shown in this scheme.

Radionuclide impurities

Measurements were performed using a high-resolution HPGe gamma spectrometer and any other Sc isotopes found along with ^{44}Sc, such as ^{44m}Sc, were reported at the specified reference date.

Half-life measurements

Ionization chambers measurements

Several measurements were made with the two ionization chambers belonging to IRA: CIR (reference ionization chamber) and TCIR (transportable reference ionization chamber).

The CIR is a high-stability well-type 4πγ Centronic IG11, sealed and filled with Ar at 2 MPa pressure. The chamber is shielded by a 5-cm-thick lead cylinder and located in a temperature-controlled room. An automated electronic system measures the current [1].

The TCIR [2] is a sealed well-type 4πγ Centronic IG12 filled with Ar at 2 MPa pressure. The ionization current is read by a Keithley 6517B digital electrometer with fixed range.

The decay rate was observed over periods of at least four half-lives for ^{44}Sc (see Fig. 2) and two half-lives for ^{44m}Sc. The current was measured at regular intervals and corrected for background, decay during measurement and saturation. Biexponential decay curves were fitted to the datasets corresponding to the measurements of ^{44}Sc half-life to take the ^{44m}Sc impurity into account.

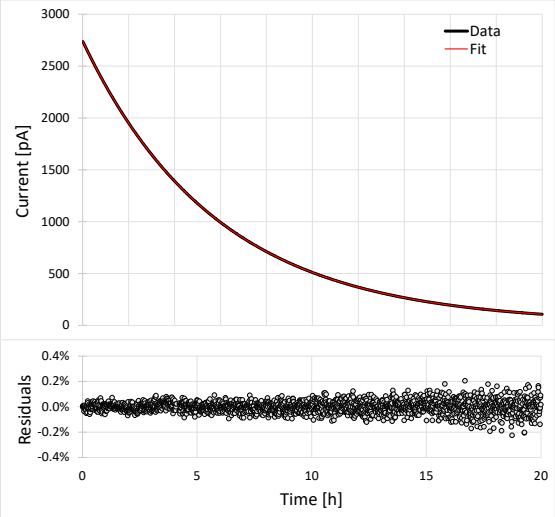

Figure 2: Decay data and fit with residuals for the determination of ^{44}Sc half-life. The measurement was performed with the TCIR for 20h.

Gamma spectrometry measurements

Two γ-spectrometers were used to follow the decay rate of the sources for the same periods stated above.

The first, a Scionix $CeBr_3$ detector type 51B51/2M-CEBR-E1, consists of a 51 × 51 mm $CeBr_3$ crystal integrally coupled to a photomultiplier tube. This detection system was housed at the bottom of a cylindrical shield covered with lead bricks. The detector output is connected to a dedicated Scionix preamplifier from where the signal is collected and fed into two parallel electronic systems [3,4]. The second is a Quartz & Silice 127-SPE-127 12.5 x 12.5 cm NaI(Tl) well-type detector connected to a NI digital electronics system.

In these cases, the curves fitted were also double and triple exponential decay curves, including the decay-correction factors, for each measurement.

Results and discussion

The half-life values for ^{44}Sc and ^{44m}Sc were determined.

The uncertainties were evaluated taking into account high (residuals, counting statistics), medium (impurities) and low (background, timing, dead-time) frequency components regarding the length of the measurement campaigns

All the values agree except for the CIR measurement for ^{44}Sc and the analogue $CeBr_3$ measurement for ^{44m}Sc. These cases will have to be addressed in more detail by the calculation of the residual autocorrelation and study of the conditions during the measurements.

Activity concentration measurements

Both solutions obtained from the original one sent by PSI where measured using different activity standardization techniques.

4πβ-(PS)-4πγ(NaI) coincidence counting

This system [5] is composed of a β-detector consisting on a plastic scintillator with a dry radioactive deposit at its center, allowing full solid angle geometry. The scintillator is coupled to the window of a Photonis XP3132 low-noise PMT that is inserted into the well of a Quartz & Silice 127-SPE-127 12.5 x 12.5 cm NaI(Tl) detector. This configuration places the radioactive source at the bottom of the well, interacting with the γ-detector through 99.1% of the full solid angle. The scintillator crystal and the photomultiplier (RTC type XP2050) are housed within a cylindrical shielding. Analogue electronics was used to perform the signal processing and the efficiency variation achieved by electronic discrimination. A dead-time of 29 μs was used in both β- and γ-channels, and the coincidence window set at 1 μs.

One source from M44Sc1 was measured in two γ-energy regimes, a threshold at 364.5 keV and another one at 661.7 keV. A source from M44Sc2 was measured with the threshold at 364.5 keV only. When taking the presence of the Sc-44m impurity into account and its non-equilibrium with the ^{44}Sc it generates, the extrapolation curves of the ^{44}Sc activity concentrations were found to be linear in all cases and yielded values compatible within 0.3%.

4πβ(LS)-γ(NaI) coincidence counting

The detection in the β-channel was performed by liquid scintillation counting in an optical chamber, made with a fluoropolymer with a high diffuse reflectance, which houses two facing 2'' Hamamatsu photomultiplier tubes working in coincidence to reduce noise levels. A NaI detector was placed directly under the 1.5 mm thick aluminum floor of the optical chamber. This detection system is located inside a large shielding enclosure with 5-cm-thick lead walls. The signal was processed with digital electronics modules by CAEN and the efficiency discrimination

and coincidence counting with a LabVIEW code described in [3] from the timestamp and amplitude list-mode data obtained from the CAEN system.

Liquid scintillation counting

To perform liquid scintillation measurements, aliquots of the diluted M44Sc2 solution were dispensed gravimetrically into vials prefilled with 14.5 mL Ultima Gold cocktail, and topped up with variable volumes of ultrapure water to achieve a 6.5 % aqueous fraction.

The TDCR method and the CIEMAT-NIST (CNET) technique were used. Three vials were measured on the IRA TDCR system [6] using a MAC3-module [7] with 100 μs resolving time. Voltage defocusing in 40 V decrements was applied to change the triple and double coincidence detection efficiencies. Three other vials were also measured on the commercial TriCarb 2700 LS commercial counter, along with eleven quenched tritium samples, to determine the calibration curve for the CNET method.

The TDCR triple and double detection efficiencies and the CNET double detection efficiencies were calculated with IRA's own Fortran code, which takes the PMTs asymmetry and the micelle effect into account [8].

TDCR and CNET methods agree within 0.9 % and their average deviates by only 0.1 % from the 4πβ-(PS)-4πγ(NaI) coincidence counting measurements.

Reference ionization chamber

The current produced in the CIR was measured for ISO, IER and BIPM ampoules. These three ampoules have different geometries and a dedicated calibration factor was calculated for each one using the results of the primary measurements. These geometries will be used in the future for characterization of Sc-44 solution.

Results and discussion

The data are currently under evaluation and more calculations are still to be performed to provide a reliable result.

Measurements at PSI

The two glass vials and the Eppendorf tubes were measured at PSI with the dose calibrator and the results compared with the one obtained with primary measurement at IRA (Table 1). A difference of 10% for the glass vials and 8% for plastic Eppendorf was determined. This shows that the calibration factor currently used for the dose calibrator has to be corrected. Two different factors could be used, one for the glass vials and one for the plastic Eppendorf.

TABLE 1: Activity concentration (MBq/g) measured at PSI for the M44Sc_PSI solution

	DOSE CALIBRATOR	DIFF. WITH 1^{RY} MEAS.
PRODUCTION VIAL	45.48	10.1%
PENICILLIN VIAL	45.40	9.9%
EPPENDORF VIAL	44.65	8.1%

Conclusions

Unfortunately, the level of ^{44m}Sc content was too high when the source arrived at IRA for the measurements to deliver the typical uncertainty level in a regular standardization (order of 0.1% relative combined uncertainty). Nevertheless, the measurements were performed satisfactorily, and the anticipated relative uncertainty was ≈ 1%, which is within the expected range for a useful value to calibrate PSI and Bern University γ-spectrometers and dose calibrators.

^{44m}Sc half-life value is comparable with the one reported by NDS of 58.6(1). The half-life obtained, though, for ^{44}Sc is 1.7% different from the reference value of 3.97(4) h [9]. According to the measurements presented in this report and the result published in 2016 of 4.042(25) h [10], a revision of the NDS value will be recommended.

References

[1] H. Schrader, *Monographie BIPM-4: Activity measurements with ionization chambers*. Bureau International des Poids et Mesures, 1997

[2] F. Juget et al. (2018), *Appl. Radiat. Isot.*, **134** (2018), pp. 95-99

[3] M. T. Durán et al., *Appl. Radiat. Isot.*, **134** (2018), pp. 329-336

[4] M. T. Durán et al., *Appl. Radiat. Isot.,* **176** (2021)

[5] Y. Nedjadi et al. (2012), *Appl. Radiat. Isot.*, **70**(1) (2012), pp. 249-256

[6] Y. Nedjadi et al., *Appl. Radiat. Isot.*, **97** (2015), pp. 113-117

[7] J. Bouchard and P. Cassette, *Appl. Radiat. Isot.*, **52**(3) (2000), pp. 669-672

[8] Y. Nedjadi et al., *Appl. Radiat. Isot.*, **125** (2017), pp. 94-107

[9] J. Chen et al., *Nucl. Data Sheets*, **112** (2011) pp. 2357-2495

[10] E. García-Toraño et al., *Appl. Radiat. Isot.*, **109** (2016), pp. 314-318

LIST OF PUBLICATIONS

F. Alves, I. F. Antunes, E. Cazzola, F. Cleeren, B. Cornelissen, A. Denkova, J. Engle, A. Faivre-Chauvet, N. Gillings, J. J.M.A. Hendrikx, A. Jalilian, N. P. van der Meulen, R. Mikolajczak, O. Neels, M.R.A. Pillai, R. Reilly, S. Rubow, Y. Seimbille, S. Spreckelmeyer, W. Szymanski, C. Taddei
Highlight selection of radiochemistry and radiopharmacy developments by editorial board
EJNMMI Radiopharmacy and Chemistry, 6, 13 (2021). DOI: 10.1186/s41181-021-00146-9

F. Alves, T. DeGrado, J. Engle, K. Gagnon, C. Hoehr, A. Jalilian, S. Lapi, M. Pandey, V. Radchenko, F. Rösch, N. van der Meulen
Production of Emerging Radionuclides towards Theranostic Applications: Copper-61, Scandium-43 and -44, and Yttrium-86
IAEA-TECDOC-1955, International Atomic Energy Agency, Vienna, 2021

S. Amaducci, N. Colonna, L. Cosentino, S. Cristallo, P. Finocchiaro, M. Krtička , C. Massimi, M. Mastromarco, A. Mazzone, A. Mengoni, S. Valenta, O. Aberle, V. Alcayne, J. Andrzejewski, L. Audouin, V. Babiano-Suarez, M. Bacak, M. Barbagallo, S. Bennett, E. Berthoumieux, P. Žugec on behalf of the n_TOF Collaboration
First results of the ^{140}Ce(n,γ)^{141}Ce cross-section measurement at n_TOF
European Physical Journal A: Hadrons and Nuclei, 57, 197 (2021). https://doi.org/10.1140/epja/s10050-021-00507-7

V. Babiano-Suárez, J. Lerendegui-Marco, J. Balibrea-Correa, L. Caballero, D. Calvo, I. Ladarescu, P. Žugec on behalf of the n_TOF Collaboration
Imaging neutron capture cross sections: i-TED proof-of-concept and future prospects based on Machine-Learning techniques
Universe, 7, 200 (2021). https://doi.org/10.3390/UNIVERSE7060200

R. P. Baum, A. Singh, H. R. Kulkarni, P. Bernhardt, T. Rydén, C. Schuchardt, N. Gracheva, P. V. Grundler, U. Köster, D. Müller, M. Pröhl, J. Rijn Zeevaart, R. Schibli, N. P. van der Meulen, C. Müller
First-in-Human Application of Terbium-161: A Feasibility Study Using ^{161}Tb-DOTATOC
Journal of Nuclear Medicine (2021). DOI: 10.2967/jnumed.120.258376

P. Bernhardt, J. Svensson, J. Hemmingsson, N. P. van der Meulen, J. R. Zeevaart, M. Konijnenberg, C. Müller, J. Kindblom
Dosimetric analysis of the short-ranged particle emitter ^{161}Tb for radionuclide therapy of metastatic prostate cancer
Cancers (2021), 1179512. DOI: 10.3390/cancers13092011

F. Borgna, S. Haller, J. M. Monné Rodriguez, M. Ginj, P. V. Grundler, J. Rijn Zeevaar, U. Köster; R. Schibli, N. P. van der Meulen, C. Mueller
Combination of terbium-161 with somatostatin receptor antagonists – A potential paradigm shift for the treatment of neuroendocrine neoplasms
European Journal of Nuclear Medicine and Molecular Imaging (2021). DOI: 10.1007/s00259-021-05564-0

F. Borgna, P. Barritt, P. V. Grundler, Z. Talip, S. Cohrs, J. Rijn Zeevaart, U. Köster, R. Schibli, N. P. van der Meulen, C. Müller
Simultaneous Visualization of ^{161}Tb- and ^{177}Lu-labeled Somatostatin Analogues Using Dual-Isotope SPECT Imaging
Pharmaceutics, 13, 536 (2021). DOI: 10.3390/pharmaceutics13040536

S. Bottoni , N. Cieplicka-Orynczak, S. Leoni, B. Fornal, G. Colò, P. F. Bortignon, G. Bocchi, D. Bazzacco, G. Benzoni, A. Blanc, A. Bracco, S. Ceruti, F. C. L. Crespi, G. de France, E. R. Gamba, Ł. W. Iskra, M. Jentschel, U. Köster, C. Michelagnoli, B. Million, D. Mengoni, P. Mutti, Y. Niu, C. Porzio, G. Simpson, T. Soldner, B. Szpak, A. Türler, C. A. Ur, W. Urban
Low-spin particle-core and hole-core excitations in ^{41,47,49}Ca isotopes studiedby cold-neutron-capture reactions
Physical Review C: Nuclear Physics, 103, 014320 (2021). https://doi.org/10.1103/PhysRevC.103.014320

N. M. Chiera, S. Bolisetty, R. Eichler, R. Mezzenga, P. Steinegger
Removal of radioactive cesium from contaminated water by whey protein amyloids–carbon hybrid filters
RSC ADVANCES, 11 (2021). DOI: 10.1039/D1RA05376K

N. M. Chiera, T. K. Sato, R. Eichler, T. Tomitsuka, M. Asai, S. Adachi, R. Dressler, Dr. Kentaro Hirose, H. Inoue, Y. Ito, A. Kashihara, H. Makii, K. Nishio, M. Sakama, K. Shirai, H. Suzuki, K. Tokoi, K. Tsukada, E. Watanabe, Y. Nagame
Chemical Characterization of a Volatile Dubnium Compound, $DbOCl_3$
Angewandte Chemie, 133, 18015 (2021). DOI: 10.1002/ange.202102808

M. Dietz, C. Lederer-Woods, A. Tattersall, U. Battino, F. Gunsing, S. Heinitz, M. Krticka, J. Lerendegui-Marco, R. Reifarth, S. Valenta, O. Aberle, S. Amaducci, P. Žugec on behalf of the n_TOF Collaboration
Measurement of the ^{72}Ge(n, γ) cross section over a wide neutron energyrange at the CERN n_TOF facility
Physical Review C, 103, 045809 (2021). https://doi.org/10.1103/PhysRevC.103.045809

C. Duchemin, J. P. Fernandes Pinto Ramos, T. Stora, E. Ahmed, E. Aubert, N. Audouin, E. Barbero, V. Barozier, A.-P. Bernardes, P. Bertreix, A. Boscher, F. Bruchertseifer, R. Catherall, E. Chevallay, P. Christodoulou, K. Chrysalidis, T. E. Cocolios, J. Comte, B. Crepieux, M. Deschamps, K. Dockx, A. Dorsival, V. N. Fedosseev, P. Fernier, R. Formento-Cavaier, S. El Idrissi, P. Ivanov, V. Gadelshin, S. Gilardoni, J.-L. Grenard, F. Haddad, R. Heinke, B. Juif, U. Khalid, M. M. Khan, U. Köster, L. Lambert, G. Lilli, G. Lunghi, B. A. Marsh, Y. Martinez-Palenzuela, R. Martins, S. Marzari, N. Menaa, N. Michel, M. Munos, F. Pozzi, F. Riccardi, J. Riegert, N. Riggaz, J.-Y. Rinchet, S. Rothe, B. Russell, C. Saury, T. Schneider, S. Stegemann, Z. Talip, C. Theis, J. Thiboud, N. P. van der Meulen, M. Van Stenis, H. Vincke, J. Vollaire, N.-T. Vuong, B. Webster, K. Wendt, S. Wilkins
CERN-MEDICIS: a review since commissioning in 2017
Frontiers in Medicine*,* 8, 693682 (2021)*.* DOI: 10.3389/fmed.2021.693682

M. T. Durán, F. Juget, Y. Nedjadi, F. Bochud, Z. Talip, N. P. van der Meulen, U. Köster, C. Duchemin, T. Stora, C. Bailat
Ytterbium-175 half-life determination
Applied Radiation and Isotopes, 109893 (2021). DOI: 10.1016/j.apradiso.2021.109893

C. Favaretto, Z. Talip, F. Borgna, P. V. Grundler, G. Dellepiane, A. Sommerhalder, H. Zhang, R. Schibli, S. Braccini, C. Müller, N. P. van der Meulen
Cyclotron production and radiochemical purification of terbium-155 for SPECT imaging
EJNMMI Radiopharmacy and Chemistry, 6, 37 (2021). DOI: 10.1186/s41181-021-00153-w

A. Gawlik, C. Lederer-Woodsb, J. Andrzejewskia, J. Perkowskia, U. Battinob, P. Ferreirac, F. Gunsingd, S. Heinitz, M. Krtičkag , C. Massimih, F. Mingroneh, R. Reifarthj, A. Tattersallb, S. Valentag, C. Weisse, O. Aberle, P. Žugec on behalf of the n_TOF Collaboration
Radiative neutron capture cross-section measurement of Ge isotopes at n_TOF CERN facility and its importance for stellar nucleosynthesis.
Acta Physica Polonica A, 139, 383 (2021). https://doi.org/10.12693/APhysPolA.139.383

A. Gawlik, C. Lederer-Woods, M. Krticka, S. Valenta, U. Battino, J. Andrzejewski, J. Perkowski, O. Aberle, P. Žugec on behalf of the n_TOF Collaboration
Measurement of the ^{76}Ge(n, γ) cross section at the n_TOF facility at CERN
Physical Review C, 104, 044610 (2021). https://doi.org/10.1103/PhysRevC.104.044610

R. Heinke, E. Chevallay, K. Chrysalidis, T. E. Cocolios, C. Duchemin, V. N. Fedosseev, L. Lambert, B. A. Marsh, N. P. van der Meulen, P. Sprung, T. Stora, M. Tosato, S. G. Wilkins, H. Zhang, Z. Talip
Efficient production of high-specific-activity thulium-167 at Paul Scherrer Institute and CERN-MEDICIS
Frontiers in Medicine, 8, 712374 (2021). DOI: 10.3389/fmed.2021.712374

F. Juget, Z. Talip, T. Buchillier, M. T. Durán, Y. Nedjadi, L. Desorgher, F. Bochud, P. Grundler, N. P. van der Meulen, C. Bailat
Determination of the gamma and X-ray emission probabilities of ^{161}Tb Effect of diluent
Applied Radiation and Isotopes, 109770 (2021). DOI: 10.1016/j.apradiso.2021.109770

I. Kajan, M. Florianov, C. Ekbergc, A. V. Matyskin
Effect of diluent on the extraction of europium(III) and americium(III) with N,N,N′ ,N′ -tetraoctyl diglycolamide (TODGA)
RSC Advances, 11, 36707 (2021). https://doi.org/10.1039/D1RA07534A

I. Kajan, S. Heinitz, K. Kossert, P. Sprung, R. Dressler, D. Schumann
First direct determination of the ^{93}Mo half-life
Scientific Reports, 11, 19788 (2021). https://doi.org/10.1038/s41598-021-99253-

I. Kajan, S. Pommé, K. Pelczar, S. Heinitz
Measurement of the ^{145}Sm half-life
Applied Radiation and Isotopes, 178, 109978 (2021). https://doi.org/10.1016/j.apradiso.2021.109978

I. Kajan, S. Pommé, K. Pelczar, S. Heinitz
Measurement of the ^{171}Tm half-life
Journal of Radioanalytical and Nuclear Chemistry. (2021) https://doi.org/10.1007/s10967-021-08108-w

E. Karlsson, J. Neuhausen, R. Eichler, I. I. Danilov, A. Vögele, A. Türler
Thermochromatographic behavior of iodine in 316L stainless steel columns when evaporated from lead-bismuth eutectic
Journal of Radioanalytical and Nuclear Chemistry, 328, 707 (2021). DOI: 10.1007/s10967-021-07682-3

E. Karlsson, J. Neuhausen, R. Eichler, I. I. Danilov, A. Vögele, A. Türler
Silver as a capturing material for iodine released from lead-bismuth eutectic in various conditions
Journal of Radioanalytical and Nuclear Chemistry, 328, 691 (2021). DOI: 10.1007/s10967-021-07669-0

E. Karlsson, J. Neuhausen, A. Aerts, I. I. Danilov, R. Eichler, A. Türler, A. Vögele
Polonium behavior following a vacuum window rupture in a lead-bismuth eutectic based accelerator driven system
Applied Radiation and Isotopes, 168, 109551 (2021). DOI: 10.1016/j.apradiso.2020.109551

B. Kraus, P. Steinegger, N. V. Aksenov, R. Dressler, R. Eichler, E. Griesmayer, D. Herrmann, A. Türler, C. Weiss
Charger carrier properties of single-crystal CVD diamond up to 473 K
Nuclear Instruments and Methods in Physics Research A, 989 (2021). DOI: 10.1016/j.nima.2020.164947

C. Lederer-Woods, P. J. Woods, T. Davinson, D. Kahl, S. J. Lonsdale, O. Aberle, S. Amaducci, P. Žugec on behalf of the n_TOF Collaboration
Destruction of the cosmic γ-ray emitter ^{26}Al in massive stars: study of the key ^{26}Al(n, p) reaction.
Physical Review C: Nuclear Physics, 104, L022803 (2021). https://doi.org/10.1103/PhysRevC.104.L022803

T. V.M. Lima, S. Gnesin, K. Strobel, M. del Sol Perez, J. E. Roos, C. Müller, N. P. van der Meulen
Fifty shades of scandium: comparative study of PET capabilities using Sc-43 and Sc-44 with respect to conventional clinical radionuclides
Diagnostics, 11, 1826 (2021). DOI: 10.3390/diagnostics11101826

C. Müller, R. Schibli, P. Bernhardt, U. Köster, N. P. van der Meulen
Terbium radionuclides for theranostics
Encyclopedia of Nuclear Medicine and Molecular Imaging, (Reference Module in Biomedical Sciences), 2021, Elsevier. DOI: 10.1016/B978-0-12-822960-6.00076-4

S. Pommé, K. Pelczar, K. Kossert, I. Kajan
On the interpretation of annual oscillations in ^{32}Si and ^{36}Cl decay rate measurements
Scientific Reports, 11, 16002 (2021). https://doi.org/10.1038/s41598-021-95600-8

G. F. Steyn, T. N. van der Walt, F. Szelecsenyi, C. Perrang, J. W. Brummer, C. Vermeulen, N. P. van der Meulen, M. A. Motetshwane, M. R. van Heerden.
Large-scale production of ^{88}Y and ^{88}Zr/^{88}Y generators: A proof of concept study for a 70 MeV H- cyclotron.
Applied Radiation and Isotopes, 168, 109469 (2021). DOI: 10.1016/j.apradiso.2020.109469S.

P. Steinegger
Open questions on chemistry in the synthesis and characterization of superheavy elements
Communications in Chemistry, 4 (2021). DOI: 10.1038/s42004-021-00529-8

Z. Talip, R. Dressler, B. Schacherl, J. C. David, C. Vockenhuber, D. Schumann
Radiochemical determination of long-lived radionuclides in proton-irradiated heavy metal targets: part II tungsten
Analytical Chemistry, 93(31), pp. 10798-10806 (2021). DOI: 10.1021/acs.analchem.1c00640

Z. Talip, F. Borgna, C. Müller, J. Ulrich, C. Duchemin, T. Stora, U. Köster, Y. Nedjadi, V. Gadelshin, V. Fedosseev, F. Juget, C. Bailat, A. Fankhauser, S. Wilkins, L. Lambert, B. Marsh, D. Fedorov, E. Chevallay, P. Fernier, R. Schibli, N. P. van der Meulen
Production of mass separated Er-169 towards the first preclinical in vitro investigations
Frontiers in Medicine 8, 643175 (2021). DOI: 10.3389/fmed.2021.643175

Z. Talip, F. Juget, J. Ulrich, Y. Nedjadi, T. Buchillier, T. Duran, F. Bochud, C. Bailat, N. P. van der Meulen
Determination of the gamma and X-ray emission probabilities of ^{169}Er
Applied Radiation and Isotopes (2021), 176, 109823. DOI: 10.1016/j.apradiso.2021.109823

M. Veicht, I. Kajan, J.C. David, S. Chen, E. Strub, I. Mihalcea, D. Schumann
Experiment-based determination of the excitation function for the production of Ti-44 in proton-irradiated vanadium samples
Physical Review C, 104(1) (2021). DOI: 10.1103/PhysRevC.104.014615

M. Veicht, I. Mihalcea, D. Cvjetinovic, D. Schumann
Radiochemical separation and purification of non-carrier-added silicon-32
Radiochimica Acta, 109(10) (2021). DOI: 10.1515/ract-2021-1070x

A. Wallner, M. B. Froehlich, M. A. C. Hotchkis, N. Kinoshita, M. Paul, M. Martschini, S. Pavetich, S. G. Tims , N. Kivel, D. Schumann, M. Honda, H. Matsuzaki , T. Yamagata
^{60}Fe and ^{244}Pu deposited on earth constrain the r-process yields of recent nearby supernovae.
Science, 372, 742 (2021). https://doi.org/10.1126/science.aax3972

Y. Wittwer, R. Eichler, D. Herrmann, A. Türler
The influence of chemical parameters on the in-situ metal carbonyl complex formation studied with the fast on-line reaction apparatus (FORA)
Radiochimica Acta, 109, 243 (2021). https://doi.org/10.1515/ract-2020-0031

Y. Wittwer, R. Eichler, R. Zingg, D. Herrmann, A. Türler
The influence of gas purification and addition of macro amounts of metal-carbonyl complexes on the formation of single-atom metal-carbonyl-complexes.
Radiochimica Acta, 109, 799 (2021). https://doi.org/10.1515/ract-2020-0036

N. P. van der Meulen, Z. Talip
Non-conventional radionuclides: the pursuit for perfection (changed by the editor to "non-conventional radionuclides: radiochemistry and radiolabeling")
Encyclopedia of Nuclear Medicine and Molecular Imaging (Reference Module in Biomedical Sciences), 2021, Elsevier.
DOI: 10.1016/B978-0-12-822960-6.00052-1

N. P. van der Meulen, K. Stroba, T. V.M. Lima
New Radionuclides and Technological Advances in SPECT and PET Scanners
Cancers, 13(24), 6183 (2021). DOI: 10.3390/cancers13246183

INTERNAL REPORTS

R. Eichler
HIMB External Review Committee, "TATTOOS @ HIPA PSI"
PSI (virtual), 26 October 2021

Z. Talip
CERN-MEDICIS 7th Board Meeting, "Thulium-167 production at MEDICIS from external PSI target"
CERN (virtual), 11 March 2021

Z. Talip
PRISMAP WP12 meeting, ''WP12 and partner PSI''
CERN (virtual), 30 September 2021

Z. Talip
PRISMAP Consortium Meeting, ''PRISMAP WP12 Status''
CERN (virtual), 13 October 2021

Z. Talip
CERN MEDICIS 8th Board Meeting, ''Yb-175 Project Progress''
CERN (virtual), 9 November 2021

Z. Talip
PRISMAP 2nd Consortium Meeting, "The link between WP4 and WP12"
CERN (virtual), 23 November 2021

Z. Talip
PRISMAP 2nd Consortium Meeting, ''WP12 Progress''
CERN (virtual), 24 November 2021

CONTRIBUTIONS TO CONFERENCES, WORKSHOPS AND SEMINARS

N. M. Chiera
Chemical Investigation with Exotic Radionuclides
SCS Fall Meeting 2021, Switzerland, 10 September 2021 (online)

N. M. Chiera
Chemistry with Exotic Radionuclides at LRC
NES BerK 2021, Villigen PSI, Switzerland, 30 November, 2021 (online)

R. Eichler
Preparation and Prospective of Chemistry Experiments with SHE @ SHE-Factory Dubna
The Virtual SHE seminars (SHE2021), Poland, 26 January 2021 (online)

P. Ionescu
Superheavy element chemistry and the residual gas effects on the chromatographic yield of homologs Hg and At
ACS Spring 2021, San Antonio (TX), United States, 05-16 April 2021 (online)

P. Ionescu
Superheavy element chemistry and the residual gas effects on the chromatographic yield of homologs Hg and At
NES PhD-Day 2021, Villigen PSI, Switzerland, 06 May 2021 (online)

L. Liu
Exploration of astatine chemistry in solution: Focus on the Pourbaix diagram in noncomplexing medium and characterization of astatine-mediated halogen bonds
LRC-Seminar, Paul Scherrer Institut, Villigen PSI, 19 November 2021

E. A. Maugeri
Opportunity from PSI
Italian section of the n_TOF collaboration, Annual meeting, 30 November 2021 (online)

E. A. Maugeri
Isotope production and Targetry at PSI
SANDA workshops for target production: Part I and II, 18 August 2021 (online)

I. Mihalcea
SINCHRON: From Idea to Implementation
LRC-Seminar, Paul Scherrer Institut, Villigen PSI, Switzerland, 12 March 2021

I. Mihalcea
Quenching volatility of SiF_6^{-2}
Bi-annual Meeting (SINCHRON Project), Paul Scherrer Institut, Villigen PSI, Switzerland, 20 May 2021

I. Mihalcea
Re-determination of the ^{32}Si half-life. Part 1: Overview
Bi-annual Meeting (SINCHRON Project), Paul Scherrer Institut, Villigen PSI, Switzerland, 22 November 2021

J. Neuhausen
WP12- Chemistry control experiments and modelling
PATRICIA 2nd Task12.2 Meeting, 05 March 2021 (online)

J. Neuhausen
WP12- Chemistry control experiments and modelling
PATRICIA 2nd TCB-Meeting, 12 March 2021 (online)

J. Neuhausen, A. Folgado de Lucena, A. Aerts
Task 3.1 – Fission product release from HLM and deposition from the gas phase
1st PASCAL progress meeting, 27 April 2021 (online)

J. Neuhausen, A. Folgado de Lucena, A. Aerts
Task 3.1 – Fission product release from HLM and deposition from the gas phase
1st PASCAL WP3 technical progress meeting, 31 May 2021 (online)

J. Neuhausen
Challenges and future of coolant chemistry of advanced nuclear reactors
LRC-Retreat, Hinterzarten, Germany, 21 October 2021

J. Neuhausen
WP12- Chemistry control experiments and modelling
PATRICIA 3rd TCB-Meeting, 27 October 2021 (online)

J. Neuhausen
WP12- Chemistry control experiments and modelling
PATRICIA Technical Review Meeting, 28 October 2021 (online)

J. Neuhausen, L. Liu, A. Folgado de Lucena
Task 3.1 – Fission product release from HLM and deposition from the gas phase
2nd PASCAL WP3 progress meeting, 19 November 2021 (online)

J. Neuhausen, L. Liu, A. Folgado de Lucena
Task 3.1 – Fission product release from HLM and deposition from the gas phase
2nd PASCAL progress meeting – session 2, 09 December 2021 (online)

D. Schumann
WP3: Target Preparation for Improvement of Nuclear Data Measurements
SANDA collaboration meeting, 11 February 2021 (online)

D. Schumann
Workshop chair, Introduction and closing remarks
SANDA workshop for Target Production, 18 August 2021 (online)

P. Steinegger
Status and plans of chemical research with heaviest elements at PSI and FLNR
TASCA Workshop 2021, Germany, 21-23 June 2021 (online)

P. Steinegger
Chemistry with Superheavy Elements at PSI
NES BerK, Villigen PSI, Switzerland, 27 October 2021

Z. Talip
Production of Radiolanthanides for Nuclear Medicine Applications
Conference on Applied Radiation Metrology Agenda 2021, 22 November 2021 (online)

G. Tiebel
Further Development of Vacuum Chromatography for Super Heavy Elements
LRC-Seminar, Villigen PSI, Switzerland, 19 November 2021

N. van der Meulen
Terbium-149 for targeted alpha therapy
66th INTC Meeting, CERN, 03 February 2021 (online)

N. van der Meulen
Reactor-produced Terbium-161: from production towards first-in-human clinical application
IAEA Technical Meeting on State of the Art Research Reactor Based Radioisotope and Radiopharmaceutical Production, 24 March 2021 (online)

N. van der Meulen
TATTOOS: a PSI strategy initiative
PSI TATTOOS Mini-symposium, Villigen PSI, Switzerland, 26 April 2021

N. van der Meulen
Pursuing the theragnostic principle at Paul Scherrer Institute
University of Geneva (UNIGE) Radiopharmaceutical lecture, 29 April 2021 (online)

N. van der Meulen
Pursuing the theragnostic principle at Paul Scherrer Institute
UAB/UWM Seminar, 05 May 2021 (online)

N. van der Meulen
A discussion on the supporting medical isotope ecosystem from isotopes to radiopharmaceuticals
Canadian Nuclear Isotope Council, European Virtual Trade Mission, Supply Chain & Support Services Opportunities, 03 November 2021 (online)

N. van der Meulen
Pursuing the radiotheragnostics concept at Paul Scherrer Institute
Pacifichem2020, 17 December 2021 (online)

M. Veicht
Re-determination of the ^{32}Si Half-Life
Annual Report No. 3 (Informal Meeting), Paul Scherrer Institut, Villigen PSI, Switzerland, 15 April 2021

M. Veicht
Determination of the number atoms, utilizing (MC)-ICP-MS
Meeting w/ P. Sprung (PSI) & S. Roellin (Labor Spiez), Paul Scherrer Institut, Villigen PSI, Switzerland, 04 May 2021 (online)

M. Veicht
Chronometric Potential: Development of a Chemical Separation Procedure for the Preparation of ^{32}Si in a Pure State
NES PhD-Day, Paul Scherrer Institut, Villigen PSI, Switzerland, 06 May 2021 (online)

M. Veicht
Implementing new isotopes for environmental research: Redetermination of the ^{32}Si half-life
Bi-annual Meeting (SINCHRON), Paul Scherrer Institut, Villigen PSI, Switzerland, 20 May 2021 (online)

M. Veicht
Re-determination of the ^{32}Si Half-Life
Annual Report No. 4 (informal meeting), Paul Scherrer Institut, Villigen PSI, Switzerland, 04 August 2021

M. Veicht
Nanoscale mechanism of UO_2 formation through uranium reduction by magnetite (Pan et al., 2020)
LRC-Seminar, Paul Scherrer Institut, Villigen PSI, Switzerland, 24 September 2021

M. Veicht
Re-determination of the ^{32}Si Half-Life
Annual Report No. 2 (Formal Meeting), Paul Scherrer Institut, Villigen PSI, Switzerland, 13 October 2021

M. Veicht
Implementing new isotopes for environmental research: Redetermination of the ^{32}Si half-life
Bi-annual Meeting (SINCHRON), Paul Scherrer Institut, Villigen PSI, Switzerland, 22 November 2021 (online)

M. Veicht
Radiochemical separation of Si-32 from proton-irradiated vanadium: Towards an accurate half-life determination
TrisKem's Virtual Users Group Meeting (part of NPL's Virtual Conference on Applied Radiation Metrology, vCARM), National Physical Laboratory (NPL), Teddington, United Kingdom, 24 November 2021 (online)

J. Wilson
Homolog Studies in Preparation for Nihonium Chemistry
LRC-Seminar, Villigen PSI, Switzerland, 24 September 2021

I. Zivadinovic
Sample preparation LBE-Te+ refractory metals
PATRICIA 2nd Task12.2 Meeting, 05 March 2021 (online)

I. Zivadinovic
Evaporation of radionuclides from heavy-liquid-metal-cooled reactors
NES PhD-Day, Paul Scherrer Institut, Villigen PSI, 6 May 2021

I. Zivadinovic
Evaporation of radionuclides from heavy-liquid-metal-cooled reactors
LRC-Seminar, Paul Scherrer Institut, Villigen PSI, 18 June 2021

I. Zivadinovic
Sample preparation studies and Radionuclide release experiments
PATRICIA Technical Review Meeting, 28 October 2021 (online)

POSTER PRESENTATIONS

N. M. Chiera
On the re-determination of the half-life of ^{146}Sm, ^{148}Gd, and ^{154}Dy
NIC-XVI - 16th International Symposium on Nuclei in the Cosmos, China, 21 September 2021 (online)

C. Favaretto, Z. Talip, P.V. Grundler, S. Geistlich, S. Landolt, D.E. Schmid, J. R. Zeevaart, U. Köster, C. Müller, R. Schibli, N. P. van der Meulen
The production of ^{161}Tb and its introduction to the clinic through the Good Manufacturing Practice-compliant radiolabeling of [^{161}Tb]Tb-DOTATOC
eSRS, 17 May 2021 (online)

C. Favaretto, Z. Talip, F. Borgna, P.V. Grundler, H. Zhang, C. Müller, R. Schibli, N. P. van der Meulen
Cyclotron production and radiochemical purification of the radiolanthanide terbium-155 for potential application in nuclear medicine
Swiss Chemical Society (SCS) Fall Meeting, Bern, Switzerland, 10 September 2021 (online)

P. Ionescu
The Chemistry of Superheavy Element Copernicium (Z = 112)
Swiss Chemical Society (SCS) Fall Meeting, Bern, Switzerland, 10 September 2021 (online)

G. Tiebel
High temperature α-spectroscopy with 4H-SiC-based detectors for superheavy elements
GDCh-Wissenschaftsforum Chemie 2021, Germany, 29 August - 01 September 2021 (online)

G. Tiebel
Characterization of the SINQ gas-jet facility as a source for fission products from ^{235}U
Swiss Chemical Society (SCS) Fall Meeting, Bern, Switzerland, 10 September 2021 (online)

J. Wilson
Gas chromatogrpahic investigation of short-lived thallium isotopes produced in the ^{141}Pr(^{48}Ti,xn) reaction
GDCh-Wissenschaftsforum Chemie 2021, Germany, 29 August – 01 September 2021 (online)

J. Wilson
Isothermal Gas Adsorption Chromatography of Different Thallium Species for Future Investigations of Nihonium
Swiss Chemical Society (SCS) Fall Meeting, Bern, Switzerland, 10 September 2021 (online)

M. Veicht
Radiochemical separation and purification of non-carrier-added silicon-32 for an accurate half-life redetermination
Swiss Chemical Society (SCS) Fall Meeting, Bern, Switzerland, 10 September 2021 (online)

I. Zivadinovic
Evaporation of radionuclides from heavy-liquid-metal-cooled reactors
Swiss Chemical Society (SCS) Fall Meeting, Bern, Switzerland, 10 September 2021 (online)

MEMBERS OF SCIENTIFIC COMMITTEES AND EXTERNAL ACTIVITIES

Dr. Robert Eichler

- Associate Editor of the International Journal of Modern Physics E (IJMPE) World Scientific Publishing
- Labor für Ionenstrahlphysik ETH Zürich, Member of Curatorial Board (on behalf of PSI)
- Radiochimica Acta, Member od Scientific Advisory Board

Prof. Dr. Patrick Steinegger

- Nuklearforum Schweiz, member

Dr. Nicholas van der Meulen

- United States Department of Energy (DOE Isotope R&D FOA), Panel Reviewer
- Accelerator for Research in Radiochemistry and Oncology at Nantes Atlanti (ARRONAX), International Scientific Committee, member
- PSI internal research commission (FoKo), member
- International Advisory Committee for the Workshop on Targetry and Target Chemistry
- Academic Editor for Public Library Of Science (PLOS)
- Reviewer Board member: Instruments (MDPI)
- Editorial Board member: EJNMMI Radiopharmacy and Chemistry

PUBLIC RELATION AND OUTREACH ACTIVITIES

N. M. Chiera
Interview for "Introducing..." Angewandte Chemie International Edition
DOI: 10.1002/anie.202107318
09 July 2021

R. Eichler
Interview In: "Elements of Surprize: Hassium" by Alan Neal, CBC Radio in Canada
(CBC is the Canadian Broadcasting Corporation, Canada's National Public Radio)
04 May 2021

A. Pautz, N. M. Chiera
Chemical characterization of a volatile dubnium compound, $DbOCl_3$
DIRK – NES Scientific Highlights. PSI, 10 August 2021

P. Steinegger, S. Bolisetty, N.M. Chiera, E. Pishchalnikova, G. Tiebel, R. Eichler
«Nano-Wissen- Atomfilter für sauberes Wasser»
https://www.3sat.de/wissen/nano/210617-sendung-102.html
3Sat TV, 17 June 2021

P. Steinegger
Von neuen Elementen bis zum Alter des Universums
Scientifica 21 (Zürcher Wissenschaftstage), ETH Hönggerberg, Zürich, Switzerland, 05 September 2021

P. Steinegger
Radiochemie: Von neuen Elementen des Periodensystems bis zum Alter des Universums
Studieninformationstage 2021, ETHZ, D-CHAB (online event), Switzerland, 08 September 2021

P. Steinegger
Radiochemistry at PSI and the Chemistry of Transactinide Elements
Unidays of the youngSCS (online event), Switzerland, 18 November 2021

P. Steinegger
Auf der Suche nach neuen Elementen des Periodensystems … und was es sonst noch zu sehen gibt
ETH Unterwegs: Gymnasium Neufeld, Bern, Switzerland, 18 November 2021

N. van der Meulen, C. Müller
Terbium Triumph
https://www.psi.ch/en/bio/scientific-highlights/terbium-triumph
21 December 2021

M. Veicht
Sonntagsdienst psiFORUM – PSI's outreach to the public

M. Veicht
PhD Coach/Mentor for 1st Year PhD Students at EDCH (EPFL)

LECTURES AND COURSES

R. Eichler
Nuclear Engineering Master course Nuclear Energy Systems: The Origin and Chemistry of Uranium
ETH Zürich, Spring Semester 2021

R. Eichler
Master course Physikalische Chemie Radiochemie The Chemistry and Physics of Heaviest Elements
University of Bern, Autumn Semester 2021

P. Steinegger
529-0121-00L Anorganische Chemie I
ETH Zürich, Fall Semester 2021

M. Veicht
Basic Principles of Drug Action at the Nervous System
University de Lausanne (UNIL), CH-603, Spring Semester 2020/2021

M. Veicht
Practical lab course: "Introduction to Chemical Engineering" | TP-4: Photovoltaïque
École Polytechnique Fédérale de Lausanne (EPFL), ChE-203, Spring Semester 2020/2021

M. Veicht
Exam Supervision: "General and Analytical Chemistry I (BIO+PHARM)"
University de Lausanne (UNIL), UNIL-101, Autumn Semester 2020/2021

M. Veicht
Exam Supervision: "General and Analytical Chemistry II (BIO+PHARM)"
University de Lausanne (UNIL), UNIL-102, Autumn Semester 2020/2021

M. Veicht
Practical lab course: "Chemistry Analytic Laboratory I" | Titrage et pH, and Conductimétrie
University de Lausanne (UNIL), UNIL-103, Autumn Semester 2021/2022

M. Veicht
Atomic Spectroscopy Virtual Symposium
Agilent Technologies, Inc., (online), March 03-04, 2021

I. Zivadinovic
529-0011-04L Praktikum Allgemeine Chemie
ETH Zürich, 24.09-21.12.2021

SEMESTER WORK

Simon Schätti
Semester Project for the Department of Mechanical Engineering, ETH Zürich
Target Preparation via Electrodeposition of Europium
Dr. N. M. Chiera (PSI) Laboratory supervisor
April-August 2021

Guilhem Louis de Galambert
Characterisation of holmium cathodes produced by molecular plating for the HOLMES experiment
Prof. Dr. A. Pautz (EPFL/PSI)
Dr. E. Maugeri (PSI)
July 2021

Oliver Pfister
Matura Arbeit Gymnasium Friedberg
Dr. N. M. Chiera (PSI)
August 2021

Cerboni Noemi Chiarina
Preparation and Characterisation of 163Ho Targets via Drop-On-Demand Inkjet Printing for Measuring the Electron Neutrino Mass
Dr. E. Maugeri (PSI)
May 2021

DOCTORAL THESES

Paul Ionescu
The Chemistry of Copernicium: Superheavy Element and Homolog Studies
Dr. R. Eichler (PSI)
Prof. Dr. A. Türler (Uni Bern)
December 2021

MASTER THESES

Guilhem Louis de Galambert
Characterisation of holmium cathodes produced by molecular plating for the HOLMES experiment
Prof. Dr. A. Pautz (EPFL/PSI)
Dr. E. Maugeri (PSI)
July 2021

AWARDS

Mario Veicht
3rd Place at the European Rover Challenge & Best Science Task
EPFL Xplore – Developing A Mars Rover From Scratch (Participation in the Science Team)
7th Edition of the European Rover Challenge (ERC), Kielce University of Technology, Poland
on-site: 10-12 September 2021

PAUL SCHERRER INSTITUT

LABORATORY OF RADIOCHEMISTRY OF THE PAUL SCHERRER INSTITUTE
31.12.2021

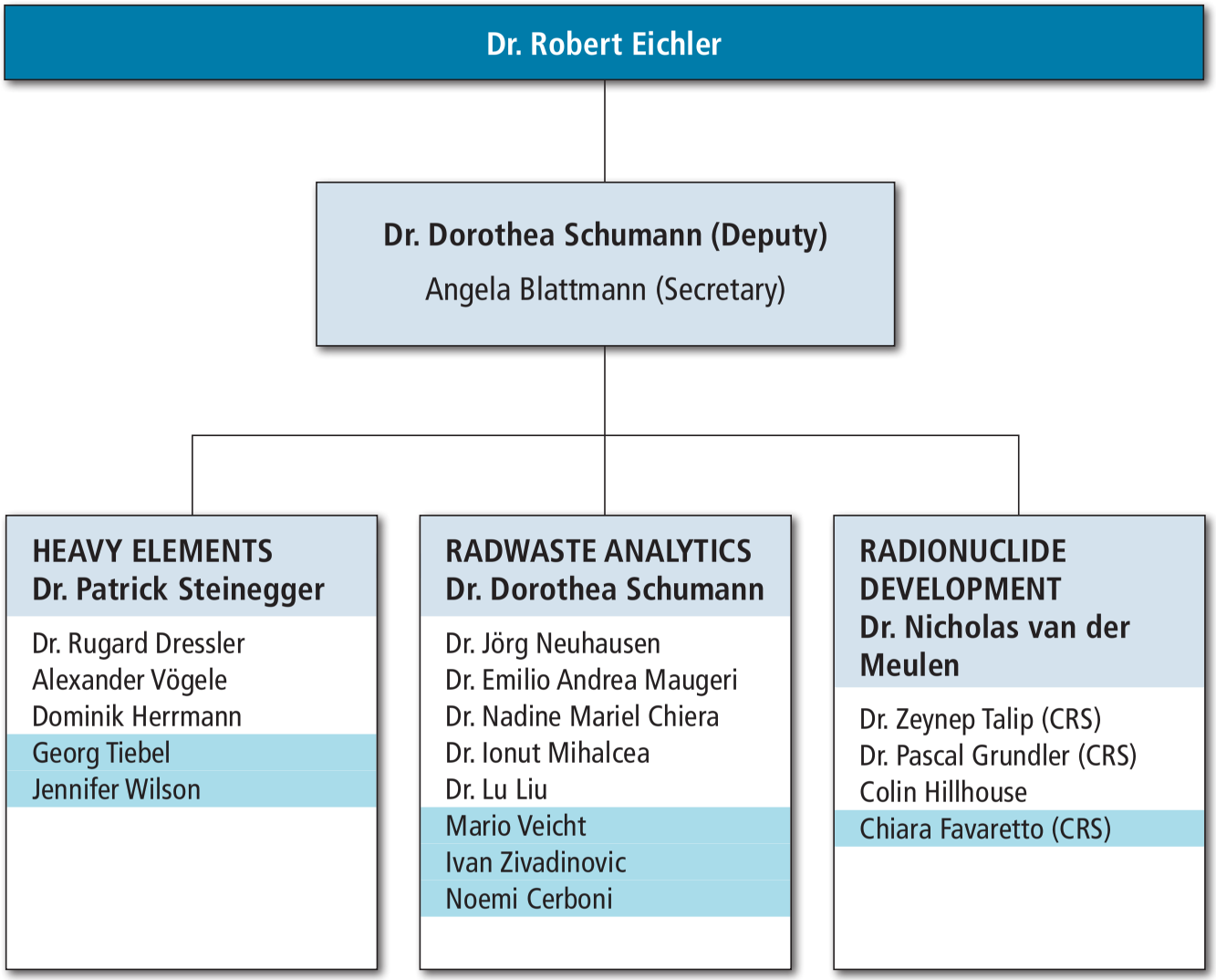

Graduate student

AUTHOR INDEX

AFFILIATION INDEX

AHL	Hot Laboratory, Division of the Nuclear Energy and Safety Department (NES), Paul Scherrer Institut, 5232 Villigen PSI, Switzerland
AEC	Albert Einstein Center for Fundamental Physics, Sidlerstrasse 5, 3012 Bern, Switzerland
ASI	Qualitätsmanagement, Paul Scherrer Institut, 5232 Villigen PSI, Switzerland
BluAct Technologies	BluAct Technologies GmbH, Defaux-Strasse 57, Glattpark, 8152 Zürich-Opfikon, Switzerland
CERN	CERN, Esplanade des Particules 1, P.O. Box, 1211 Geneva 23, Switzerland
CHUV	Centre Hospitalier Universitaire Vaudois, Rue du Grand Pré 1, 1007 Lausanne, Switzerland
CIVIDEC	CIVIDEC Instrumentation GmbH, Schottengasse 3A/1/41, 1010 Vienna, Austria
CRS	Center for Radiopharmaceutical Sciences, Paul Scherrer Institut, 5232 Villigen PSI, Switzerland
EPFL	École polytechnique fédérale de Lausanne, Route Cantonale, 1015 Lausanne, Switzerland
ETHZ	Eidgen. Technische Hochschule Zürich, 8092 Zürich, Switzerland
FLNR	Flerov Laboratory of Nuclear Reactions as part of the Joint Institute for Nuclear Research (JINR), Joliot-Curie 6, Dubna, 141980, Moscow region, Russian Federation
FRIB/MSU	Facility for Rare Isotope Beam, Michigan State Universit, 640 South Shaw Lan, East Lansing, USA
GFA	Grossforschungsanlagen, Paul Scherrer Institut, 5232 Villigen PSI, Switzerland
Ghent Univ.	Ghent University, 9000 Ghent, Belgium
ILL	Institut Laue-Langevin - 71 avenue des Martyr, CS 20156, 38042 GRENOBLE Cedex 9 - France
IRA	Institute de radiophysique, Rue du Grand-Pré 1, 1007 Lausanne, Switzerland
IRFU	Institute of research into the fundamental laws of the Universe, CEA-Saclay, DEIN CEA, Saclay 91191 Gif sur Yvette, cedex France
ISOLDE-CERN	ISOLDE, Esplanade des Particules 1, 1211 Geneva, Switzerland
JINR	Joint Institute for Nuclear Research, Joliot-Curie, 6, Dubna, 141980, Moscow region, Russian Federation
KU Leuven	KU Leuven, Institute for Nuclear and Radiation Physics, Celestijnenlaan 200d - bus 2418, B-3001 Heverlee, Belgium
LANL	Los Alamos National Laboratory, Los Alamos, NM 87545, United States of America
LBK	Bioenergy and Catalysis Laboratory, Paul Scherrer Institut, 5232 Villigen PSI, Switzerland
LHEP	Laboratory for High energy Physics, University of Bern, Sidlerstrasse 5, 3012 Bern, Switzerland
LMN	Laboratory for Micro and Nanotechnology, Division of the Nuclear Energy and Safety Department (NES) Paul Scherrer Institut, 5232 Villigen PSI, Switzerland
LNB	Laboratory of Nanoscale Biology, Paul Scherrer Institut, 5232 Villigen PSI, Switzerland
MSU	Lomonosov Moscow State University, GSP-1, Leninskie Gory, Moscow, 119991, Russian Federation
NPL	National Physical Laboratory, Hampton Rd, Teddington TW11 0LW, United Kingdom
PoliMi	Politecnico Milano 1863, Piazza Leonardo da Vinci 32, 20133 Milano, Italy
PSD	Detektor Wissenschaft+Charakterisierung, Paul Scherrer Institut, 5232 Villigen PSI, Switzerland
PSI	Paul Scherrer Institut, Forschungsstrasse 111, 5232 Villigen PSI, Switzerland

TU Wien	Technische Universität Wien, Karlsplatz 13, 1040 Vienna, Austria
SenSiC	SenSiC GmbH, Park Innovaare, deliveryLAB, 5234 Villigen, Switzerland
SFU	Simon Fraser University, 8888 University Dr, Burnaby, BC V5A 1S6, Canada
UDS	Université de Strasbourg, 4 rue Blaise Pascal, CS 90032, 67081 Strasborug cedex, France
Univ. Bern	Departement für Chemie und Biochemie, Universität Bern, Freiestr. 3, 3012 Bern, Switzerland
Univ. Paris-Saclay	Université Paris-Saclay, 3 rue Joliot Curie, Bâtiment Breguet, 91190 Gif-sur-Yvette, France
Univ. York	University of York, York, YO10 5DD, United Kingdom
UoM	University of Manchester, Oxford Rd, Manchester, M13 9PL, United Kingdom
UoS	University of Seville, 4 San Fernando Str. Sevilla 41004, Spain
ZRW	Zentrum für radiopharmazeutische Wissenschaft ZRW, Paul Scherrer Institut, 5232 Villigen PSI, Switzerland